Lehrstuhl für Biomedizinische Bildgebung

Hybrid selective plane illumination microscopy and optoacoustic mesoscopy

Benno Koberstein-Schwarz

Vollständiger Abdruck der von der Fakultät für Elektrotechnik und Informationstechnik der Technischen Universität München zur Erlangung des akademischen Grades eines Doktors der Naturwissenschaften genehmigten Dissertation.

Abstract

Imaging of intact, living specimen, especially model organisms has become an important and powerful tool to study genetic function, morphogenesis and several diseases including heart diseases and diabetes. In recent years, lightsheet fluorescence microscopy in particular has enabled in-vivo imaging of zebrafish larvae and other small model organisms. However, classical light microscopy always suffers from limited penetration depth, which becomes most apparent when being applied to 3D samples exeeding several $100\,\mu$m in dimension. This limit is caused by the scattering of light within the sample. In this thesis we introduce a hybrid selective plane illumination microscope (SPIM) and optoacoustic mesoscopy setup, enabling imaging beyond the limitations of pure light microscopy and extending the imaging depth. This new technology facilitates imaging of model organisms, such as the zebrafish from early larval stage, up to adulthood when the fish is several millimeter in width.

In order to improve imaging depth, two different strategies have been implemented; firstly the reconstruction of the SPIM images is improved with a novel prior and regularization approach for spatially variant blind deconvolution algorithms. The prior utilizes image information from neighboring planes to improve the estimation of the point spread function (PSF). Furthermore, the regularizer incorporates a simple scattering model into the reconstruction. As a result, the reconstruction is able to correct partially for the influence of scattering and to extend the imaging depth and resolution.

Secondly, to improve the optoacoustic reconstruction, advanced correction methods are implemented to account for imperfect transducer properties. The sensitivity field of the transducer is both simulated and measured, and then - using a weighting factor - incorporated into the backprojection reconstruction workflow.

The effects of the improved SPIM and the optoacoustic reconstructions are demonstrated on biological data sets of zebrafish at different stages of development. With the introduced setup and the work on the improved reconstruction, we are able to provide complementary hybrid contrast and track the development of a model organism over several weeks until it reaches adulthood.

Contents

List of abbreviations

1D	one-dimensional
2D	two-dimensional
3D	three-dimensional
a. u.	Arbitrary units
AR-OAM	acoustic-resolution optoacoustic microscopy
BPP	beam parameter product
CAD	Computer-aided design
CT	Computed tomography
CW	Continues wave
DAQ	Data acquisition (system)
EIR	Electrical impulse response
FOV	Field of view
FWHM	Full width at half maximum
GFP	Green fluorescent protein
GPU	Graphics processing unit
ISRA	Image space reconstruction algorithm
LED	Light-emitting diode
MIP	Maximum intensity projection
MPM	Multiphoton microscopy
MSE	Mean square error
MSOT	Multi-Spectral Optoacoustic Tomography
NA	Numerical aperture
NIR	Near infrared

Norm.	Normalized
OA	Optoacoustic
OPO	Optical parametric oscillator
OR-OAM	optical resolution optoacoustic microscopy
PSD	Power spectral density
PSF	Point spread function
PZT	Lead zirconate titanate
ROI	Region of interest
SHG	Second-harmonic generation
SIR	Spatial impulse response
SNR	Signal-to-noise ratio
SPIM	Selective plane illumination microscopy
STFT	Short time Fourier transform
THG	Third-harmonic generation
TPEM	Two-photon excitation microscopy

1 Introduction

Our modern understanding of how life works on a microscopic scale would not be the same without optical microscopy. In the last centuries, optical microscopy has become an indispensable tool in biology and medicine. From the first observation of bacteria by A. van Leeuwenhoek in 1676 [1] to the year 2014, when the Noble prize for Chemistry was awarded to Stephan Hell, Eric Betzig and William E. Moerner for super-resolution microscopy, optical microscopy evolved remarkably. Paradigms such as the belief that imaging resolution is necessarily limited by the diffraction limit has been proven wrong. Nevertheless, several limitations remain, whereof the imaging depth in biological samples is one of the most prominent [2]. Since its early beginnings, visualization of biological structures and processes has been restricted to superficial imaging or required histological slices. The reason for the limited imaging depth is scattering of light (especially within the visible spectrum) within the sample, which causes image blur and a strong decease in contrast. With a few minor exceptions, such as the transparent *C. elegans* or the embryonic zebrafish, these limitations make in-vivo imaging of whole samples challenging. Only in the last few decades several new techniques have emerged that extend the imaging depth. In confocal microscopy an improved optical resolution and contrast are achieved by suppression of out-of-focus light [3]. Instead of illuminating the entire sample, only one point is illuminated and a pinhole at the confocal plane of the objective is used to reject light from outside of the focal plane. Based on this principle several other techniques have been developed. New optical methods like multiphoton microscopy (MPM) can improve the optical sectioning even further and extend the imaging depth [4]. Chemical clearing is capable of turning even large opaque samples optically transparent [5]. However, the imaging depth of MPM is still affected by the scattering of light, which will restrict the imaging depth to around 1 mm. Optical clearing allows imaging of larger samples, but is a toxic process, hence cannot provide in-vivo images, which are necessary to observe biological processes such as neuronal activity, metabolism, or drug effects.

As a consequence, biological imaging of living samples has focused on small specimen and suffers from scattering as the organism grows. *Danio rerio* (zebrafish) are a good example for such a growing organism. It is transparent in the early (embryonic) stage and Casper mutant lines are available with no pigmentation. Furthermore, *Danio rerio* shares several genes and characteristics with other mammals including ourselves, which makes the zebrafish an interesting model organism [6]. As a result, the zebrafish has extensively been used to study genetic function, morphogenesis and developmental behavior. Its genome is fully sequenced and several different zebrafish lines are commercially available.
Studying genetic function and morphogenesis in such a model organism is crucial

to understand not only the underlying basic biology, but also investigate several diseases including heart diseases [7] and diabetes, which can also be found in humans. While transparent in the early stage of development, the zebrafish becomes increasingly more opaque with age. Genetic lines without pigmentation/melanin can extend the period the zebrafish can be imaged with optical methods, but scattering ultimately limits the ability to visualize processes and structures inside the organism. Therefore, most studies are confined to the embryonic stage of development. However, morphogenesis, gene expression, and behavior are not finalized at this early age and will develop until the fish reaches adulthood. The limited time frame of early embryonic development is also too short to study slowly developing diseases such as cancer in more detail [8].

These disease models would benefit from the possibility to image also larger and older specimen. Furthermore, the study of older zebrafish could possibly lead to new insights on genetic function and developmental process and behavior, such as aging and reproduction.

Acoustic resolution optoacoustic imaging (or optoacoustic mesoscopy) has proven to provide a much better penetration depth up to several millimeters [2]. In such a depth the excitation light is still present in the sample but fully diffusive. Therefore, an optical resolution of structures is no longer possible. Although optically excited, optoacoustic mesoscopy works independent of light scattering, and relies on the localization of the generated ultrasound. However, since the technique relies on acoustic focusing and acoustic resolution it does not reach the resolution of methods which rely on optical focusing, such as optical resolution optoacoustic microscopy or fluorescence microscopy. Therefore, small samples of only one or two hundred micrometers are not suitable for most optoacoustic mesoscopy systems. In the early larval stage of development cellular resolution is required to track the development of the organism and image biological processes.

The motivation behind this work is to establish a system for in-vivo imaging, which overcomes the limitations of light scattering and allows imaging over a larger scale from cellular resolution of small samples up to large specimen several millimeters in size.
To this end, this thesis investigates a hybrid system of selective plane illumination microscopy (SPIM) and optoacoustic mesoscopy system. SPIM is well suited for the three-dimensional (3D) in-vivo imaging and offers specific contrast, rapid acquisition, and a sub-micron resolution [9]. The potential of this technique for imaging small developing model organisms has been demonstrated earlier by many groups, e.g. [7, 10, 11]. However, the imaging depth of SPIM is limited by the scattering of light to around $100\,\mu\text{m}$. Optoacoustic mesoscopy on the other side can provide a larger imaging depth and label free contrast at a reduced resolution. Because of the reduced resolution, imaging of structures in samples smaller than a few hundred micrometers is difficult. The hybrid system aims to combine the advantages of both imaging modalities resulting in a system which supports a large range of sample sizes at high resolution and with complementary contrast.

The development, improvement, and implementation of suitable reconstruction algorithms for both of the imaging modalities form a vital aspect in this respect. To provide a truly hybrid modality with complementary contrast, the largest possible overlap in imaging depth between SPIM and optoacoutic mesoscopy is pursued. In this thesis a simple model for the scattering of light is incorporated into the reconstruction of the SPIM images, effectively increasing the imaging depth.

In contrast to SPIM, optoacoustic mesoscopy inherently offers a much better penetration depth. However, the reconstruction result is influenced by the transducer characteristics on the measured signal. By incorporating the transducer properties into the reconstruction, image quality was significantly improved.

In the first chapter of this thesis, the technical implementation of the hybrid system will be discussed. The introduction of the experimental setup is followed by a more detailed view on both imaging modalities and how new ideas have been used to improve the reconstruction. Finally, hybrid imaging results of a developing zebrafish, from larval stage until adulthood are presented, highlighting the possibilities of the presented hybrid system as a unique and novel tool for imaging in developmental biology.

2 Experimental Setup

2.1 Motivation and requirements for the setup

The system is designed to provide an imaging modality able to track the development of small model organisms over large temporal and spatial scales. Current techniques are either suited for high resolution imaging of small or young organisms (this includes techniques like SPIM), or offer mesoscopic imaging of larger organisms with a high imaging depth but at much lower resolution (mainly techniques related to optoacoustic mesoscopy). The aim is to track the development of a model organism over several weeks until it reaches adulthood. To achieve this goal, the system has to offer both a high spatial resolution to image larvae or embryos of only a few hundred micrometer in size and a large imaging depth to image older model organisms with a diameter of several millimeter. The imaging volume and field of view (FOV) has to match the expected sample sizes. Adult zebrafish can reach a diameter of around $1\,\mathrm{cm}$ which will be the desired maximum imaging size. Furthermore the imaging system should be well suited for in-vivo imaging to allow studies of the same specimen at different points in time during its development.
A variety of different optical and optoacoustic systems have been used for biological imaging of deep tissue and (developing) model organisms. In the following, a quick overview of the existing techniques in light microscopy and in optoacoustic imaging will be given. The advantages and disadvantages of each technique will be discussed to clarify the choice of the proposed hybrid SPIM and optoacoustic tomography system.

2.1.1 Review of light microscopy techniques

Over the last decades a large number of optical techniques have been developed and adopted for biological imaging [12]. These new techniques have taken resolution, imaging depth, and speed to a new level and enabled fast volumetric in-vivo imaging. Different techniques offer different advantages in terms of speed, penetration depth and resolution.

Multiphoton Microscopy

A variety of different microscopy methods use nonlinear excitation effects of two or more photons to gain image contrast [4,13]. Most of them are based on the confocal (laser scanning) microscope geometry. One of the most widely used method is two-photon excitation microscopy (TPEM) where the fluorophores in the sample are excited through the simultaneous absorption of two photons [14–16]. The probability of this simultaneous absorption is extremely low and therefore a high

intensity is needed in order to excite the fluorophores. The high intensity which is required for this non-linear effect is usually only found at the focal point which provides optical sectioning and prevents background signal generation. By raster scanning the focal spot through the volume of the sample a three-dimensional (3D) image is generated. An additional advantage besides the improved optical sectioning is the higher penetration depth due to lower scattering of light at larger wavelengths in the near infrared (NIR). Imaging depths from a few hundred micrometer up to 1.6 mm [15] have been reported for TPEM.

Besides the fluorescence contrast in TPEM, there are other nonlinear effects which can be used for imaging, such as second and third harmonic generation (SHG/THG). These effects offer label-free tissue contrast and are based on the presence of specific structures in the sample, such as myofibrils (for SHG) or micelles (for THG). Since studies often rely on the labeling of specific cells or proteins the scope of application of SHG and THG imaging and TPEM is different in many cases.

Two-photon excitation microscopy offers a superior imaging depth with high resolution through the whole image stack. However, the raster scan geometry is slow when larger volumes are imaged. Furthermore, multiphoton microscopy usually requires a high NA objective to achieve the high intensities at the focus, which is the reason the technique normally offers only a limited field of view. This makes TPEM well suited for high cellular resolution imaging of small organ or brain sections. There are approaches to combine multiphoton imaging with optoacustic microscopy [17]. Although providing hybrid contrast, the optoacustic system inherits the raster scan geometry from the multiphoton geometry making it not suitable for imaging of larger specimen. Furthermore, the optoacustic microscopy in the hybrid system relies on the focusing of light as well and therefore does enhance the imaging depth of the system.

Optical projection tomography

Another optical approach to obtain volumetric images is by collecting data from different projections (angles) of the volume. Both fluorescence and absorption contrast can be used for imaging. In the latter case, a light source is placed behind the sample and a transmission image is acquired. Mathematical models are utilized to reconstruct optical contrast from the different absorption images, similar to X-ray computed tomography (CT). Since the reconstruction in OPT is based on the same backprojection algorithm as in X-ray CT, the reconstruction is highly vulnerable to scattering. Therefore, OPT was first applied on cleared ex-vivo samples and later on microscopic samples in-vivo [12, 18].

To improve the imaging depth, the light propagation within the sample has to be modeled, which also utilizes also scattered photons for imaging. This more advanced technique is called Mesoscopic Fluorescence Tomography (MFT) and can significantly increase the imaging depth compared to OPT [19].
The tomographic geometry of OPT and MFT is well suited to be combined with

mesoscopic optoacoustic imaging (see next section 2.1.2).

While MFT offers a good imaging depth, it lacks the high resolution of other optical imaging methods. Both OPT and MFT typically require a large part of the sample to be in focus [12] and therefore low numerical aperture (NA) objectives with a lower resolution are used. In contrast to TPEM, MFT uses scattered photons for imaging, while in TPEM scattered photons are rejected.

Selective plane illumination microscopy

One technique which was first introduced under the name of ultramicroscopy [20] and which has become popular in the last decade, is selective plane illumination microscopy (SPIM) [9]. Here only a short overview of the advantages and applications of SPIM will be discussed. A more detailed introduction into SPIM imaging and different SPIM setups can be found in the next chapter.

In SPIM the sample is illuminated with a thin sheet of light and the fluorescence is collected by an objective and a camera perpendicular to the illumination. The lightsheet coincides with the focal plane of an objective and the sample is scanned through the lightsheet. In this manner a 3D image stack of the whole sample is acquired in a short period of time and therefore offers a high acquisition rate of entire volumes. The low photo damage and bleaching of the sample makes SPIM an ideal tool for in-vivo imaging of fast processes and developing organisms [9, 21]. The optical sectioning in SPIM largely reduces out of focus light. However, SPIM does not reach the same imaging depth as TPEM or MFT. The geometry of most SPIM setups, with a freely movable and rotatable sample is furthermore compatible with optoacoustic tomography geometries (see next section).

2.1.2 Review of optoacoustic imaging geometries

As mentioned in the introduction, there are two major approaches for optoacoustic imaging. In optical resolution optoacoustic microscopy (OR-OAM) a focused light beam is scanned across the sample, analogous to a confocal raster scan microscope. Although providing a complementary contrast, the method does not fundamentally change the penetration characteristics over optical methods. Similar to optical methods, OR-OAM is limited to depths where focusing of light is still effective. Depending on the degree of scattering this can vary from below $100\,\mu$m up to a few hundred micrometer.

In contrast, acoustic-resolution optoacoustic microscopy (AR-OAM) relies on the acoustic resolution of the ultrasound detector. This mode employs an unfocused or broader illumination. Imaging performance is based on the ability to localize acoustic sources which depends on the characteristics of the ultrasound detectors. While generally having a worse resolution than optical imaging or optical resolution optoacustic microscopy, acoustic resolution optoacoustic microscopy offers significantly better imaging depth up to several millimeters. AR-OAM is capable of filling

the gap between microscopic imaging with a high resolution below a micrometer and macroscopic scale imaging. In this case, AR-OAM is often referred as optoacoustic mesoscopy.

The technique is therefore well suited to image small model organisms such as zebrafish [22, 23]. Optoacoustic mesocopy can be realized in different scanning geometries, all with their own advantages and disadvantages. In the following a short review of the three most fundamental scanning geometries will be given.

Planar detection geometry systems

Systems with a planar detection geometry are usually raster scan systems, where the detector is scanned in a plane outside of the sample. There are different approaches in which a planar geometry can be implemented.

The most common systems are based on piezo transducers. The planar detection geometry can either be achieved by two dimensional (2D) raster scanning a single element transducer, or by using an array of transducers. When a linear array is used, only a line scan is required to capture the ultrasound signals at the detection plane and from a 3D image of the sample. In the same way, a 2D array can provide even faster imaging by acquiring a whole volume at once without scanning.
There are two detection concepts: imaging can either be done in-focus or out-of-focus. In the first approach, the in-focus imaging, the focus of the transducer is directly placed in the sample. The resolution is typically determined by the focal spot size of the transducer.

The second approach is imaging out-of-focus or using an unfocused detector. This can be realized by a 2D array of small unfocused piezo elements. In the case of an unfocused transducer, the lateral resolution scales with the detector size. However, not only the resolution will increase for smaller detectors but also the sensitivity will drop proportional to the detector size. The same imaging geometry can be achieved with a focused single element transducer when the focus is placed outside of the sample. In this case the focus acts as a virtual point detector. The resolution for out-of-focus imaging is not determined by the size of the transducer but by the size of the virtual detector, i.e., the focal spot size.

Besides piezo based planar detection geometries, there are also all optical detection systems. For further information on these systems the reader is referred to the review article [24]. Both optical and piezo detection can achieve an imaging depth from a millimeter to a few centimeter, depending on the sensitivity and the bandwidth of the used detector.

The planar detection/scanning geometry offers good resolution and a decent scanning speed and allows to image (shallow) region of interests from larger specimen such as mice or other larger animals [24]. However, the geometry has a major drawback. The optoacoustic signal emitted from structures is generally not isotropic but

depends on the shape and orientation of the structure. A cylindrical structure will emit most of its optoacoustic signal perpendicular to the axis of the cylinder. Therefore, vessels or other structures with a distinct direction will not be visible for the detector in case they are oriented perpendicular to the detection plane [25]. Another disadvantage is that the planar geometry typically comes with an anisotroptic resolution. The resolution in the direction of the transducer axis is typically much higher than the resolution along the scanning plane.

The resolution along the transducer axis (perpendicular to the plane) is mainly dependent on highest detectable frequency f_c of the transducer and therefore related to the frequency bandwidth of the transducer. The axial resolution R_H at the focus can be approximated with the following equation:

$$R_H = 0.8 \cdot \frac{c}{f_c}, \tag{2.1}$$

where c is the speed of sound and f_c is the maximum detectable frequency. Outside the focus the resolution will deteriorate, depending on the actual shape of the transducer.

The lateral resolution (in plane) mainly depends on the aperture of the transducer. The resolution is given by

$$R^L = \sqrt{R_H^2 + D^2}. \tag{2.2}$$

Here D is either the focal spot size (in case the focal spot is used as a virtual point detector) or the detector size in case of an unfocused transducer. For most detectors the diameter D will be much larger than the frequency depended resolution. In this cases the lateral resolution can be approximated with the transducer diameter. A more detailed description of the transducer focusing and the resolution can be found in chapter 4.3.

Two-dimensional optoacoustic tomography

In contrast to the planar scanning geometry the tomographic geometry is typically circular or cylindrical. One of the simplest implementations of a 2D tomography geometry is the rotation of a cylinderically focused transducer around the sample or vice versa (see [26]). The scanning geometry is illustrated in Figure 2.1.

The cylindrical focus of the transducer will reduce the three-dimensional imaging problem to a two-dimensional geometry by only detecting optoacoustic signals from the focal plane of the transducer. By translating the imaging plane relative to the sample a 3D image of the whole sample can be acquired. This way the good axial resolution from the transducer can be used to generate an isotropic in-plane resolution (at least in the center of the reconstruction volume).

The resolution perpendicular to the imaging plane is generally worse than the in-plane resolution and depends on the focal width D_f of the transducer:
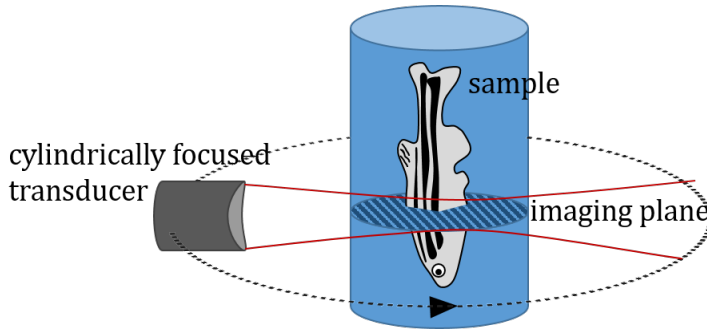
Figure 2.1: 2D optoacoustic tomography The cylindrical focus of the transducer provides acoustical sectioning. To acquire one image plane the transducer is rotated around the sample (alternatively the transducer is kept fix and the sample is rotated). By translating the imaging plane a 3D volume of the sample can be acquired. To generate an optoacoustic signal a broad and homogeneous illumination around the focal plane of the transducer is required which is mot drawn in this scanning scheme.

$$D_f = 1.4 \cdot \lambda \frac{F}{D}, \tag{2.3}$$

where F is the focal length, D the diameter of the transducer and λ the acoustic wavelength. Through the focus, acoustic sectioning is performed. Only signal from within the focal plane will be detected (more details about the focusing can be found in chapter 4.3). By using optical sectioning instead of the optoacoustic focus the resolution improves. This optical sectioning can be achieved by illuminating the sample in the focal plane of the detector with a lightsheet. However, for larger samples scattering will cause a broadening of the lightsheet and reduce the resolution.

To reduce the imaging time a (semi)circular detector array can be used instead of a single element transducer. With these detector arrays the whole imaging plane can be acquired at once, facilitating much faster imaging. The increased imaging speed can be used to acquire multispectral data, reduce motion artifacts and for imaging of (fast) physiological processes [26].

This two-dimensional geometry can be found in a variety of setups for the imaging of model organisms. The size of the imaged specimen ranges from small drosophila pupae or zebrafish [27] to larger animals such as mice [26].
The transducer frequency and of course the radius of the circular detection geometry have to be adapted to the target sample size and resolution.

Compared to the planar detection geometry the tomographic geometry acquires signals from multiple directions. Therefore, tomography offers the advantage that structures of arbitrary orientation can be detected. By reducing the 3D detection geometry to a 2D detection geometry, the time required for reconstruction shortens significantly, which facilitates real time imaging. However, because of the frequency

dependent focal width D_f of the transducer (see equation 2.3), the capability as a truly 3D imaging modality is contested [28].

### Three-dimensional optoacoustic tomography

In three-dimensional optoacoustic tomography the imaging problem is treated as a real 3D problem. Instead of restricting the acquisition to the circular detection of one plane, a truly cylindrical [29] or spherical detection surface [30] is implemented. A detection point from one cylinder plane will also detect signals originating from other planes. Similar to the previous geometries, this geometry can be realized either by a 2D array with multiple detector elements on the detection surface or by scanning of a 1D-array or a single element transducer around the sample.

Compared to the 2D tomography the image geometry offers a better resoltution along the axis of the detection cylinder or even isotropic resolution in the case of a spherical detection geometry (in the center of the detection sphere) [30, 31]. Especially for (semi)-spherical arrays rapid imaging of the whole 3D volume can be achieved, since no scanning is required. With each laser pulse a whole volumetric image can be acquired. In this way, imaging at frame rates of 100 volumes per second are possible as shown by Dean Ben et al. [32]. The fast frame rate allows the observation of fast biological processes such as neuronal activation in zebrafish with GCaMP [32] (GCaMP is a genetically encoded GFP based calcium indicator). A scan with a linear transducer array (or with a single element transducer) can not achieve the same imaging speed, but can cover much more sensor positions. The simultaneous acquisition of several hundreds of detector elements is computationally demanding, especially when high sampling frequency is required. In a scanning geometry thousands of detection points can be acquired. The higher amount of detector positions translates into a better image quality and less reconstruction artifacts.

2.1.3 Choice of scanning geometry

To match the requirements stated in section 2.1 and facilitate in-vivo imaging of developing model organisms, a hybrid SPIM and optoacoustic tomography is proposed in this thesis. SPIM imaging has proven to be an excellent tool for in-vivo imaging in developmental biology. The geometry of the optoacoustic scan has to be chosen according to the SPIM geometry. In this geometry one side is occupied by the microscope objective and the sample is illuminated from two opposing sides perpendicular to the objective (see Figure 2.2). For the optoacoustic acquisition a broad homogeneous illumination is used instead of a lightsheet. This way signals from the whole sample can be acquired at once and no scanning of the sample through the illumination plane is required.
In Figure 2.2 the sample chamber layout is shown. In dark green the lightsheet illumination is illustrated and in light green the broad optoacoustic illumination. The sample (in this case indicated by a smiley) is mounted in an agar cylinder. For samples such as zebrafish which are larger along one dimension, the long axis of
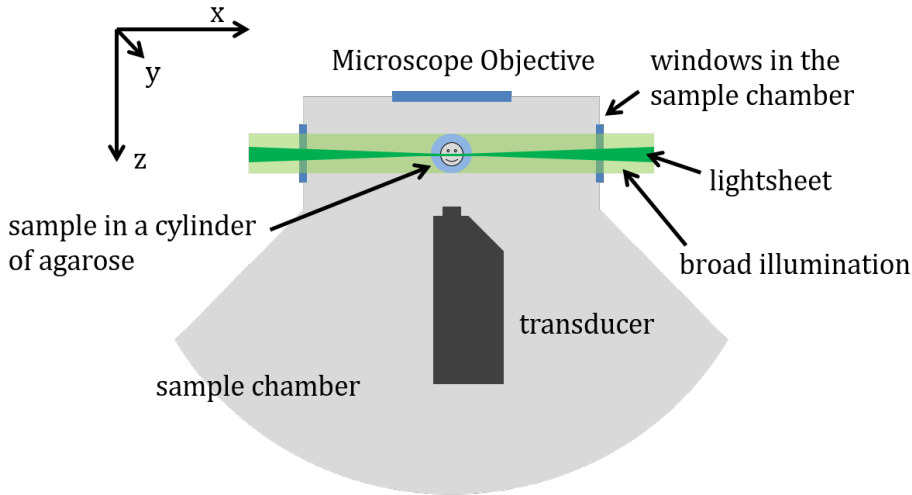
Figure 2.2: Design of the sample chamber In green the double sided SPIM and optoacoustic illumination is illustrated. The illumination enters the water-filled sample chamber through two windows to each side of the sample chamber. The microscope objective is located behind a third window perpendicular to the illumination plane. The ultrasound transducer is placed on the opposite side of the objective.

sample is orientated along the axis of the cylinder (y-axis). This way the path of the excitation light (the lightsheet) and the path of the emitted fluorescence light to the objective is minimized.

Limited by the SPIM geometry and the positioning of the sample the transducer is placed on the opposite side of the objective. For high resolution, sensitivity, and image quality a three-dimensional tomographic approach is chosen. Since the aim of this setup is rather the observation of developmental processes on longer time scales than imaging of fast physiological processes a one-dimensional array with 128 elements and a scanning geometry is chosen. The elements of the transducer are aligned along the y-axis.

Instead of a pure rotational tomographic geometry, a combination of translation (planar scan) and rotation was chosen. The transducer array is cylindrically focused in the xz-plane and the focus is placed inside the sample to achieve maximum sensitivity. Because of the focusing for each transducer position, only a small plane of the sample is covered, defined by the focal width and focal shape of the detector. By translating the transducer, a whole 3D image of the sample is acquired. However, as discussed in the section above, in this planar geometry not all structures might be visible (depending on their orientation), the resolution is anisotropic and reconstruction artifacts might reduce the image quality. Therefore, in addition to the planar scan, a tomographic scanning geometry is implemented. More precisely, two different rotational geometries where designed and tested. Both scanning geometries are depicted in Figure 2.3.

In first scanning scheme, which is illustrated in Figure 2.3a, the transducer is
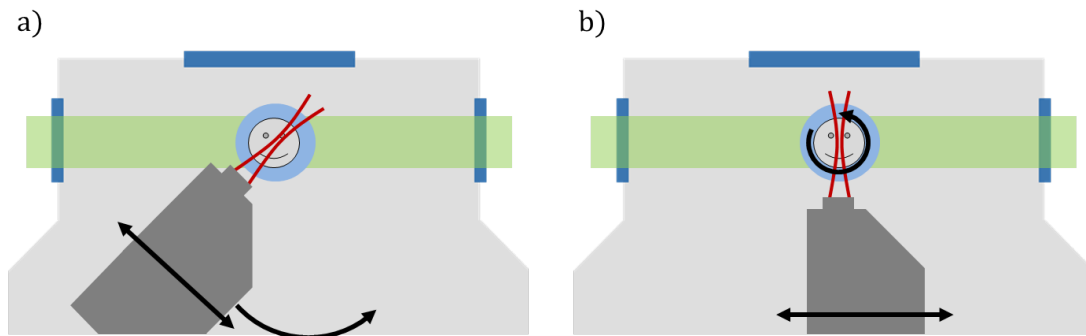
Figure 2.3: Scanning geometry Two different scanning geometries were imple-
mented: In a) the transducer is both translated and rotated. In b) the transducer is
only translated and the sample is rotated.

both translated and rotated. This has the advantage of keeping the illumination
of the sample fixed. As shown later in chapter 4.2 a homogeneous and constant
illumination is one of the assumptions which are made for the reconstruction. The
disadvantage is that due to the illumination from both sides the rotational angle is
limited to approximately 90°.

In the second scanning geometry (see Figure 2.3b) the transducer is only translated
and the sample is rotated. The advantage of this scanning scheme is that a full
360° scan can be acquired. As shown later in chapter 4.7, the advantages of a full
360° scan outweighs the disadvantages of a slightly changing illumination and most
of the measurements were acquired in this scanning geometry.

A scanning geometry which combines translation and rotation as already been
realized by Gateau et al. [29, 33]. As shown in this papers the geometry is superior
to pure rotational geometries, as they offer isotropic (in-plane) resolution over a
larger regions of sample volume.

2.2 Implementation of the scanning geometry

The hybrid character of the system implies some special design choices which can
normally not be found in other systems. The most prominent of these characteristics
is the used laser. While in conventional SPIM imaging (monochromatic) continues
wave (CW) lasers are used, optoacoustic imaging requires a pulsed laser. The pulse
width of the laser is related to the emitted optoacoustic frequencies and therefore to
the maximal resolution of the optoacoustic image. To achieve a resolution of under
$40\,\mu\text{m}$ a pulse width of around $10\,\text{ns}$ is required (see chapter 4.1.1). To take full
advantage of the multispectral optoacoustic contrast, a tunable laser is necessary.
Since most common fluorophores are designed for the visible spectrum and intrinsic
biological components such as oxy- and deoxy-hemoglobin have a characteristic
spectrum in the visible region, a laser tunable in the visible spectrum was chosen.

The requirements of more than 10 mJ and a few nanosecond pulse requires a Q-switched OPO laser system. For SPIM imaging these lasers have the disadvantage of a low quality laser focus. The axial resolution in SPIM imaging depends on the ability to focus the excitation light into a thin sheet. This ability depends on the quality of a laser beam which can be measured by the M^2 factor, which is defined as

$$M^2 = \frac{\theta r_0 \pi}{\lambda} \tag{2.4}$$

A perfect, diffraction limited beam of a circular aperture has a Gaussian shape and an M^2 factor of one. Tunable pulsed OPO-lasers usually have a beam profile which is very different from a Gaussian profile and therefore an M^2 factor larger than one. Another disadvantage of the high energy pulsed laser beam is increased photo bleaching and photo toxicity due to the differing photo dynamics of the high energy pulses.

The used laser is a fast tunable Q-switched optical parametric oscillator (OPO) laser (Spitlight-DPSS 250 ZHG-OPO, Innolas, Germany). It consists of a frequency tripled diode-pumped Nd:YAG laser as a pump beam and a non-linear optical crystal in an optical resonator.

Through second-order nonlinear optical interactions the original wavelength of the pump laser splits into two different wavelength. The frequencies of the generated light add up to the frequency of the pump light. The two different wavelength are typically referred to as signal and idler, where the light with the higher frequency (i.e. the lower wavelength) is called signal. The laser covers a spectral range from 418nm to 710nm for the signal wavelengths and 710nm to 2100nm for the idler wavelengths.

The energy of the laser is optimized for the visible range with pulse energy of approximately 18 mJ at 450 nm (later in this chapter in Figure 2.6 a wavelength dependent pulse energy plot can be found). To generate a broadband optoacoustic pulse, the pulse width of the laser is only around 7 ns. The frame rate at which signals can be acquired is given by the laser repetition rate of 50 Hz (can be tuned down to 20 or 10Hz).

Besides the laser, a second characteristic is induced by the hybrid modality of the setup. To meet the different requirements, there are the two different illumination modes. While using the same laser, the illumination for SPIM and optoacoustic is shaped by two different optical pathways.

In Figure 2.5, a 3D computer-aided design (CAD) model of the whole system is shown. The system consists of two illumination beam paths one on each side of the microscope, which can be seen in the middle of the setup. Both illumination paths are schematically depicted in Figure 2.4. The excitation beam from the laser is switched by a flip mirror (FM) to one of the two illumination paths.

Both beam paths are merged again with a polarizing beam splitter and the same optics are used to direct the beams into the sample chamber.
In the following the shaping of the optoacoustic and SPIM illumination will be discussed separately.
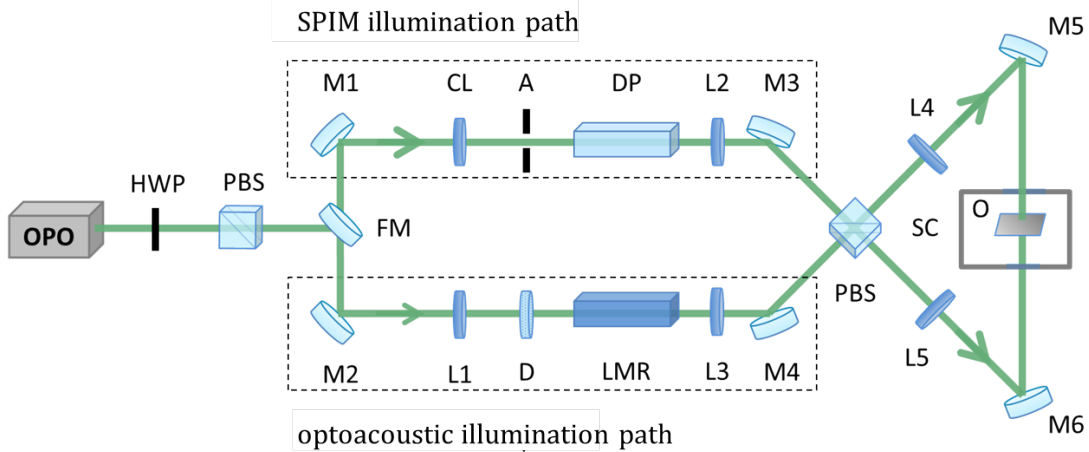
Figure 2.4: System Schematics A pulsed optical parametric oscillator (OPO) illuminates a flip mirror (FM), which is used to choose between both illuminations. The light sheet is focused by a cylindrical lens (CL) and than projected into the sample chamber with the Lenses L2 and L4/L5. The aperture (A) blocks the higher modes of the lightsheet focus and dove prism (DP) rotates the lightsheet. The volumetric illumination is formed by a light mixing rod (LMR). Lens (L1) and the diffusor (D) focus and homogenize the beam before the input of the LMR. The output is then projected into the sample chamber with the Lenses L3 and L4/L5. Power and polarization are adjusted using a half-wave plate (HWP) and polarizing beam splitter (PBS). A second PBS splits the beam 50:50 before illuminating the object (O) in the sample chamber (SC).

2.2.1 SPIM illumination and acquisition

Figure 2.5b shows the optics of the SPIM illumination. The optical component which will determine the actual shape of the lightsheet is the cylindrical lens (CL). The numerical aperture (NA) of the lens defines the width of the focus, i.e. the width of the lightsheet. Lenses with a NA will create a thinner lightsheet at the center of the sample volume. Since the beam diameter d_b is fixed, the NA can be defined as

$$\text{NA} = \frac{d_b}{2f}, \tag{2.5}$$

where f is the focal length of the lens. However, this is only valid as long as the lens diameter is larger than the laser beam profile. The focal width D_f can be approximated as [34]

$$D_f = \frac{\lambda}{2\text{NA}} = \frac{f \cdot \lambda}{d_b}. \tag{2.6}$$

However, with a smaller focal width also the focal length will decrease. The lightsheet thickness will increase rapidly when leaving the central region, limiting the effective field of view which can be used for imaging. The focal length L_f is given by [34]

$$L_f = 2n\frac{\lambda}{(\text{NA})^2} \tag{2.7}$$

Lenses with a larger focal distance will create a thicker lightsheet but the lightsheet thickness will diverge more slowly. The choice of the right focal length is therefore always a trade off between lightsheet thickness, which directly translates into axial resolution, and potential sample width. If not mentioned otherwise, the images shown in chapter 3.4 were imaged with a 30 mm lens. For bigger samples the setup offers the possibility to exchange the cylindrical lens.

Directly in the focal point of the cylindrical lens (CL) an aperture slit (A) is mounted. The slit is used to block higher modes of the line focus and therefore narrow down the thickness of the lightsheet.

The "cleaned up" focal line is projected into the sample chamber by a 4f-optics with a magnification of one by the lenses L2 and L4/L5.
The lightsheet in the sample chamber has to be vertically orientated to match the focal plane of the objective. To achieve such a vertical orientation, the lightsheet has to be rotated. This rotation is realized by a dove prism (DP). The prism has a trapezoidal shape. An incoming beam undergoes a total internal reflection, flipping the beam coming out of the prism. When the prism is rotated the transmitted beam is rotated at twice the angle. In this way an arbitrary orientation of the transmitted beam can be achieved. To align the lightsheet parallel to the focal plane, a 45° rotation is realized by the prism.

In Figure 2.5c and 2.5d the splitting of beam path and the two sided illumination can be seen. A polarizing beam splitter (PBS) is dividing the beam, transmitting half of it and reflecting half of it at 90°. In order to split the beam in a 50:50 ratio the linear polarization of the beam has to match the correct angle. This angle is adjusted by a half wave plate (HWP) and a polarizing beam splitter (PBS) which are mounted in front of the laser.
The divided beam is directed into the sample chamber, which is filled with water. Both lightsheets enter the chamber through two windows, one on each side (see Figure 2.5c).
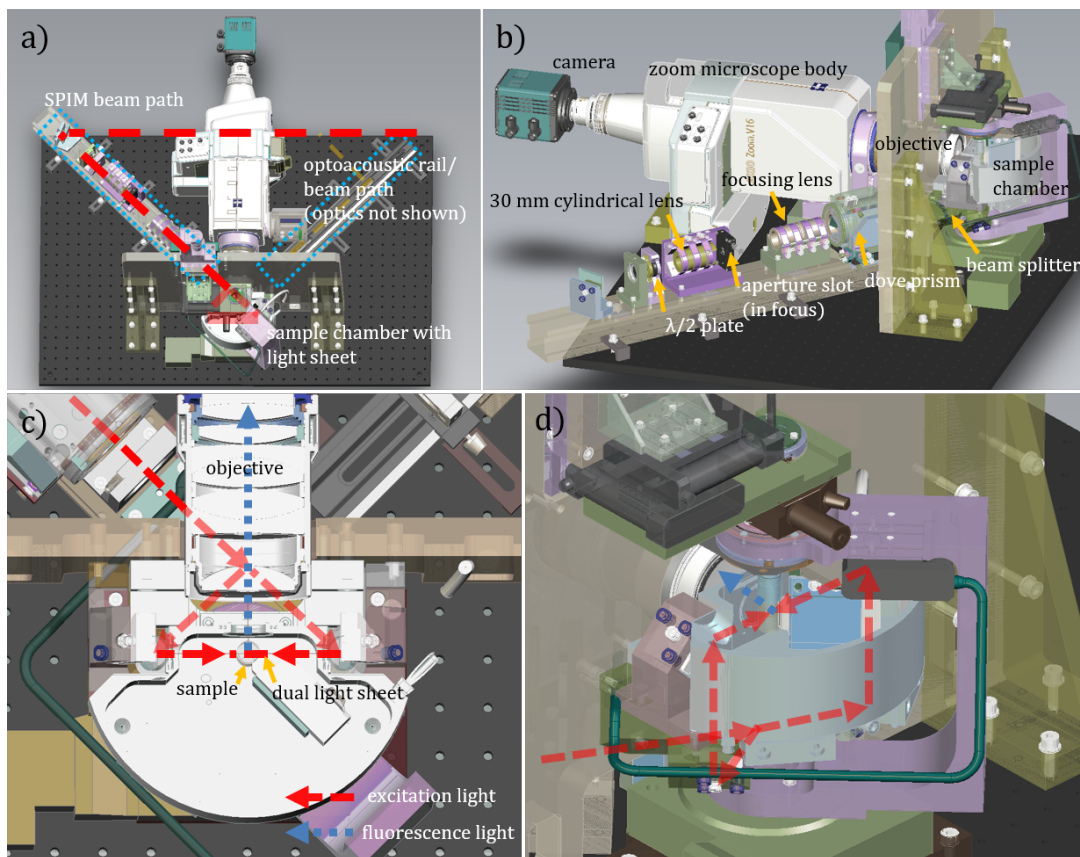
Figure 2.5: CAD of SPIM illumination a) top view of the setup. The excitation beam (red) enters the system at the top right. The SPIM optics are on the left optic rail. b) side view of the setup with labeling of the beamforming components on the optical rail. c) top view on a cut through the sample chamber and the objective. The fluorescence (blue) is emitted from the sample and detected by the objective. d) close-up side view of the sample chamber. The sketch illustrates how the excitation light is directed into the sample chamber

The sample is mounted on a holder which is attached to 4 motorized stages - three translational stages to cover all three dimensions and a rotational stage. The three translational stages allow the positioning of the sample as well as scanning the sample through the lightsheet. The rotational stage can - besides positioning - be used to image the sample from multiple directions, and later for optoacoustic tomographic acquisition. The principle of the SPIM acquisition and a general scanning scheme will be explained in-depth in the chapter 3.

The fluorescence emitted from the sample is collected by a custom made ZEISS Apo Z $1.5\times/0.37$ FWD 30mm objective located behind a window in the sample chamber. The objective is corrected for spherical aberrations induced by water in the sample chamber. With the attached zoom microscope (Axio Zoom.V16, ZEISS) magnifications from $1.05\times$ - $16.8\times$ can be achieved. The NA of the system varies between 0.052 for the lowest and 0.374 for the highest magnification. The large range of magnifications allow the imaging field of view to either cover the whole

maximal sample volume, or zoom into the middle of the sample volume for smaller samples. Within the microscope, different emission filters are mounted in a filter turret. For the following measurements of green fluorescent protein (GFP) labeled samples an excitation wavelength of 488 nm in combination with a 515/10 bandpass filter as an emission filter is used. The specific optical design and the manufacturing of the system components were done by ZEISS (Carl Zeiss AG, Jena, Germany). All optical components were optimized for the visible range between 400 - 700 nm.

The images are recorded by an sCMOS camera (pco.egde, PCO, Kelheim, Germany) which is mounted on the microscope. The camera sensor has 2560×2160 pixels and an extremely low readout noise. The exposure time ranges between 500 µs - 2 s. In the actual measurements the exposure time was adjusted to the amount of fluorescent signal and typically is between 100 ms - 500 ms. For these exposure times it is ensured that multiple laser pulse hit the sample during the image acquisition (at a repetition rate of 50 Hz a laser pulse hits the sample every 20 ms).
Acquisition of the images and controlling of the motor stages is performed with Matlab (Mathworks, Natick, MA, United States) and the raw data is saved as a .tiff image stack for further computational processing.

2.2.2 Optoacoustic illumination and acquisition

The scheme of the optoacoustic illumination beam path can be found in Figure 2.4. A homogeneous illumination of the sample as well as a high energy per area are important for optoacoustic mesoscopy. An inhomogeneous beam profile would lead to artifacts in the reconstruction (see chapter 4.1) For this reason, a light mixing rod (LMR) is used in this setup to achieve a homogeneous illumination. The light mixing rod further offers the advantage of a rectangular beam profile. Since the sample volume is cylindercal with the illumination being perpendicular to the cylinder axis, the rectangular shape will optimize the illumination level of the FOV and lead to a higher laser energy per area. The laser beam is focused by lens L1 on one side of the light mixing rod. A diffuser in front of the light mixing rod homogenizes the beam pattern and the light mixing rod is creating a sqaure-shaped output. This square-shaped homogeneous beam profile is projected into the sample chamber with a 4f-imaging system by the lenses L3 and L4/L5 (similar to the lightsheet). The magnification of the 4f-imaging system can be adapted by changing the focal length of lens L3. This way the width of the illumination can be adapted to the sample size, achieving a higher energy per area for smaller samples. Similar to the lightsheet illumination, the beam is split by the polarizing beam splitter to obtain an even illumination from both sides of the sample.

When the sample is illuminated with a laser pulse, an optoacoustic signal is generated. This optoacoustic wave is detected by the ultrasound transducer placed in the sample chamber (see Figure 2.2). The transducer is composed of 128 elements and each element will convert the pressure wave at its position into an analog (voltage) signal. The exact scanning geometry is described in section 2.1.3.

The acquisition and digitalization of the signal was performed using a 128-element data acquisition system (DAQ) operating at 125 Msamples/s at a frame rate of 50 Hz (iTheraMedical GmbH). While the Nyquist–Shannon sampling theorem states that theoretically frequencies at half of the sampling frequency (62.5 MHz) can be detected, the DAQ has a built in anti-aliasing filter which restricted the bandwidth of the signals to 45 MHz. Similar to the SPIM scan, the acquisition was controlled and performed with Matlab. Reconstruction of the raw data was also performed in Matlab.

2.2.3 Alignment of both modalities

For SPIM imaging it is critical that both lightsheets are aligned exactly in the focal plane of the microscope objective, with the focus of the lighsheets at the center of the focal plane. An offset in one of both lightsheets or a tilt will result in out of focus light, an inferior axial resolution or a reduced FOV. The alignment is done mechanically with the mirrors next to the sample chamber and the position of the focusing lens.

In order to facilitate hybrid imaging and simplify image co-registration between both modalities, the optoacoustic system was aligned according to the SPIM system. The rotational axis of the sample was adjusted to the focal plane and the center of the objective. The optoacoustic illumination was adjusted as well to this central axis. The mirrors could not be used for alignment without altering the position of the lightsheet. Hence, the focal lens, which projects the output of the light mixing rod into the sample chamber, was mounted in a translation mount. By translating the lens perpendicular to the beam path, the position of the optoacoustic illumination could be adjusted.

The mechanical alignment of both systems ensures an optimal overlap of both FOVs. However, the mechanical alignment will not be sufficient to achieve a perfect correspondence between both imaging modalties. The fine adjustment was performed after the data acquisition and reconstruction computationally, by a rigid transform of the 3D datasets.

2.3 Characterization of the illumination

In this section the illumination of the system will be characterized. The focal width of the lightsheet which can be achieved is dependent on the quality of the laser beam and on the NA of the focusing lens. Equation 2.6 is only valid for a Gaussian shaped beam. The more the laser beam deviates form the Gaussian beam, the more the actual lightsheet width will deviate from the theoretical prediction. The homogeneity of the illumination profile in the sample chamber will further-more affect the quality of the optoacoustic reconstruction. An inhomogeneous laser beam profile requires additional beam shaping optics to achieve an optimal optoacoustic illumination. This homogenization of the beam is done by a diffu-

sor and a light mixing rod, which produces a homogeneous rectangular beam profile.

In the next sections the laser profile, the SPIM illumination, and the rectangular optoacoustic illumination will be characterized.

2.3.1 Laser profile

The laser beam quality will also determine the size and quality of the beam focus after a lens. The quality of a (laser) beam can be characterized by the M^2 value. It is defined as the ratio of beam parameter product (BPP) to the BPP of a Gaussian beam with the same wavelength. The BBP is the product of the half-angle beam divergence θ and the radius of the beam at the beam waist r_0. For a perfect Gaussian beam the BBP is given by λ/π. Therefore the M^2 value of a beam is defined as $M^2 = \theta r_0 \pi/\lambda$.

In a OPO laser system the selection of the wavelength is done by tuning the nonlinear crystal and the beam profile varies heavily for the different wavelength. This can be seen in Figure 2.6 where the profile of the laser beam for 488 nm, 550 nm and 600 nm are plotted.
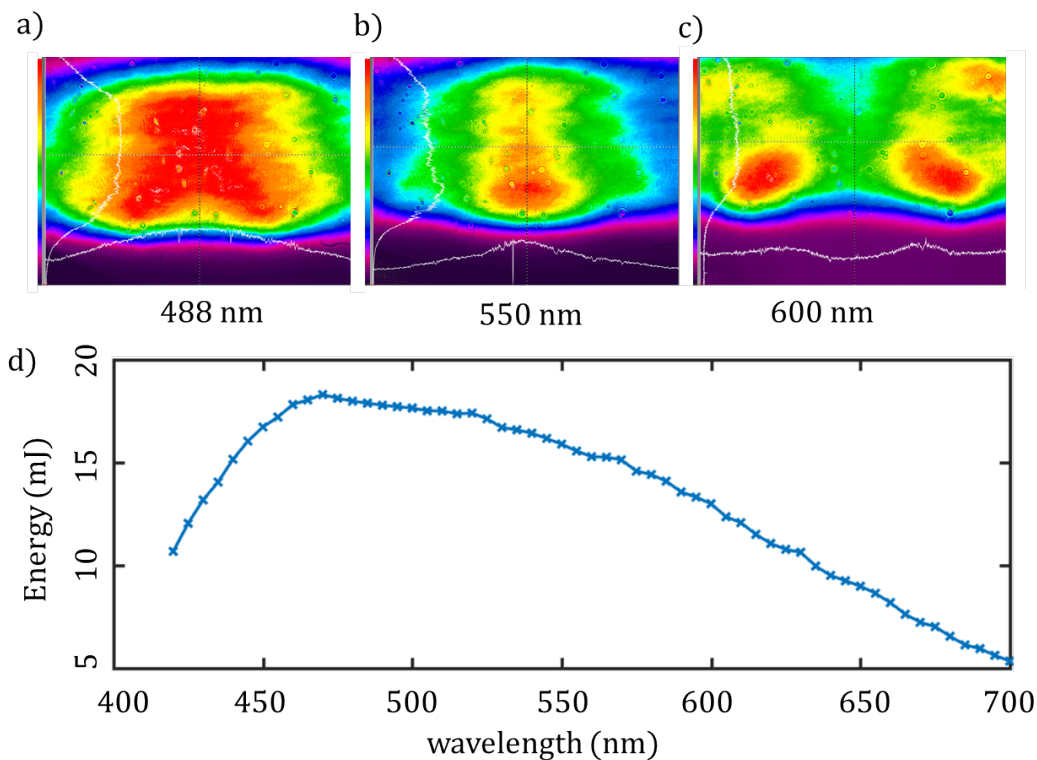
Figure 2.6: Laser beam characteristics a)-c) show the laser beam profile at 488 nm , 550 nm and 600 nm respectively. In d) the laser energy is plotted against the wavelength of the laser.

While the profile at 488 nm and 550 nm still show some characteristics of a stretched Gaussian beam with the first transverse electromagnetic mode (TEM$_{00}$) being the

primary mode of the laser beam, at 600 nm other TEMs become more dominant. Furthermore, a drift in height can be observed in Figure 2.6a-c. The M^2 value will be calculated with the focusing characteristics of the lightsheet, which are presented in the next section.

Besides the changes in the beam profile, the energy of the laser will also vary with the wavelength. In Figure 2.6d the laser energy is plotted against the wavelength of the laser in the visible range (for the signal part of the laser spectrum). Because of strong fluctuations in the laser energy on multiple timescales, each point of the curve is a one second average and the whole curve was smoothed with a moving average filter of 3.

The energy curve has to be considered in optoacoustic imaging when spectral imaging is performed. The recorded signal in optoacoustics is proportional to both the absorption coefficient in the sample and the energy of the illumination. To determine an absorption spectrum from a component of the sample, the measured signal has to be corrected by the laser energy for the specific wavelength.

In the experiments this correction can be done by normalizing the signal strength by the shown energy spectrum. However, the laser energy fluctuates in time. The pulse to pulse fluctuations of the laser will normally average out. But there are also fluctuations in the laser energy due to the temperature of the laser and the cooling systems, which take place on larger time scales and might affect the measurement.

Finally the laser optics degrade over time. This degradation will first affect the light with shorter wavelengths, since the higher energy of the photons with shorter wavelengths is more likely to damage the optics in the laser. The degradation of the optics effectively changes the spectrum over time and requires recurring power calibration measurements.

It has been shown advantageous to use a second approach for energy calibration. The laser energy can be calibrated within the measurement by placing black absorbing polystyrene micro beads next to the sample. These beads have almost a flat absorption spectrum in the visible range. By normalizing the reconstructed intensity of the beads, the laser energy distribution can be corrected.

2.3.2 Lightsheet characterization

In this section the lightsheet illumination will be characterized. The lightsheet is focused using a 30 mm cylinderical lens (see section 2.2.1). The focusing of the lightsheet is always a trade off between mimimal width (i.e. the axial resolution) and the length over which this high resolution can be achieved. By using high NA lenses for focusing, narrow lightsheets can be generated. Although thin at the focal region, these lightsheets will quickly diverge outside of the focus, which limits the possible imaging width. To measure the lightsheet thickness two methods where used. In the first measurement a silver mirror in the sample chamber mounted at

45° was used to reflect the lightsheet into the objective and directly measure the full width at half maximum (FWHW). In the second approach a phantom with multiple fluorescent nano beads was used.
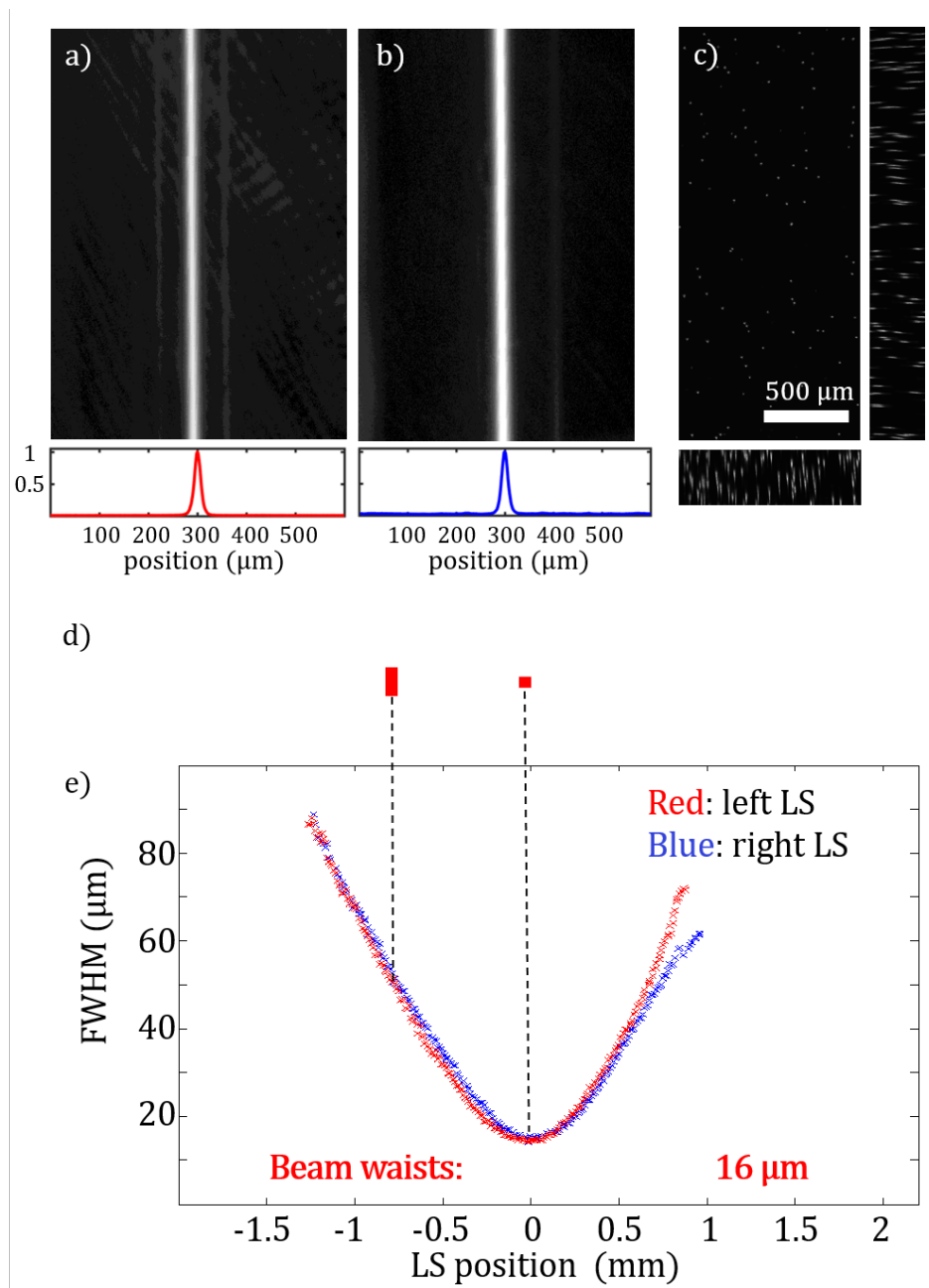
Figure 2.7: Measurement of the lightsheet width a) profile image of left lightsheet with a cross-section plotted below. b) profile image of the right lightsheet c) MIPs of a fluorescent nano bead sample from all three directions in space. d) plot of the lightsheet width against the distance to the focus. On top of the plot the schematic shape of the lightsheet is depicted.

The silver mirror is mounted on a precisely manufactured calibration sample, which

will later also be used for other system analysis. By moving the tilted mirror parallel to the lightsheet along the x-axis, a profile image of the lightsheet for different positions along the propagation direction can be recorded. The profile image of the focus region can be seen in Figure 2.7a and b. Since the lightsheet illumination is two-sided the profiles of both lightsheets were analyzed independently. The image in Figure 2.7a shows the left lightsheet, the image in Figure 2.7b shows the right lightsheet. Underneath both images a cut through the middle of the image is plotted. A Gaussian profile was fitted to the profile to determine the width of the lightsheet. When moving the mirror back and forth (parallel to the lightsheet) the broadening of the lightsheet can be observed in the profile image. This thickening of the lightsheet on both sides is shown in Figure 2.7d. On top of the panel the lightsheet shape is schematically drawn. The plot in Figure 2.7e shows the FWHM (again fitted with a Gaussian) plotted against the relative distance to the focus. In the center both lightsheets reach a beam waist of about 16 μm.

With this measurement the M^2-factor at the used wavelength of 488 nm can be determined. A line is fitted onto the diverging beam to calculate the half divergence angle θ. Both values, the beam waist r_0 of 16 μm and the half opening angle are inserted into equation 2.4 which results in an M^2-factor of 7.8. The wavelength 488 nm was chosen for a closer analysis, because it is most commonly used for SPIM imaging in this thesis (due to the absorption peak of GFP at 488 nm) However, it should be noted, that the beam profile at 488 nm is much closer to a Gaussian profile than the beam profile at 600 nm (see Figure 2.6a and c) which will result in a higher M^2 factor for higher wavelengths.

The measurement of the lightsheet thickness was repeated with a bead phantom. Fluorescent nano beads with a diameter between 0.2-0.3 μm were embedded in a 5 mm diameter agarose cylinder and the sample was scanned through the lightsheet. The resulting image volume can be seen in Figure 2.7c. The three images show the maximum intensity projection (MIP) of the volume from all three directions in space. By plotting the profile and fitting a Gaussian to it, the FWHM was determined. Unlike the previous measurement the sample points in space are distributed randomly in space. The minimum width measured with this approach was 34 μm for the left lightsheet and 27 μm for the right lightsheet. The discrepancy of the mirror measurement and the bead measurement is presumably due to the agarose. Although quite transparent, some light will be scattered in the agarose resulting in an effectively broader lightsheet. The non equidistant sampling and the small amount of sampling points in the center of the focus might also affect the minimal measured width.

2.3.3 OA broad field illumination characterization

To compensate for the inhomogeneous laser beam profile and to achieve a homogeneous illumination over the whole FOV, a light mixing rod (LMR) and a diffusor are used. The light mixing rod creates a homogeneous square-shaped output profile by multiple total internal reflections of the beam within the rod. The rectangular

illumination shape matches the FOV of the transducer and will therefore optimize the yield intensity.
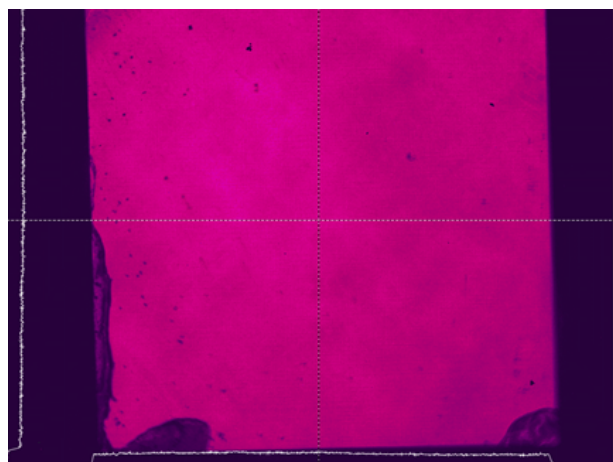
Figure 2.8: OA illumination profile The output of the light mixing produces a homogeneous beam profile. The image height is 5mm . The discrepancies at the bottom of the beam profile are generated by defects on the surface of the light mixing rod.

A measured beam profile of the optoacoustic illumination is shown in Figure 2.8. For this profile the magnification of the 4f-imaging system which projects the output profile into the sample chamber was chosen to equal one. The 5 mm length of the illumination profile could not be fitted completely onto the beam camera, which has a width of only 5 mm. However, the shown beam profile confirms the homogeneity of the beam over the whole length. During the assembly of the system, the rod was damaged on two corners, which is visible in the beam profile. Furthermore, some small impurities can be seen on the surface of the LMR.

2.4 Characterization of the resolution

Resolution in an imaging system is defined as the minimal distance between two objects, so that the two objects can still be distinguished. The resolution will determine what details can be seen in an imaging system and is therefore one of the crucial parameters when choosing an imaging system for a certain application. In the presented setup a large range of sample sizes will be covered, from small embryos of only a few hundred micrometers to juvenile or adult samples of several millimeters. To be able to measure small samples of only 100-200 µm, the resolution of the system has to be sufficiently high.

2.4.1 SPIM resolution

Lateral resolution

Similar to most other techniques in light microscopy, the resolution of SPIM is diffraction limited. This fact was already described by Ernst Abbe in 1873 [35].

According to him the minimal distance d between two objects, which is still resolvable is given by

$$d = \frac{\lambda}{2n \sin \alpha} = \frac{\lambda}{2\text{NA}}.$$ (2.8)

Here λ is the wavelength of the light and NA the numerical aperture of the objective. The resolution criteria is valid for objects in the focal plane of the objective and therefore describes the lateral resolution of a microscope. If the image is under-sampled by the detecting camera, the lateral resolution will not be diffraction limited anymore. In this case the pixel size of the camera determines the lateral resolution.

To effectively measure the size of an object and determine the resolution of the system, the exact magnification and pixel size of the detector must be known. Therefore the size of an image pixel will be measured depending on the magnification of the system. The size of an image pixel was determined by a resolution target on the calibration sample. For this purpose the size of different structures on the resolution target was measured multiple times with different magnifications. Since the real size of the structures on the targets is known, the effective size of one image pixel can be calculated for different magnifications. The image pixel size for the smallest magnification of 1.05× was determined to be 6.15 µm, while the pixel size for the largest magnification of 16.5× was measured to be 0.38 µm. Overall 5 different magnifications were measured. The image pixel size for an arbitrary magnification was interpolated from these measurements.

To experimentally determine the lateral resolution, the same fluorescent bead sample, which was previously used to determine the width of the lightsheet (see Figure 2.7), can be used. Since the nano beads are much smaller than the resolution limit of the microscope they can be assumed to be point sources. However, the measurement will suffer the same effect as the previous measurement - scattering inside the agarose. The maximal resolution found with the highest magnification of 16.5× which could be measured with the fluorescent nano beads is 1.15 µm. Since the size of the nano beads (0.2-0.3 µm) is significantly smaller than the expected resolution, the FWHM of the measured signal can be assumed to resemble the resolution of the optical system. However, due to the scattering of the agarose, the measured resolution will be larger than the minimal lateral resolution of the pure objective and the camera. The measurement still gives an impression of the performance of the setup, since all samples will be embedded in agarose.

Axial resolution

In SPIM the lightsheet provides optical sectioning and greatly reduces out of focus light. Furthermore, it will improve the axial resolution if the lightsheet thickness is smaller than the axial resolution of the objective, which is given by

$$d = \frac{2\lambda n}{\text{NA}^2}.$$

(2.9)

For the lower magnifications of the objective this criteria is met and the axial resolution is given by the thickness of the lightsheet of 16 µm which was measured in section 2.3.2. If the lightsheet is not scattered and the FOV is not exceeded only fluorescence form the focal plane will be detected. If the axial resolution of the objective is smaller than the lightsheet, the lightsheet will exceed the width of the focal plain and create out of focus light. The light from outside the focal plane will reduce the contrast and make it more difficult to visualize smaller structures. Therefore, the width of the lightsheet will be used as a lower estimation of the axial resolution.

2.4.2 OA resolution

Here the resolution of the optoacoustic system will shortly be discussed. A more detailed analysis of the PSF and the resolution of the optoacoustic system can be found in chapter 4.6. Due to the detection geometry the resolution is expected to be anisotropic in the horizontal and vertical direction. While the theoretical resolution in the horizontal plane is is given by equation 2.1, the resolution along the vertical y-axis will be lower, as seen in equation 2.2. However, the theoretical resolution does not necessarily correspond to the actual resolution in the system. Therefore the resolution was determined experimentally with 20 µm beads (see chapter 4.6). In the horizontal direction a resolution of 35 µm and in the vertical direction 120 µm was measured.

3 SPIM

The principle illumination scheme behind modern lightsheet microscopy was already developed in 1902 by Henry Siedentopf and Richard Adolf Zsigmondy, working for the company Carl Zeiss, as an extreme darkfield micrcoscope under the name ultramicroscope [20]. However, the technique was largely forgotten for the better part of the 20th century. With the arrival of new fluorescence labels and imaging techniques the principle of ultramicroscopy was rediscovered. In 1993 Voie et al. [36] applied the technique to fixed and cleared tissue as Orthogonal-plane Fluorescence Optical Sectioning (OPFOS), but unfortunately received little attention. Similar to OPFOS, Fuchs et al. presented Thin Laser Sheet imaging microscopy (TSLIM) in 2002 [37]. Only when Huisken et al. in 2004 [9] presented Selective Plane Illumination Microscopy (SPIM), the technique became recognized by a larger community. In the article from Huisken et al. zebrafish embryos were imaged in-vivo with SPIM, already showing the potential of this technique for imaging small developing model organisms. Since this first publication, lightsheet microscopy has been used in several image applications and the technique has been improved in acquisition speed, imaging depth and resolution [12, 38]. Since a few years several SPIM microscope systems are commercially available.

SPIM or lightsheet microscopy is based on the illumination of the sample by a thin lightsheet from the side of the sample. The principle geometry can be seen in Figure 3.1.
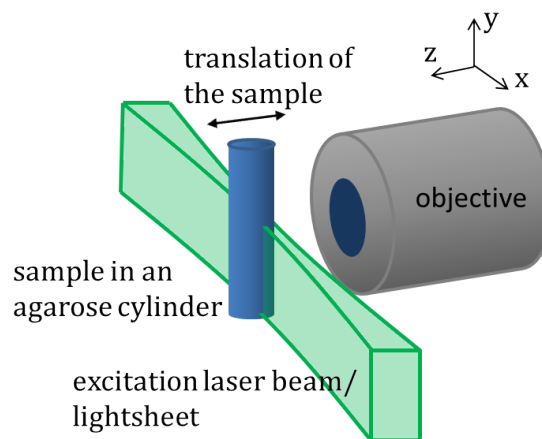
Figure 3.1: Schematic SPIM setup: The sample is placed in a cylinder of agarose (here in blue) and translated through the lightsheet. The fluorescence from the sample is detected by the objective perpendicular to the lightsheet plane.

In the easiest implementation, the lightsheet is formed by a cylindrical lens and the

sample is scanned through the lightsheet along the z-axis. The emitted fluorescence from each plane of the sample is detected by a microscope objective perpendicular to the lightsheet. In this way a 3D image stack of the sample is acquired. However, since the conception of the first SPIM system, a variety of different modifications to the basic geometry haven been presented.

Instead of illuminating the sample with only one lightsheet form one side, two counter propagating lightsheets can be used [11]. A double sided illumination offers reduced shadowing artifacts and a more even illumination of the detection plane. Another modification to the illumination is introduced in the in Digitally Scanned Light Sheet Microscopy (DSLSM). Here, the sample is not illuminated with a whole lightsheet, but alternatively with a generic pencil beam which is rapidly scanned along one dimension (along the y-axis). This geometry allows for the use of different beam illumination patterns. Instead of a generic Gaussian beam, Bessel [39] or Airy [40] beams can be applied. These beam profiles can reduce the influence of scattering and absorption in the sample even further and increase the imaging depth and quality especially for larger samples.

Besides the "self-healing" properties which lead to the reduced vulnerability towards absorption and scattering, the Bessel and Airy beam patterns offer another advantage over the regular Gaussian beam. In order to generate a lightsheet of the same sickness over the whole field of view, typically low NA lenses or objectives are used to focus the lightsheet (or the pencil beam) into the sample chamber. The low NA results in a longer focal length (along the x-axis) but will also increase the width of the focus and therefore lower the axial resolution. This limitation can be overcome by different beam forms such as Bessel or Airy beams as recently shown by Vettenburg et al. [40]. As shown in this publication, Airy beams can yield up to a tenfold larger field of view compared to a Gaussian beam lightsheet.

Similar to the approach of structured illumination microscopy [41], a modulated beam pattern can also be used in lightsheet microscopy. In structured illumination Digitally Scanned Light Sheet Microscopy (DSLM-SI) [42] the sample is illuminated with changing beam pattern to discriminated scattered background fluorescence and increase the contrast.

Another way of increasing imaging depth is combing SPIM with two-photon imaging [43]. Analog to the raster (or laser) scanning two-photon excitation microscopy non-linear effects at the focus of the laser beam cause two photons of a higher wave length to excite fluorophores at half of the excitation wavelength. In two-photon SPIM imaging this approach is combined with the long pencil focus and the scanning geometry of DSLSM. The two-photon excitation minimizes influence of scattering on the lightsheet thickness and therefore improve the axial resolution for larger or highly scattering samples. However, the emitted fluorescence photons will still be scattered on there way the objective, blurring the acquired image.

In the absence of scattering the axial resolution in SPIM imaging is given by the width of the lightsheet and the lateral resolution is determined by the microscope

objective. Therefore, the resolution is highly anisotopic, with a high lateral and a lower axial resolution. Since the sample is mounted freely rotatable in front of the objective in most of the SPIM systems this limitation can be overcome by imaging the sample from different angles [44, 45]. When this approach is combined with advanced registration [46] and fusion algorithms [47] isotropic resolution can be achieved.

Rotating the sample in multi-view SPIM and acquiring multiple views of the sample greatly increase imaging depth and resolution. However, it is not suited for fast imaging. This disadvantage can be overcome by using multiple detection objectives. In [48] Krzic et al. realize a detection from both sides of the sample (perpendicular to the illumination plane), which allow for fast multi-view imaging. To acquired even faster multi-view images form direction which are perpendicular to each other, the illumination and detection can be is alternated between the different objectives [49, 50]. In this geometry it is not necessary anymore the rotate the sample to achieve an isotropic resolution in both directions.

Although the different modifiactions of the original SPIM system improve the imaging quality and depth the scattering of light still sets a fundamental limit to the maximum imaging depth. To track the development of samples until they reach a size of several millimeter in width, other approaches like the proposed hybrid optoacoustic imaging modality are necessary. However, the aim of this project is not to monitor the development with one modality up to a point in time where the sample gets to large and then switch to the second modality, but to provide a real hybrid modality and complementary contrast. To achieve this, the overlap between SPIM and optoacoustic imaging has to be as large as possible. Therefore intensive efforts were made in this thesis to increase the imaging depth of SPIM.

As listed above there are several hardware adaptions which can improve the SPIM imaging depth, however for this first proof-of-concept hybrid setup a standard SPIM illumination was chosen (also due to the poor laser beam profile quality). Instead, the focus of this work was to increase the image quality and image depth by computational reconstruction algorithms.

Reconstruction algorithms based on deconvolution are widely used in microscopy in general and more specific for multiview SPIM image fusion [47]. However, these algorithms usually rely on multiple views of the sample and more importantly do not incorporate a model for the scattering inside the sample. In this work a prior and a new regularizer are introduced for deconvoltion of SPIM images.

To understand the principle behind the deconvolution algorithm a short introduction into image formation and the point spread function (PSF) will be given, followed by a detailed explanation of the deconvolution algorithm itself and the newly introduced prior and regularizer.

3.1 PSF

Every imaging system is limited in its ability to represent reality. The projection of a real object is always distorted by unwanted influence coming from the imaging device or from influences like scattering which are inherent in the physical imaging process. The most widely used model to describe these effects is the point spread function (PSF). The aim of the reconstruction algorithm presented in this chapter is to model the influence of scattering on the PSF. With an accurate estimation of the PSF a better reconstruction for the real object can be found, which can effectively increasing the maximum imaging depth.

The PSF describes the response of the imaging system to a delta-function or a point source. In fluorescence microscopy and other incoherent imaging modalities, the imaging formation is a linear process. Due to the non-interactive properties of photons, the imaging process of different objects is independent of each other, meaning that the sum of both objects imaged separately corresponds to the image of both objects combined.

$$I(O_1 + O_2) = I(O_1) + I(O_2), \tag{3.1}$$

where $I(O)$ is the image of an object O. Because the imaging process is linear, I can computed, by summing up smaller parts of the image. If the image is decomposed into single points, the image formation process can be seen as the sum or rather the integral of a point-wise multiplication with the point spread function of the system, which mathematically corresponds to a convolution of O and the PSF P:

$$I(x,y) = O * P + N = \int \int O(u,v)P(x-u,y-v)\mathrm{d}u\mathrm{d}v + N(x,y), \tag{3.2}$$

where N is the noise introduced to the imaging system. The name point spread function comes from the fact, that a point (of light) in the object function is spread out to a finite size in the acquired image. The image formation process as a convolution between the PSF and the object is illustrated in Figure 3.2.


<center>object   PSF   image</center>
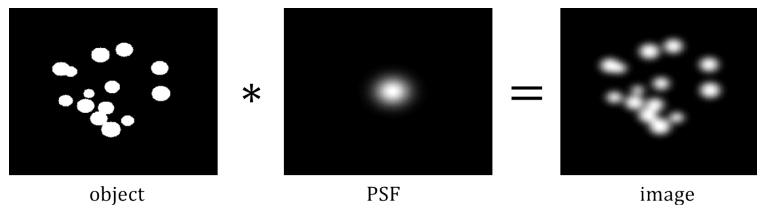
Figure 3.2: Convolution Scheme The image formation of the image (I) can be seen as a convolution between the (real) object (O) and the PSF (P).

In the case of fluorescence microscopy the object (O) is the distribution of the fluorophores in the sample. In the following the image formation in SPIM and the

related PSF will be explained.

In SPIM the sample is illuminated with a thin sheet of light. To acquire a whole 3D image of the sample the lightsheet and the sample are moved relative to each other. The direction of movement will be denoted as the z-direction, while the imaging plane will be labeled xy-plane. Accordingly the z-index of the variables indicates the current z-plane of the light sheet. The overall PSF of the SPIM system has three major contributions, which together determine the final image on the camera: the illumination function P_{illum}, the scattering PSF P_{scatt}, and the detection function of the microscope P_{det}. All three functions are going to be explained in more detail.
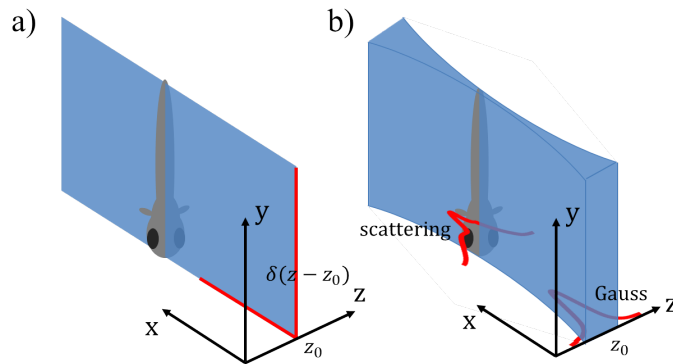
Figure 3.3: Scheme of the illumination function a) the "perfect" lightsheet illumination function is given by a delta-function. In this case only the plane z_0 is illuminated. b) in reality the lightsheet illumination function has a finite width and a specific shape (for example Gaussian). Furthermore the illumination light get scattered on the way through the sample resulting in an even larger width and a distorted shape.

Illumination function

The first contribution is the illumination function of the system. Figure 3.3 illustrates the illumination geometry and the illumination function. This function includes the shape of the lightsheet as it is formed by the focusing optics, which is sample independent. For an "ideal" infinite thin lightsheet that illuminates only a single x-y plane, P_{illum} would be a δ-function:

$$\underset{\text{recorded Image}}{I_{z_0}(x,y)} = \left(\int \int \int \underset{\text{object}}{O(x,y,z)} \underset{\text{illumination}}{\delta(z-z_0)} \underset{\text{scattering}}{P_{scatt}(x,y,z,z_0)} \, \mathrm{d}x\mathrm{d}y\mathrm{d}z \right) * \underset{\text{detection}}{P_{det}} \quad (3.3)$$

This case is depicted in Figure 3.3a. Since a convolution with a δ-function will yield the original function, the illumination function will choose a single plane from the object. In a real system, of course, the lightsheet will have a finite width and a certain profile. The profile is often a Gaussian profile, but other beam profiles such as a Bessel beam [39] have been realized as well. Figure 3.3b depicts the case of a

Gaussian lightsheet illumination. Besides the original beam profile the illumination PSF includes the deformation of the lightsheet within the sample. Due to scattering, absorption and optical refraction, which is present even in non-scattering samples, the lightsheet will change its shape. This change will vary for different samples as well as for different z-planes in the sample. Considering both a real beam profile and the scattering of the illumination light in the sample equation 3.3 generalizes to:

$$I_{z_0}(x,y) = \left(\int \int \int O(x,y,z) P_{illum}(z - z_0) P_{scatt}(x,y,z,z_0) \mathrm{d}x\mathrm{d}y\mathrm{d}z \right) * P_{det} \qquad (3.4)$$

P_{illum} describes the light distribution within the sample. Fluorescence light will only be emitted by fluorophores which are covered by the illumination function of the current z-position.

Scattering function

The second contribution is the scattering of the emitted fluorescence photons. The fluorescent molecules are sufficiently small to be considered point sources. For deeper z-planes within the sample the emitted photons have to travel through all the planes above the reach the objective. The scattering of these photons on the way to the objective will broaden P_{scatt} and will contribute to the overall PSF.

Detection function

Eventually the detection optics contribute to the PSF. This third contribution P_{det} is sample independent and for most cases smaller than the PSF broadening due to scattering. Besides the fundamental limitation of the resolution, the detection PSF can include other imperfections of the (lens) imaging system such as optical aberration.

Combined PSF

In the following all three separate contributions are condensed in one single PSF. Equation 3.4 will take the simple form

$$I_z = O_z * P_z + N_z, \qquad (3.5)$$

where I_z is the image recorded in the plane z, O_z is the distribution of fluorophore in the illuminated plane, P_z is the PSF, and N is the noise term.

P_{illum} as well as P_{scatt} will change for different z-planes and therefore the over all PSF P_z becomes z-dependent. Since biological samples are usually quite heterogeneous, the amount of scattering will vary depending on the position in the image.

Furthermore, the sample might not be flat and the distance the photons have to travel through tissue will depend on the position in the object/image. Therefore, the PSF will generally also vary for different positions within the xy-plane.

3.2 Deconvolution Algorithm

To reconstruct the original image or the distribution of fluorophores, a deconvolution of the image and the PSF has to be performed. Mathematically this is a well known inverse problem. Since the PSF and the object function are both unknown, this problem is also referred to as a blind deconvolution. Several different approaches haven been published to solve deconvolution problems in general [51–54] and blind deconvolution problems in particular [55,56]. The deconvolution problem is typically ill-conditioned and will not necessarily converge to one single solution. To improve the convergence and the quality of the reconstruction algorithm different priors and regularizers can be used. In this thesis a new idea is developed using neighboring SPIM planes as a prior for the reconstruction. Furthermore a regularizer is used to implement a simplistic model of scattering into the reconstruction.
The following sections will discuss how to solve the deconvoltuion problem computationally with the use of the image space reconstruction algorithm (ISRA) [53]. In the field of image reconstruction the ISRA is a commonly used reconstruction framework. The algorithm will be used to implement both the prior and the regularizer for the scattering correction into the reconstruction.

Most deconvolution algorithms assume a static and space invariant PSF. This approximation is valid, if the image formation is mostly affected by detection PSF. For lager samples scattering has a significant influence on the PSF. Since the scattering within the sample is most often inhomogenous, the PSF shows a spatial dependence. The deconvolution algorithm has to account for this spatial dependence. Solutions for similar problems have already been described in the field of image reconstruction, for example camera shake [57]. A method to account for the spatial dependence is the decomposition of the original image into smaller sub-images by the Gabor transform, which will be used in this thesis. However, for a better understanding of the general principle the sections will be split into two parts. First the simpler case of a spatially invariant PSF (space invariant in the xy-plane not in z) will be discussed. Later the method will be extended to the account for spatial dependence.

3.2.1 Spatially invariant algorithm

In the spatially invariant case each z-plane of the detected SPIM image is treated as a convolution between the real object and the PSF plus an additional noise-term (see equation 3.5). This noise term accounts for all the noise influences on the final image introduced by the imaging system. There is no trivial solution for O_z in

equation 3.5. However, if N is Gaussian noise, the original image can be estimated by minimizing the least square error E:

$$E_0 = \|I_z - P_z * O_z\|_2^2. \tag{3.6}$$

The least square error E_0 is the error of the approximated solution for O_z and P_z, i.e. the deviation from the original image I. However, it should be noted that the image noise is typically not Gaussian distributed but rather a mix of Gaussian and Poisson noise. Gaussian noise is mainly intoduced by the electronic sensor and electronic acquistion system, while the Poission or shot noise is introduced by the stastical characteristics of the photons, which hit the sensor.

For a large number of photons the Poisson noise approaches a Gaussian distribution. If the photon count is lower and the noise in the image shows a mix of Poisson and Gaussian noise, a variance-stabilizing transform can be used to transform the noise into a near Gaussian distribution with a constant variance [58]. Other possibilities to account for the Poisson characteristic of the noise is the use of different deconvolution methods, such as the Lucy-Richardson alogrithm. Nevertheless, the image space reconstruction algorithm which will be introduced below turned out to be stable also in the case of Poisson noise [59].

Equation 3.6 is typically ill conditioned, even if the PSF is known - which is not the case for the reconstruction described in this chapter. Here the only known variable is I and both P and O have to be reconstructed. Trying to minimize the least square error will not necessarily converge to a unique solution. To obtain a converging solution, further assumptions have to be made or more information has to be added to the problem. Multiview deconvolution algorithms of SPIM images, such as the one presented by Preibisch et al. [47], use the information provided by the multiple image stacks which are acquired from different angles in order for the algorithm to converge. If only a single image stack from one direction is known, which is the assumption for the algorithm introduced in the following, a different approach has to be chosen.

3.2.2 Coprimeness prior

To improve the convergence towards a unique solution, a prior which uses information from neighboring image planes is introduced in this thesis. The prior is based on the assumption that the same object is illuminated in both planes if the step size between the two consecutive z-planes is small enough. Only the PSF will (slightly) change for the neighboring image planes. This assumption is, of course, only true if the selected step size is smaller than the observed structures. At the edge of a structure only one neighboring plane will show the same object and the prior will be less beneficial for improving the convergence. The described approach is depicted in Fig. 3.5a. When reconstructing a single plane I_{z_i} from the image stack (depicted in red in Fig. 3.5) the neighboring plans above and below: $I_{z_{i-1}}$ and $I_{z_{i+1}}$ are assumed to show the same object O_z. For each of these images the convolution

is given by

$$I_{z_i} = O_z * P_{z_i} + N_{z_i}. \tag{3.7}$$

Under ideal conditions of no noise, the same support for O_z and P_{z_i} (no support constraint), and the assumption of multiple observations of P_{z_i} (i=1,2,3) of the same object the coprimeness equation can be used to determine the PSF:

$$P_{z_j} * I_{z_i} - P_{z_i} * I_{z_j} = 0 \quad \forall \, i \neq j \tag{3.8}$$

This equation can be derived from the commutativity of the convolution operator $*$ and the presence of the common factor in equation 3.7. For further details see [60]. Since no ideal conditions are given and noise is present in the image, there will be no exact solution to equation 3.8. Instead the equation becomes an optimization problem:

$$E_{coprime} = \sum_{(i \neq j)} \| P_{z_j} * I_{z_i} - P_{z_i} * I_{z_j} \|_2^2. \tag{3.9}$$

The effectiveness of algorithms based on the coprimeness equation as a prior have already been shown by multiple groups [56, 61, 62]. The prior is normally either used with different views of the same object or in time series of the same view with slightly varying PSF. However the coprimeness equation itself will typically not converge to a single solution [56], but since the equation is independent of the solution of O, it can be used as an additional regularization for the error function E_0:

$$E_{tot} = E_0 + E_{coprime} = \sum_i \| I_{z_i} - P_{z_i} * O_z \|_2^2 + \lambda \sum_{(i \neq j)} \| P_{z_j} * I_{z_i} - P_{z_i} * I_{z_j} \|_2^2. \tag{3.10}$$

To find a solution for P and O the cost function E_{tot} needs to be minimized. The convergence of the minimization can be improved to be faster and more stable if additional assumptions due to the to the physical properties of the imaging system are made. The properties of the imaging include that the PSF cannot be negative: $P_{z_i} \geq 0$. Furthermore, all three PSF $P_{z_{i=1,2,3}}$ can be normalized to the same value by the sum constraint:

$$\sum_{x,y} P_{z_i}(x,y) = 1 \tag{3.11}$$

Strictly speaking this is only valid if absorption in the sample can be neglected. Since the step size between the z-planes is small and the algorithm is only considering adjacent z-planes, this is a reasonable assumption. The positivity constraint holds as well for the object $O_z \geq 0$. Furthermore, the support Ω of the PSF should be smaller than I and O and therefore it can be assumed to be included in a predefined

set: $\Omega \subset \Omega_0$. These constraints together with the assumptions that the object in the z plane above and below is the same while the PSF P_{z_i} (i=1,2,3) changes lead to the following minimization problem:

$$\min_{P_i \geq 0, \sum P_i = 1, P_{\Omega_0^\perp} = 0, O \geq 0} \sum_i \|I_{z_i} - P_{z_i} * O_z\|_2^2 \sum_{(i \neq j)} \|P_{z_j} * I_{z_i} - P_{z_i} * I_{z_j}\|_2^2 \tag{3.12}$$

The last term, the comprimeness regularization mentioned above, helps to stabilize the deconvolution problem and can even lead to a unique solution [61]. It should be noted that although the term E_0 is convex (but not necessarily strictly convex) for a single variable (i.e. the Image O_z or the PSF P_{z_i}), the function is not convex for both variables simulaniously [63].

To achieve convergence of the cost function, an alternating optimization scheme is used. Since both the PSF (P_{z_i}) and the object (O_z) are convex, the nonlinear Gauss Seidel algorithm can be used to ensure convergence [64]. In this scheme P_{z_i} and O_z are optimized one after another independently while the other parameter is fixed. Thus the over all optimization algorithm iterates between P_{z_i} and O_z:

$$P_{k+1} = \arg\min_P E_{tot}(P, O_k) \tag{3.13}$$

$$O_{k+1} = \arg\min_O E_{tot}(P_{k+1}, O) \tag{3.14}$$

3.2.3 Image Space Reconstruction Algorithm (ISRA)

The optimization of the PSF (P) and the object (O) are both inverse problems with no direct solutions. To reconstruct O for a fixed P an iterative scheme can be used. There is a large variety of image reconstruction algorithms, which use such an iterative scheme. Each of these algorithms starts with a "guessed" object, calculates the convolution between O and P and then compares the result to the recorded image (I). In a second step the object is updated based on the difference between the calculated image and the recorded image. Examples of such algorithms are the Richardson–Lucy deconvolution [59, 65], the maximum likelihood expectation maximization (ML-EM) [54] algorithm, and the Image Space Reconstruction Algorithm (ISRA) [53, 66]. One difference between these algorithms is how the error of the current iteration step is weighted and how it is used to update the assumed object for the next iteration step. In this work the ISRA algorithm is used, because the algorithm can easily be adapted to include different priors and regularizers due to the multiplicative update rules of the algorithm [59, 67]. One of these regularizers will be used as a simple model for scattering in the sample (see section 3.2.5).

The iterative Image Space Restoration Algorithm was first introduced by Daube-Witherspoon and Muehllehner in 1986 for image reconstruction from positron emission computed tomography (PET) data and is based on the maximum likelihood (ML) algorithm [53]. For an imaging problem such as in equation 3.5 and eqaution 3.6 with the resulting optimization problem:
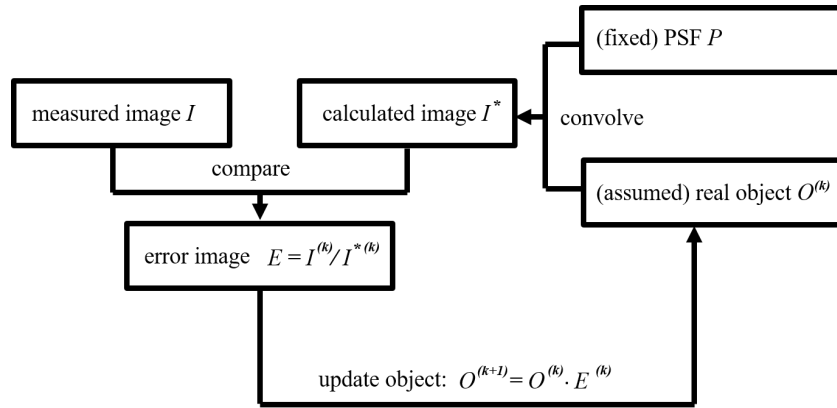
Figure 3.4: Scheme of ISRA for a fixed PSF The measured image (I) is compared to the calculated image $I^{*(k)} = O^{(k)} * P$. The error image $E^{(k)}$ is used to update the guess for the object $O^{(k+1)} = O^{(k)} \cdot E^{(k)}$. At this point the iteration starts into another round. The new object $O^{(k+1)}$ is again convoluted with the PSF and the resulting image $I^{*(k+1)}$ is compared to the measured image.

$$\min \sum_i \|I_i - P_i * O\|_2^2 \qquad \text{,with} \tag{3.15}$$

$$I_i = O * P_i. \tag{3.16}$$

The basic iteration scheme can be seen in Fig. 3.4. First the algorithm takes an initial guess for $O^{(k=0)}$ (this inital guess could for example be the recorded image). Then the (in this example) fixed P is convoluted with $O^{(k=0)}$. The result $I^{*(k)}$ is compared to I. By multiplying the current guess of $O^{(k)}$ with the error image $E = I/I^{*(k)}$ a better estimation for $O^{(k+1)}$ can be found:

$$O^{(k+1)} = O^{(k)} \cdot E^{(k)}. \tag{3.17}$$

This iteration can either be repeated a fixed number of iteration circles or until E is small enough. Analog to this scheme the PSF can be calculated when fixing O and iterating $P^{(k)}$:

$$P^{(k+1)} = P^{(k)} \cdot E^{(k)}. \tag{3.18}$$

This equation holds for the basic deconvolution of a miniaturization problem of the form $\min \sum_i \|I - P * O\|_2^2$. In the following the update rules for the PSF and the object will be derived for the minimization problem stated in equation 3.12 starting with the optimization for $P_{z_i}^{(k)}$ for a fixed object function O_z. The equation for this optimization is given by:

$$\min_{P_i \geq 0, \sum P_i = 1, P_{\Omega_0^\perp} = 0} \sum_i \|I_{z_i} - P_{z_i} * O_z\|_2^2 + \sum_{(i \neq j)} \|P_{z_j} * I_{z_i} - P_{z_i} * I_{z_j}\|_2^2. \qquad (3.19)$$

Even if O_z is fixed the equation is still a multi-variable problem with convex sub-problems for each of the three P_{z_i} of the three adjacent planes. Again the nonlinear Gauss Seidel algorithm can be applied to the optimization problem. For the optimization of a single P_{z_m} the Gauss Seidel algorithm yields the following quadratic problem:

$$\min_{P_m \geq 0, \sum P_m = 1, P_{\Omega_0^\perp} = 0} \|I_{z_m} - P_{z_m} * O_z\|_2^2 \sum_{(m \neq j)} \|P_{z_j} * I_{z_m} - P_{z_m} * I_{z_j}\|_2^2 \qquad (3.20)$$

$$= \min_{P_m \geq 0, \sum P_m = 1, P_{\Omega_0^\perp} = 0} \langle O_z * P_{z_m} | O_z * P_{z_m} \rangle \sum_{(m \neq j)} \langle I_{z_j} * P_{z_m} | I_{z_j} * P_{z_m} \rangle$$

$$-2 \left(\langle I_{z_m} | O_z * P_{z_m} \rangle \sum_{(m \neq j)} \langle P_{z_j} * I_{z_m} | I_{z_j} * P_{z_m} \rangle \right) \qquad (3.21)$$

Introducing the notation of the convex set $C = \{x | x \geq 0\} \cap \{x | x_{\Omega_0^\perp} = 0\} \cap \{x | \sum x = 1\}$, the equation simplifies to:

$$\min_{P \in C} \langle O_z * P_{z_m} | O_z * P_{z_m} \rangle \sum_{(m \neq j)} \langle I_{z_j} * P_{z_m} | I_{z_j} * P_{z_m} \rangle$$

$$-2 \left(\langle I_{z_m} | O_z * P_{z_m} \rangle \sum_{(m \neq j)} \langle P_{z_j} * I_{z_m} | I_{z_j} * P_{z_m} \rangle \right) \qquad (3.22)$$

Following the basic scheme in equation 3.18 but inserting the optimization problem in equation 3.22 yields the following equation:

$$P_{z_m}^{(k+1)} = P_{z_m}^{(k)} \frac{O_z * O_z^* * I_{z_m} + \sum_{(j \neq m)} I_{z_j} * I_{z_j}^* * P_{z_j}^{(k)} * I_{z_m}}{\left(O_z * O_z^* + \sum_{(j \neq m)} I_{z_j} * I_{z_j}^* \right) * P_{z_m}^{(k)}} \qquad (3.23)$$

$$P_{z_m}^{(k+1)} = P_{z_m}^{(k)} / \sum P_{z_m}^{(} k) \qquad (3.24)$$

The whole iteration process follows the scheme in Fig 3.5b.
After the first iteration of the PSF is done, all three P_{z_i} get fixed and the object is iteratively reconstructed. Since only one object is assumed for all three images the minimization reduces to the more simple from:

$$\min_{O \geq 0} \sum_i \|I_{z_i} - P_{z_i} * O_z\|_2^2 \qquad (3.25)$$
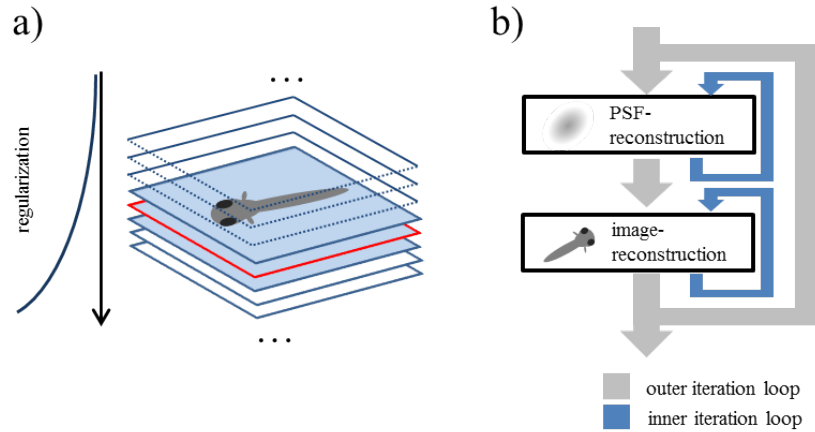
Figure 3.5: Prior and Iteration scheme a) illustration of the comprimeness prior with the quadratically increasing regularization. The prior assumes neighboring slices show the same object for sufficient sample step sizes between z-plane. The two blue colored planes are used to reconstruct the red framed plane). b) the iteration scheme of the used algorithm. PSF and object are reconstructed iteratively one after each other with the ISRA algorithm while keeping the other one of them fixed (inner loop). After a new estimation for PSF and object is found the whole iteration starts over again (outer loop)

Similar to the problem of a single PSF update discussed above, this is a constraint quadratic problem. The update rule can easily be derived from equation 3.17 and takes the following form:

$$O_z^{(k+1)} = O_z^{(k)} \frac{I_{z_i}}{O_z * O_z^* * P_{z_m}^{(k)}} \tag{3.26}$$

The Gauss-Seidel algorithm, which was used to derive the optimization formula, requires each sub-problem to be strictly convex (i.e. have a unique solution). This is, however, not the case for either the object nor the PSF optimization. Although both sub-problems are convex, strict convexity cannot be guarantied. One way to achieve strict convexity in all sub-problems is the proximal minimization method, which will shortly be discussed in the following.

3.2.4 Proximal minimization method

For a general optimization problem of the convex function $F(x)$:

$$\min_{x \in X} F(x)$$

the proximal minimization operator [68] is defined as:

$$\min_{x \in X, y \in \mathbb{R}^n} F(x) + \frac{1}{2\lambda} \|x - y\|_2^2, \tag{3.27}$$

with the scaling or regularization parameter λ. Application of the nonlinear Gauss-Seidel algorithm yields the following equation:

$$x^{(k+1)} = \arg\min_{x \in X} F(x) + \frac{1}{2\lambda} \|x - y^{(k)}\|_2^2 \tag{3.28}$$

$$y^{(k+1)} = x^{(k+1)} \tag{3.29}$$

or equivalently

$$x^{(k+1)} = \arg\min_{x \in X} F(x) + \frac{1}{2\lambda} \|x - x^{(k)}\|_2^2 \tag{3.30}$$

Now the problem is strictly convex and should result in a unique solution. Because of the multiplicative update rules of the ISRA the regularization can easily be added. Together with the proximal minimization regularization the algorithm will converge and can be used to reconstruct both O and P.

3.2.5 Scattering model and Tikhonov regularization

In this section the second novelty besides the coprimness prior, which uses information of neighboring planes, is introduced into the algorithm. To further improve the reconstruction, knowledge about the scattering in the sample will be taken into account.

When light enters a biological tissue, the photons will interact with the different cellular structures on there way through the sample. Some of the photons will be absorbed by the tissue but a much more frequent interaction between the tissue and the photons is elastic scattering. In the process of scattering the photons will be absorbed a re-emitted by the molecules or cellular structures without the loss of energy but under a certain angular distribution. In case most of the photons are emitted under small angels in the forward direction, the scattering process is referred to as forward peaked scattering. With increasing imaging depth the deviation of the photons form the original beam path increases and additional scattering events take place. Therefore the images will suffer from increased scattering blur for image planes from deeper inside the sample.

The idea of the adaptive regularizier, which will by introduced in this section, is to compensate for the increased scattering by adjusting the regularization along with the imaging depth. An approximation for forward peaked light scattering in

tissue is found in [69, 70] and is given by the the Fokker–Planck and Leakeas–Larsen equations or can be approximated with a Monte Carlo simulation. However, in this work an even more simplified model will be used. With increasing depth the size of the PSF is assumed to grow quadratically. To implement this simple model, the Tikhonov regularization [71, 72] was chosen. Similar to the proximal minimization method, the Tikhonov regularization is often used to achieve strict convexity of a minimization problem. The implementation is simple since only two regularization terms are added to the minimization:

$$\min_{P_i \in C, O \geq 0} \sum_i \|I_{z_i} - P_{z_i} * O_z\|_2^2 + \sum_{(i \neq j)} \|P_{z_j} * I_{z_i} - P_{z_i} * I_{z_j}\|_2^2 + \alpha \|O_z\|_2^2 + \beta \sum_i \|P_{z_i}\|_2^2,$$

(3.31)

with α and β being two regularization parameter. The introduced terms achieve strict convexity. However the regularization has a non-trivial interaction with the sum constraint $\sum_i P_{z_i} = 1$. This can be explained by the sparseness measure [73]. The sparseness measure can be defined by the relationship between the L_1 norm and the L_2 norm:

$$\text{sparseness}(\boldsymbol{x}) = \frac{\sqrt{n} - \frac{\|x\|_1}{\|x\|_2}}{\sqrt{n} - 1} = \frac{\sqrt{n} - \frac{\sum_i |x_i|}{\sqrt{\sum_i x_i}}}{\sqrt{n} - 1},$$

(3.32)

where n is the dimensionality of the vector $\boldsymbol{x}$. $\|x\|_1 = \sum_i |x_i|$ and $\|x\|_2 = \sqrt{\sum_i x_i^2}$ are the L_1 and L_2 norm, respectively. The sparseness measure lies between 0 and 1, with 1 corresponding to a delta peak and 0 to a constant function $\boldsymbol{x}$ (i.e higher values describing sparser signals). With the sum constraint being defined as $\sum_i x_i = 1$, the spareness changes to:

$$\text{spareness}(\boldsymbol{x}) = \frac{\sqrt{n} - \frac{\|x\|_1}{\|x\|_2}}{\sqrt{n} - 1} \overset{\text{constraint}}{=} \frac{\sqrt{n} - \frac{1}{\|x\|_2}}{\sqrt{n} - 1}$$

(3.33)

Since the Tikhonov regularization penalizes the L_2 norm $\|x\|_2$, the regularization will result in a decrease of the sparseness measure above. This will push the solution of the minimization towards a constant and increase the support of the function. Therefore the PSF will be broadened by the Tikhonov regularization.

This effect of a broadened PSF with an increased regularization is used to implement the scattering model. By increasing the regularization parameter β with depth, the solution is pushed towards a larger PSF, which will compensate for the effect of increased scattering for photons from these deeper planes. In the assumed scattering model the PSF will increase quadratically with depth. For more adavanced scattering models the parameter can be adapted to change accordingly. However, the quadratic increase was empirically found to be a good approximation, as shown by the results

in section 3.4.

3.2.6 Spatially varying algorithm and the Gabor transform

In general, the scattering will not only vary with depth but will also depend on the xy-position within the sample. This is due to varying degrees of scattering within the sample for different organs and structures. Furthermore, the sample might not be flat and the distance the photons have to travel through tissue will depend on the position in the object/image. Hence equation 3.5 generalizes to:

$$I_z(x,y) = O_z(x,y) * P_z(x,y) + N \tag{3.34}$$

So far a single PSF was used to deconvolve the whole xy-plane of the image. A spatial dependence requires the image to be deconvolved with different PSFs for different regions of the image. This can be achieved by splitting the image into smaller patches and do independent deconvolution for each sub-image. A similar approach has been successfully used to remove motion artifacts in photography [57, 74].
One way of splitting the reconstruction into smaller patches and therefore account for the spatial dependency of the PSF is given by the Gabor transform. It is named after Dennis Gabor and can be seen as a window based short time Fourier transform. Although the Gabor transform was originally introduced in the context of quantum mechanics in 1946 [75], it has proven to be valuable in a variety of image and signal processing applications [76, 77]. The implementation of the Gabor transform will be achieved by comparing the original signal with a translation of a window function g through an inner product (i.e. a generalized convolution operator $*$)). Since the window function is localized in space, the inner product will only contain a (localized) fraction of the original signal [77]. As mentioned earlier, the Gabor transform can be seen as a special case of the short time Fourier transform (STFT), which is defined as:

$$[\text{STFT}(f)](x,\omega) = \int\limits_{-\infty}^{\infty} f(y)w(y-x)e^{-2\pi i\omega y}\,\mathrm{d}y \tag{3.35}$$

Here $f(x)$ is the original signal and $w(x)$ is a window function. The (discrete) Gabor transform can be seen as a discrete sampling form of the STFT [76, 78].
Similarly to the STFT a window g_m can be defined. In the standard definition of the Gabor transform a single window function g is chosen and then translated (and eventually modulated) with a simple translation operator: $g_m = T_m g$, with $(T_m f)(x) = f(x-m)$. However, more generally the window function g_m does not necessarily have be be the same size and can be seen as a set of window functions [77]. Based on the chosen window, the Gabor coefficients of a function f are defined as the inner product of the window g_m and the function f:

$$V_m(f) = \langle f, g_m \rangle \tag{3.36}$$

with the inner product defined similarly to the convolution operator.

To invert the Gabor transform and reconvert the Gabor coefficients to the original function f, a dual window γ_m is necessary. With this dual window γ_m, a reconstruction operator R can be defined:

$$Rf = \sum_m V_m(f)\gamma_m. \tag{3.37}$$

A major aspect of the Gabor transform is finding suitable windows g and γ that fulfill the equation $Rf = f$ [77]. The reconstruction or inversion is perfect for all pairs of g and γ fulfilling equations 3.36 and 3.37 above. However, this is only true if the function f is not altered after the decomposition. When filtering or reconstruction is applied on f in the Fourier space (as it is the case for the presented algorithm) the inversion might produce unwanted artifacts. Therefore it is desirable to choose a reasonably smooth window function.

Implementation of the Gabor transform

One possibility of implementing the Gabor transform and its inversion is using a cyclic partition of the unity as shown by [76]

$$\sum_m g_m = 1, \tag{3.38}$$

where g is again the window function (or support) of the Gabor transform. This partition of the unity can be used to realize the Gabor transform. The resulting Gabor coefficients can be defined similar to equation 3.36:

$$V_m(f) = \mathcal{F}(fg_m^p)) \tag{3.39}$$

The inverse transform is given by:

$$Rf = \sum_m \mathcal{F}^{-1}(V_m) \cdot g_m^{(p-1)} \tag{3.40}$$

$$= \sum_m fg_m^p g_m^{(p-1)} = f \tag{3.41}$$

As mentioned before, the window function should be smooth and symmetrical to avoid artifacts. To ensure a good localization of the transformed signal the window function should furthermore have a limited support (i.e. drop the zero at some

point). The **sine**^{2} function on the interval $[0,\pi]$ fulfills these requirements. The **sine**^{2} window function can easily be used to match the criteria in equation 3.38 by translating the window about half of its width. An example for the resulting set of windows can be seen in figure 3.6.
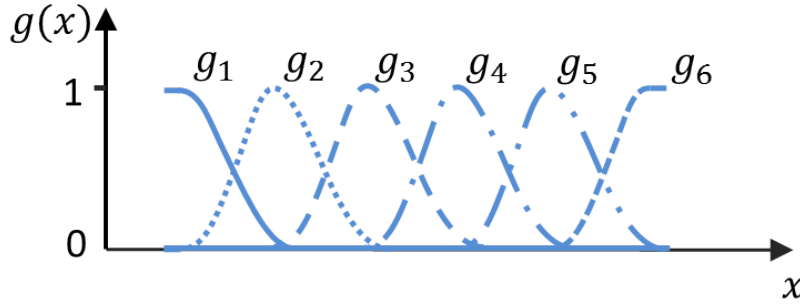
Figure 3.6: Gabor windows A collection of windows covering the signal space. The **sine**^{2} windows overlap by 50% and add up to one.

An exception to the periodical translation of the window by half of its width (Figure 3.6 g_2-g_5) are the border windows (g_1,g_6), which consist of a cropped window. In case a fixed window size is chosen and the function f is not a multiple of this window, the "border"-windows can be used to the match the size.

Although the Gabor transform is discussed for the 1D case in this section, the extension into 2D is straight forward. In the case of the spatially variant blind deconvolution algorithm, the function f is a 2D image from the SPIM image stack. The window function g is defined as a 2D window function $g = \sin^2(x) \cdot \sin^2(y)$ with $x,y \in [0,\pi]$. The size of the windows was chosen to be large enough to most closely satisfy the $\sum P_i = 1$ constraint. The calculation of the object and the PSF is done for each of these windows independently and in the end the object is put back together with the inverse transform. The whole reconstruction is basically split into smaller (overlapping) z-stacks (smaller in the xy-plane, not in z-direction). Since the sample is not necessarily flat, the z-position of the image plane containing the sample surface might vary from window to window. Hence the depth regularization by the adapted Tikhonov parameter was done for each window independently. By comparing the intensity of the image in each window to a threshold, an estimate for the surface of the sample was found. From there the depth was measured and the Tikhonov regularization was increased quadratically.

3.3 Simulation

To validate the algorithm and to visualize its basic functioning, the algorithm was first applied to a set of artificial data. For this propose an artificial dataset was created. The simulated 3D volume was filled with multiple overlapping cylinders all facing the z-direction. Inside the cylinders the simulated dataset was given the value 1 and 0 everywhere else. The cylinders span over all planes. This original volume (analog to the "real object" in the section above) was convolved with a PSF P_{sim}. Since the algorithm is based on the assumption that with increasing depth

(i.e. z-position) the PSF increases in size due to scattering, the simulated PSF has to reflect this behavior. A Gaussian PSF was chosen and altered for each z-plane in the volume by quadratically increasing the width σ^2 of the PSF. Furthermore, the PSF was designed to be asymmetric in one direction resulting in an ellipsoidal shape:

$$P_{sim}(z) = A \exp\left(-\frac{(a(x-x_0)^2 - 2b(x-x_0)(y-y_0) + c(y-y_0)^2)}{2\sigma^2(z)}\right). \quad (3.42)$$

An example of the generated PSF can be found in Figure 3.7b, where the PSF from one z-plane (z=18) is shown.
The ellipsoidal shape of the PSF allows for a more general evaluation of the reconstruction algorithm. In theory the algorithm should be capable of retrieving any PSF shape. A stretched or ellipsoidal shape, as used in this simulation, is typically related to a motion blur of the image [57]. Although this type of image deformation can often be found in photography they can also appear in SPIM images.

Each plane of the original volume is convolved with the respective PSF. In the second step the convolved dataset is reconstructed by the introduced blind deconvolution algorithm. In Figure 3.7 the results of the reconstruction can be found. Figure 3.7a shows the mean square error (MSE) of the convolved dataset (drawn in red) and the reconstructed dataset (drawn in green) compared to the original volume as a function of depth (z-position). It can be observed that the deviation from the original increases much slower for in the reconstructed dataset for deeper z-planes. Three different planes ($z = 6, z = 18, z = 28$) are marked in the graph and a cross section from these planes is shown in Figure 3.7d-f. The region where the cross section is taken from is identical for all three plots. The plotted region is marked in Figure 3.7g, where the corresponding z-plane for the cut through in Figure 3.7d ($z = 6$) is shown. All three panels 3.7g-i show the reconstructed z-planes from the same depths as the cross sections above ($z = 6, z = 18, z = 28$).

Although in this case no spatially varying PSF was used to create the artificial dataset, the finalized space-variant blind deconvolution algorithm was used. By keeping the space-variant part the influence of the chosen Gabor window and possible artifacts can be determined. 25 windows were chosen to cover the whole plane. This is the same amount of windows, which was used for most of the reconstructions of experimental data. The only parameter which has to be adapted is the factor β in front of the quadratically increasing Tikhonov regularization parameter. This parameter depends primarily on the physical distance between two neighboring planes (i.e. the step size in z-direction).

Whereas at the beginning both the convolved dataset and the reconstructed dataset yield the same results, the edge steepness of the reconstructed data is decreasing much slower than the edge steepness of the convolved data. This can be seen in Figure 3.7d-f where the convolved data (colored in red) is compared to the
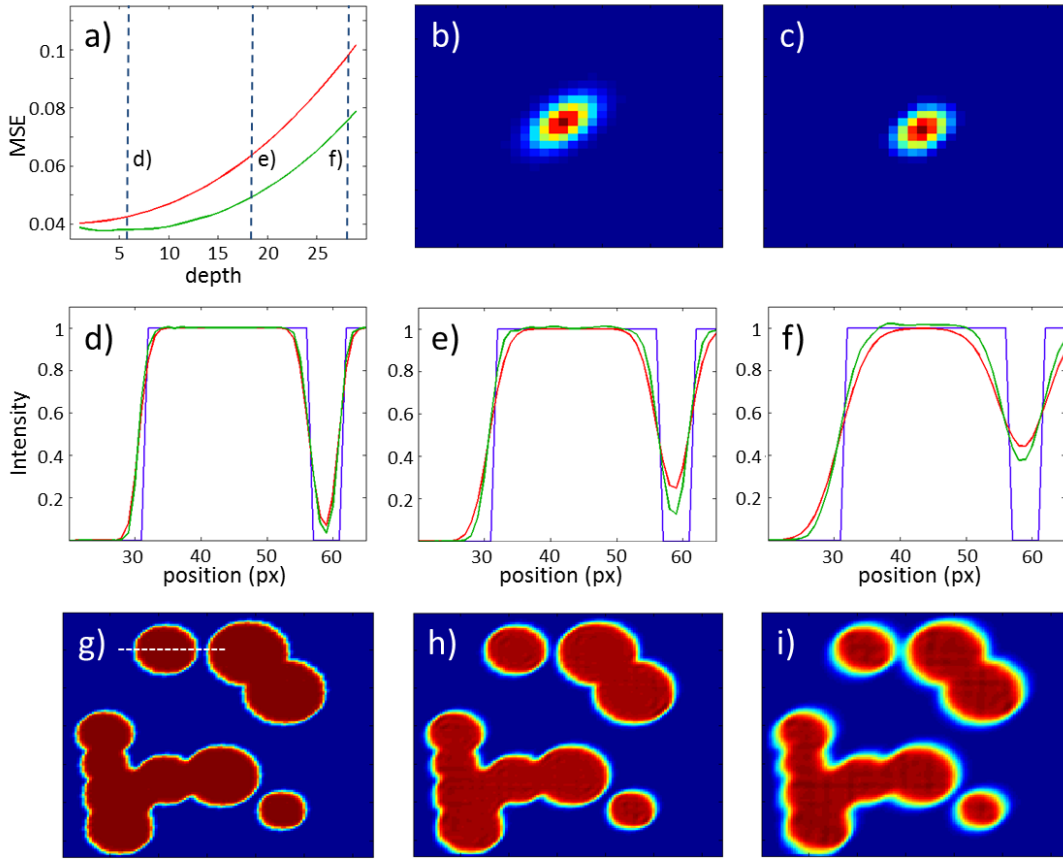
Figure 3.7: Simulation a) Mean square error of the artificial dataset (colored in red) and its reconstruction (colored in green) as a function of depth (z-position). The three dashed lines indicate the depth at which the images as well as the cross sections were taken. b) PSF which is used to generate the artificial dataset for the depth z=18; c) Reconstructed PSF from the same depth z=18; d-f) cross sections through different z-planes: d) z=6, e) z=18, f) z=28. In blue the original object is plotted, in red the convolved object, or the simulated dataset is shown and in green the reconstructed dataset is depicted. g-i) z-planes corresponding to the depth of the cross sections above (image width 256 px): g) z=6, h) z=18, i) z=28. The white dotted line in g) indicates the position the cross sections were taken from.

reconstructed data (colored in green) as well as in Figure 3.7a where the MSE of the reconstructed data (also colored in green) starts to rise later than the MSE of the convolved data (colored in red).

To further validate the function of the algorithm, the calculated PSF is compared to the initial PSF. The initial or original PSF is known, since it was used to produce the artificial dataset. One of the 25 PSFs of the different windows from plane $z = 18$ calculated by the algorithm can be seen in Figure 3.7c, next to the original PSF in Figure 3.7b. Although the original PSF has a slightly larger support and shows higher intensities in the outer regions both PSF coincide well. The PSFs have the

same directionality and about the same width.

In Figure 3.7h and 3.7i small artifacts due to the reconstruction can be observed. Small window artifacts can be observed at the edges of the window frames. These window artifacts get slightly stronger for reconstructions with larger PSFs. As mentioned in the previous section 3.2.6, the Gabor transform and inversion is error-free if the original image is unaltered. The more the reconstruction alters the original image, the more the Gabor inversion is visible in the reconstruction of the simulated data. Furthermore, circular artifacts around the edge of the cylinder are visible. The artifacts have an oscillating appearance around steep edges in the image and occur when the PSF is overestimated by the reconstruction algorithm. In contrast to the window artifacts, they can also be observed in experimental data, especially when the factor in front of the quadratically increasing Tikhononv regularization is not properly adapted to the step size of the recorded z-stack. Since the artifacts are related to PSF size and therefore to overregularization of the PSF, they are closely related to the introduced reconstruction algorithm and its advantage over regular deconvolution algorithms. An overestimation of the Tikhonov regularization parameter will generally lead to an overestimation of the PSF size and cause oscillating artifacts. To visualize this effect, the regularization was kept constant over all z-planes. Figure 3.8 shows a cut through the simulated volume in plane $z = 6$ with the same level of regularization applied to the image in Figure 3.7f and 3.7e ($z = 28$). In blue the original object is plotted, in green the reconstructed dataset is depicted and in red the reconstructed dataset with a constant (oversized) regularization is shown. The overestimated PSF causes large oscillations around the edge of the cylinder.
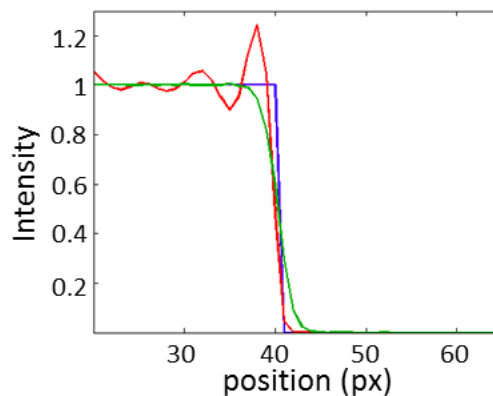
Figure 3.8: Simulation of reconstruction artifacts Cross sections through z-plane z=6 of the artificial dataset. In blue the original object is plotted, in green the reconstructed dataset is depicted and in red the reconstructed dataset with a constant (oversized) regularization is shown.

The results from the simulated dataset demonstrate the function of the algorithm. It is shown that the algorithm is able to improve the image quality for a volume with an increasing simulated scattering. Since constant cylinders over all z-planes

were assumed in the simulation, it is not shown how the approximation of a constant object within the algorithm is affecting its function. To validate this approximation as well as to test the algorithm under real conditions, a real dataset is used in the following section.
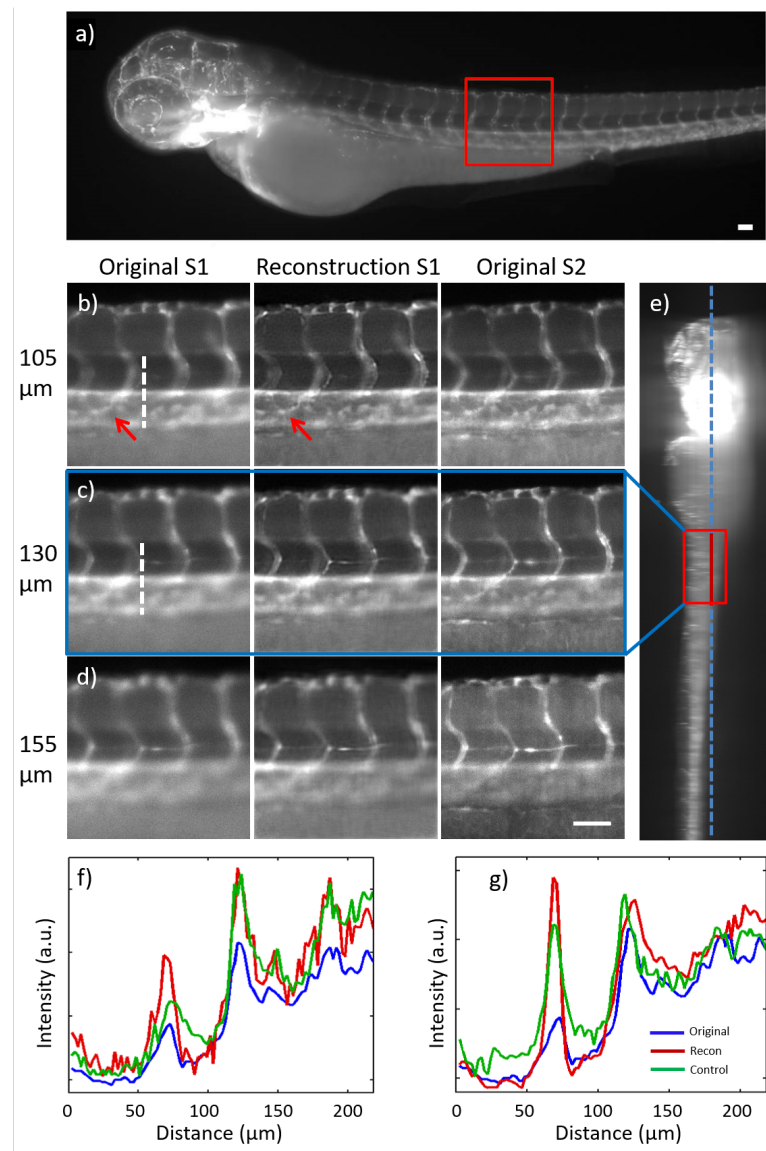
3.4 Experimental Results

In this section the effect and the performance of the algorithm on a real dataset is examined. As a sample, a transgenic zebrafish embryo, a common model organism for biological research, is used. The 3 day old zebrasfish embryo of the genetically modified line Fli1A had its vasculature labeled with EGFP (enhanced Green Fluorescent Protein). Furthermore, results from the article [79] will be presented. In this paper the algorithm was applied on an adult zebrafish.

First, the results of the 3 day old fish larvae will be discussed[1]. The fish was imaged sideways with a step size of $5\,\mu m$ between adjacent z-planes. A maximum intensity projection (MIP) of the fish can be found in Figure 3.9a. Two complete 3D image stacks of the zebrafish embryo were acquired, and the sample was rotated by 180° between the image stacks. While reconstruction was only performed on the first image stack (S1), the second image stack (S2) was used as a control image. Since the imaging was done from two opposed sites, structures which appear deep and scattered in S1 are better visible in S2. The revered imaging depth of the dataset S2 is used to validate the reconstruction results from S1. To be able to use the second dataset (S2) for validation, a region from the tail of the fish with a width of about $175\,\mu m$ was selected. Thicker regions like the head would not be suitable, since the effectively usable overlap where both datasets can be used is too small or nonexistent. The chosen region is marked red in Figures 3.9a and 3.9e. Figure 3.9b, 3.9c and 3.9d show image slices from three different depths: $105\,\mu m$, $130\,\mu m$, and $155\,\mu m$, respectively. In Figure 3.9e the MIP of S1 is shown, this time from the top to the bottom of the fish (the dataset is rotated by 90° with regard to the image in panel 3.9a. The left side is the front, facing the objective; the right side is the back of the fish. The area, which is depicted in Figure 3.9b-c is again marked with a red box. The blue dashed line indicates one z-plane at $130\,\mu m$ depth, measured from the front of the fish. For this sample, the depicted depths are just in the range where scattering starts to drastically reduce the image quality. In the left column the original slice from dataset S1 is presented, the column in the middle shows the same slice after processing with the introduced algorithm, and the column to the right shows the corresponding slice from dataset S2.

The shown section was reconstructed using 25 windows. The red arrows indicate regions where the reconstructed dataset shows a clear improvement in image quality compared to the original dataset S1. The structures which can be seen at a depth of $105\,\mu m$ agree well with the structures in the second dataset S2. The effect is

---

1 The following results and discussions are already partly published [21]

Figure 3.9: Experimental Results Zebrafish Larvae a) MIP of the used dataset (S1). The image shows a zebrafish from the genetic line Fli1A 3 days past fertilization. The orange-colored box indicated the region which was used to demonstrate the reconstruction algorithm. b),c) and d) show the same region at different depth (105 μm, 130 μm, 155 μm). The column on the left shows the original dataset (S1), the column in the middle shows the reconstruction of the dataset to the left and the column on the right side shows a second dataset (S2), which was recorded from the opposite side of the fish to validate the reconstruction results. c) MIP of S1 this time from the top to the bottom of the fish. The left side of the fish is considered to be the front. The depth is therefore measured from left to right. The orange box again marks the region of interest. The blue dashed line indicates the z-plane shown in the middle line in b). g) and h) show a cut through the slices in a) and b). In blue the original dataset S1 is plotted, in red our reconstruction and in green the control dataset S2. Scale bar indicates 100 μm

still visible at a depth of 130 μm. The good agreement with the control dataset S2 can also be seen in Figure 3.9f and 3.9g, where line profiles through the slices at 105 μm (3.9g) and 130 μm depth (3.9h) are plotted. In blue the original dataset S1 is plotted, in red our reconstruction and in green the control dataset S2. The position of the chosen cut is indicated by a white dotted line in Figure 3.9b and 3.9c. Deeper inside the sample the ability of the algorithm to correct the image diminishes. At a depth of 155 μm the reconstruction algorithm is not able to reveal detailed structures anymore and the image quality is not significantly improved compared to the original dataset.
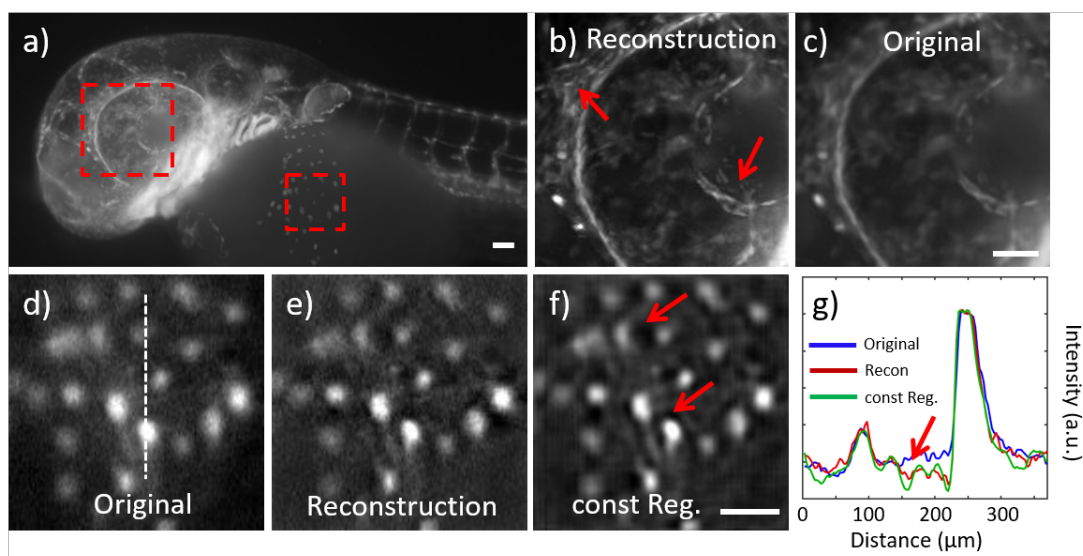
Figure 3.10: Artifacts Zebrafish Larvae a) MIP of the original dataset. The red-colored boxes indicate the two region of interest. The left region can be seen in b) and c), the right box marks a region of the yolk sac, which can be seen in d)-f). In b) the MIP of the reconstructed image stack can be seen, in c) the MIP of the original image stack. The red arrows indicate areas where the improvement can clearly be seen. d) shows a slice form the original dataset at a depth of 15 μm,e) shows the reconstruction of the same region with the introduced algorithm. In f) the adaptive regularization is switched of and a constant regularization factor is used. g) shows a cut through the plane, which is depicted in d)-f). The white dotted line in d) indicates the position of the cut through. Oscillations caused by over-regularization are marked with a red arrow. Scale bar indicates 100 μm

The adaptive regularization prevents over-regularization on image planes closer to the surface. Images form all planes benefit from the used prior, since the algorithm can correct for small motion artifacts which alter the PSF shape of neighboring planes. To point out this advantage the dataset of another 3 day old zebrafish embryo of the type Fli1A is shown in Figure 3.10a. This Figure shows the MIP of the head and the upper body. In red two regions of interest are marked.

The left box marks a region of interest which is covering part of the head and the eye of the zebrafish. Figure 3.10b shows a MIP of the original image stack. A MIP

of the reconstructed image stack is depicted in Figure 3.10c. The overall thickness of the head is around 320 μm. The blur due to scattering and other effects is clearly reduced in the reconstructed image and virtually no artifacts are seen. Small details which are not or only partly visible in the original MIP are clearly visible in the reconstructed MIP (see details marked by the two red arrows).

The second red box which is drawn in Figure 3.10a marks a part of the yolk sac in the belly. On the outer skin of this yolk sac some fluorescent structures can be seen. These structures are close to the surface and not expected to be significantly influenced by scattering. Therefore, it can be assumed that the original image 3.10d is close to the ground truth. Figure 3.10d shows an original slice of the belly in approximately 15 μm depth. Figure 3.10e shows the same slice reconstructed with our algorithm. The image blur is reduced and no severe artifacts can be observed. On the contrary, Figure 3.10f shows what happens if no adaptive regularization is used. The same algorithm is applied for the reconstruction, but the regularization is kept constant at a level, which is optimized for a depth of 180 μm. The resulting overestimation of the PSF size leads to artifacts (see red arrows).

As already shown in section 3.3 in Figure 3.8, an over-regularization of the PSF can lead to the formation of oscillations around the edge of plateaus or structures of high intensity. Similar artifacts are also visible in Figure 3.10f. The oscillations in this example are rather prominent and form "shadows" around the bright structures in the yolk sac (see red arrows). In Figure 3.10g a cut through the image slice is plotted. The region which is chosen for the plotted profile is indicated in Figure 3.10c by a white dashed line. In the plot the original dataset (blue) is compared to the introduced reconstruction algorithm (red) and to the reconstruction with a constant regularization (green). The red arrow marks a region where oscillations can be seen for the constant regularization and which are not present in the original or the normally reconstructed dataset.

To further highlight the advantage over deconvolution algorithms without the suggested prior and regularization, two slices from the head region of the zebrafish are shown in Figure 3.11. In the upper row (Figures 3.11a-d) a plane from a depth of around 140 μm is shown. The lower row with Figures 3.11f-i shows an image plane from the eye close to the surface at a depth of 5-10 μm. The original image slices can be seen in Figure 3.11a and 3.11f, the result from our algorithm in Figure 3.11b and 3.11g. The two planes in Figure 3.11c and 3.11h were reconstructed without the co-primeness prior and with a fixed PSF. There - instead of iteratively reconstructing both the PSF and the image - a fixed (simulated) Gaussian PSF was used. This kind of correction is widely used in microscopic imaging to correct for optical aberrations of the microscope. Figure 3.11d and 3.11i show a modified version of our algorithm where the same coprimness-prior is used but a constant regularization is applied. The amount of regularization was optimized for a depth of around 140 μm. This case is equivalent to the reconstruction of the dataset in the previously shown Figure 3.10f.

To visualize the difference between the three reconstructions Figure 3.11e and 3.11j show a cut through the images. The location of this cut though is indicated by a white dotted line in the original image. In Figure 3.11e a cut through the plane of $140\,\mu m$ depth is shown where the original dataset (blue) can be compared to the reconstruction with fixed PSF (green) and the result from our algorithm. The results from the constant regularization are identical to the results from our algorithm since the regularization was optimized for the depth of $140\,\mu m$. As expected our algorithm enhances structural contrast and is reducing the structure size in order to correct for the scattering, while the reconstruction with the fixed PSF falls behind. At this depth the PSF broadening due to scattering is much larger than the microscope PSF and therefore the PSF size in the fixed reconstruction is not sufficient to yield a better result.

At a depth of around $5\,\mu m$ the effect scattering has on the broadening of the PSF can be neglected, similar to the images in Figure 3.10d-f. Again it can be assumed that the original image 3.11f is very close to the ground truth. As already shown, excessive regularization can lead to artifacts in planes close to the surface. Figure 3.11j shows a cut through one of these planes at a depth of $5\,\mu m$. The reconstruction with constant regularization is plotted in cyan. Similar to the artifacts shown in Figure 3.10g the over-regularization of the PSF leads to the formation of oscillations around the edge of plateaus or bright structures. The plot in Figure 3.11j shows an oscillation at a position of around $50\,\mu m$ (marked with the red arrow). Our algorithm (red) and the fixed PSF reconstruction (green) are much closer to the original dataset at this point.

As a result of these oscillating artifacts, spatially overlapping objects of different intensity might artificially be separated. Besides the artifacts seen in this image other artifacts may appear depending on the imaged structure. For images from deep inside where the algorithm uses high regulariaztion, window artifacts similar to the artifacts discussed in section 3.3 might appear. However it should be mentioned that these artifacts appear at a point in depth when the image is already highly blurred due to scattering and no structural information can be retrieved. Furthermore these artifacts only appear in samples much bigger than the small 3 day old zebrafish shown here in Figure 3.9, 3.10 and 3.11.

Besides testing the algorithm on a zebrafish embryo, it was also applied to the dataset of an adult one-month-old zebrafish from the HGn39D transgenic line. The results were published by Amy Lin et al. in Laser Photonics Review [79].
In most biological studies zebrafish larvae of only a few days of age are used (similar to the 3 day old zebrafish shown above). In this early stage they are naturally transparent and only a few melanocytes have formed. The size of these larvae does not extend a few hundred micrometer in width and 2-3 mm in length and is therefore still within range of depth (or size) which is suitable for SPIM imaging or light microscopy in general. When the zebrafish is growing older, it becomes opaque and, of course, much larger. The zebrafish which was studied here measured 10 mm in length and 3 mm in diameter. The HGn39D transgenic line expresses
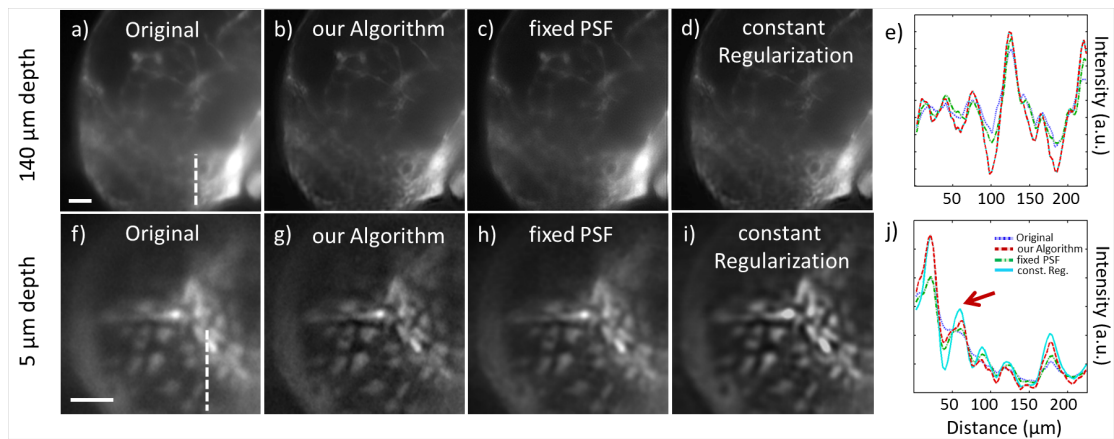
Figure 3.11: Comparison of Reconstruction with and without prior and regularization The head region of the zebrafish shown in Figure 2 is chosen and two different slices from the volume are picked.). The upper row a)-d) shows a plane from a depth of approximately 140 µm. The lower row f)-i) shows a plane from the surface (of the eye). In e) and j) a cut through the image planes is plotted. The location of the cut through is indicated by the white dotted line in the original images. In blue the original dataset is plotted, in red the results from our algorithm, in green the reconstruction with fixed PSF and in cyan the reconstruction with constant regularization. Artifacts produced by the constant regularization are marked with a red arrow. Scale bar indicates 100 µm

GFP at the afferent neurons of the lateral line systems.

The datasets were recorded with an older version of the SPIM system with a Zeiss Fluar $5\times/0.25$ objective. A $f = 40\,\text{mm}$ cylindrical lens was used to cover a larger FOV and account for the bigger sample. Again a step size of $5\,\mu\text{m}$ was chosen between each z-plane.

Figure 3.12a shows a MIP along the z-axis. Because of the used objective with a fixed magnification only a limited FOV could be acquired at the same time. Therefore, two SPIM measurements were taken. As indicated by the white gap the two image stacks do not cover the whole fish, but two ROIs, one covering the head region and one covering the tail of the zebrafish.

Several neuronal structures can be be identified in the head. Two of these structures are highlighted in Figure 3.12b and 3.12c. They show close-ups of a ganglion and the ventral axon, respectively. Depending on the depth of the different structures they experience different amount of scattering. This effect is visible in both panels. In Figure 3.12b the individual somata comprising the ganglia appear to be blurred because of scattering. In Figure 3.12c the ventral axon and the neurons, which extend to the neuromast cells are closer to the surface and can therefore be resolved much better. The same holds for the lateral line nerve, which extends over the whole tail of the zebrafish and is visible in Figure 3.12a on the right. In Figure 3.12d a photograph of the imaged zebrafish is shown. As seen in the photograph the zebrafish is completely opaque, hence strong scattering can be expected.
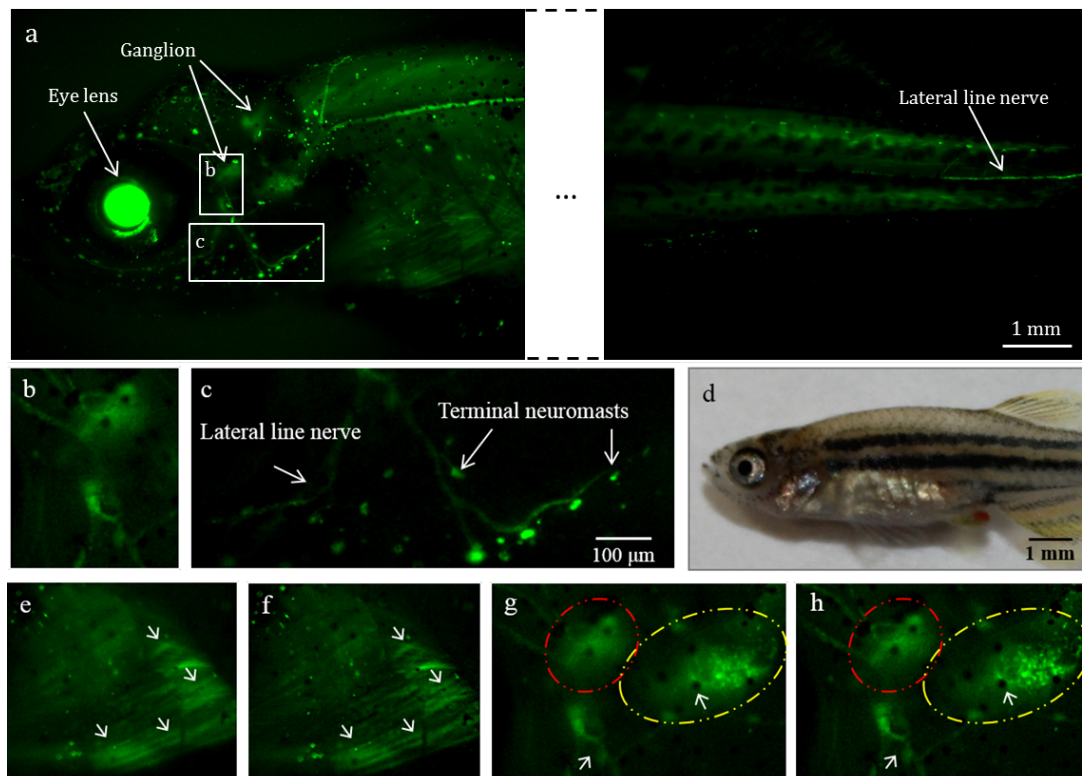
Figure 3.12: Experimental Results Adult Zebrafish a) MIP of a 1-month old zebrafish from the HGn39D line. The lateral line neurons are labeled with eGFP. Because of the sample size two image stacks were taken: one from the head region and one from the tail region. b) and c) are close-up of a ganglion and ventral axon arbors extending to neuromasts both from the head region of the SPIM image stacks. The location of both regions is indicated by a with box in a). d) Photograph of the zebrafish. e) and f) Autofluorescence of muscle fibers. e) shows the original image, f) the reconstructed image. The white arrows mark the muscle fibers, where improvement in image quality can be seen. g) and h) Ganglions (circled). The yellow arrows indicate melanocytes, and the white arrows point to a neuronal structure. Again e) is the original image and g) is the reconstructed image.

Figures 3.12e shows a region of the fish were autofluorescence of muscle fibers at a depth of around $30\text{-}40\,\mu\text{m}$ can be observed and Figure 3.12g shows a bigger region around the ganglion already depicted in Figure 3.12b. The ganglion spans over a depth of approximately $70\text{-}160\,\mu\text{m}$.To improve the image quality and correct for scattering, the introduced deconvolution algorithm was applied on the whole dataset and the results are shown in Figures 3.12f and h. It should be mentioned that due to the increased scattering in the sample compared to the previous larvae sample the factor β in front of the quadractically adaptive regularization had to be increased.

The muscle fibers in Figure 3.12f (white arrows) are sharper and better resolved after the reconstruction. In Figure 3.12h the cells in the large ganglion on the right (yellow circle) and neuronal structure at the bottom of the image (white arrow)

show a clear enhancement in contrast and a reduction of blurriness compared with Figure 3.12g. This is also partly true for the ganglion to the right (circled in red). Especially the loop structure on the top is enhanced, while the rest of the ganglion shows little to no improvement. Most of the ganglion structures are located at a depth of $100\,\mu$m and deeper. The algorithm is not capable of retrieving information from these highly scattered regions. The reason the maximal imaging depth is lower than in the previous sample is the increased scattering. While in the 3 day old larvae small structures at depth between $130\,\mu$m and $150\,\mu$m (depending on the position in the sample) could still be resolved, in the juvenile zebrafish the maximum imaging depth is under $100\,\mu$m.

Even the melanocytes in Figure 3.12g (marked with a yellow arrow), which are located at the surface of the zebrafish, look sharper in the reconstructed image. Since these structures are on the surface no scattering is expected and the slight blur in the original image is probably due to motion artifacts. The algorithm is also capable to compensate for these small distortions and improves the overall image quality.

In the reconstructions shown in this section, the selected step size of $5\,\mu$m was sufficiently small for a stable reconstruction. In the shown datasets, most observed features where at least three times larger than the step size. For samples with smaller labeled structures a smaller step size together with a thinner light sheet would probably be beneficial.

The acquired results show that the novel regularizer and the prior presented in this work are able to correct to some extent for scattering within the sample and enhance the image quality and depth. The adaptive regularizer effectively avoids over-regularization of the reconstruction. In the specific case of the zebrafish sample, the increase in imaging depth was about $30\,\mu$m. For this correction, only information from a single image stack was used, together with a simple model for the dispersive broadening of light in tissue. Tikhonov regularization was used efficiently as a model to account for an increased scattering, which comes along with an increased imaging depth. The advantage of this approach is that neither multiple image stacks have to be acquired, nor adaptations on the hardware level are required and the algorithm can be applied to already acquired data. The algorithm only requires a volumetric image stack with a small step size between two adjacent imaging planes, therefore the algorithm should also be able to work on other imaging techniques which provide a 3D image volume.

3.5 Outlook and possible adaptations for the used prior and regularization

The results from the imaged zebrafish show that the algorithm works on z-stacks of SPIM images. However, this does not mean that the algorithm is limited to this imaging modality. The algorithm should be able to work with other optical microscopy methods, as well as other imaging methods which are limited by the

scattering of light in tissue. There are three requirements which must be met: a full 3D image stack is available, the step size between two adjacent planes is small compared to the observed structures, and the scattering in the sample can sufficiently be described by the introduced model. While a single dataset was used for this demonstration, the algorithm can be extended to handle multiple datasets to form one sample, either with varying illumination or even with varying views of the sample.

4 Optoacoustic Tomography

Optoacoustic (OA) Imaging, also called photoacoustic imaging, is an imaging modality that emerged in the last two decades. The technique is based on light-induced generation of ultrasound. By utilizing acoustic waves, optoacoustic imaging circumvents one of the biggest problems of light microscopy, the limitation of the imaging depth because of light scattering. While light is strongly scattered in most biological tissue, ultrasound has a much smaller scattering coefficient. Compared to ultrasound imaging, the contrast in optoacoustic imaging does not originate from the elastic properties of the tissue but on the specific optical absorption contrast.

This chapter will give a brief introduction into the principles of optoacoustic signal generation, detection and reconstruction. We show that the knowledge about the influence of detection on the measured signal can be used to improve the reconstruction and therefore the final image quality, which confirms the results of Miguel Caballero et al. [80].

4.1 Optoacoustic principles

Opto- or photoacoustic imaging is based on the photoacoustic effect. This effect was first discovered by Alexander Graham Bell in 1880 [81]. He observed the generation of sound by the absorption of rapidly modulated sunlight. Following the discovery, very little scientific or technological interest was taken in the photoacoustic effect. Only with the development of lasers in the 1960s the technological basis was formed for further applications. The spectral purity and the high peak power of the new light sources successfully enabled trace gas analysis and other spectroscopic applications based on the photoacoustic effect. In the 1990s a first few research groups started to use optoacoustics for medical imaging [82,83]. However, it took until the mid-2000s for the development of this new imaging modality to gain momentum. Since then, several different setups of multiple purposes have been developed [84] (an overview of different scanning geometries can be found in chapter 2.1.2).

The principle behind optoacoustic imaging is illustrated in Figure 4.1. Typically a laser is used as a pulsed high power light source to illuminate the sample. Structures with a high absorption coefficient will absorb the incident light. The absorbing structures convert the light into thermal energy which causes a sudden expansion of the absorbing structure, also referred to as a transient thermoelastic expansion. If the illumination is not continuous, i.e only a short laser pulse is used, the quick thermal expansion is followed by a fast relaxation. This oscillation generates an ultrasonic wave which then travels through the sample and is often denoted as an
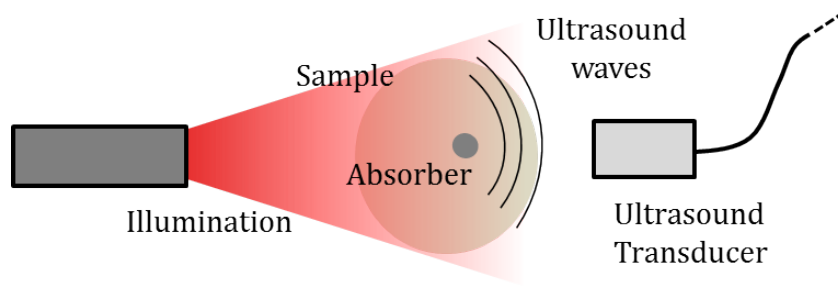
Figure 4.1: Optoacoustic principle An absorber within the sample is illuminated with a laser pulse. The absorbed energy creates a thermoelastic expansion and generates an ultrasound wave which can be detected with an ultrasound transducer

optoacoustic wave. Outside of the sample this optoacoustic wave is detected by an ultrasound transducer, which collects part of the emitted wave.

Normally one detector (position) is not sufficient to locate the origin of an incident arbitrary optoacoustic wave. To form a complete image of the sample, it is necessary to record the generated ultrasound from several positions/views. This is normally implemented either by moving the transducer relative to the sample and repeating the optoacoustic excitation or by the use of multiple detectors. The acquired signal is afterwards processed by image reconstruction algorithms to recover the distribution of all absorbers and form an actual image of the sample. More precisely, the reconstructed image shows the distribution of absorbed optical energy within the sample. The absorbed energy depends on both the illumination which is used and the optical properties of the sample. In the following sections the generation of the pressure wave and the propagation of the wave through the sample will be discussed. This knowledge will be necessary to understand the principles behind the reconstruction algorithms, which will be discussed later in this chapter.

For more detailed explanations, the reader is referred to [84–86] and especially the book "Biomedical Optics : Principles and Imaging" [87]. Most of the derivations and explanations as well as the structure in the sections 4.1.1 to 4.2 will be based on this book.

4.1.1 Initial optoacoustic pressure generation

Optoacoustic signals are generated through thermal expansion and relaxation. To generate an optoacoustic pulse, the intensity of the incident light has to vary over time in order to allow for thermal relaxation. The stronger the variation, the stronger the generated signal. This is why, most commonly, short laser pulses are used to excite the sample. However, it should be mentioned that also intensity modulated CW laser source can be used for optoacoustic imaging [88]. In the setup presented in this thesis a pulsed laser with a pulse width of 7 ns is used.

There are two time scales for the laser heating of the absorbers in the sample: the thermall relaxation time and the stress relaxation time. The thermal relaxation time τ_{th} characterizes the thermal diffusion during the laser heating. It indicates

how long it takes for the heat to diffuse to neighboring tissue. τ_{th} is determined by:

$$\tau_{th} = \frac{d_c^2}{\alpha_{th}}. \tag{4.1}$$

Here α_{th} is the thermal diffusivity (m^2/s) and d_c is the characteristic dimension of the heated region. d_c can be understood as the dimension of the (absorbing) structure in the sample. Smaller structures have a shorter relaxation time.
The second time scale is the stress relaxation time. This time scale characterizes volume expansion or the pressure propagation during the laser pulse:

$$\tau_s = \frac{d_c}{v_s}, \tag{4.2}$$

where $v_s = c$ is the speed of sound.

For small vessel of $d_c = 35\,\mu$m the corresponding thermal and stress relaxation times are $\tau_{th} = 22\,$ms and $\tau_s = 24\,$ns, respectively. For the laser pulse of $\tau = 7\,$ns used in the presented system, the excitation can be assumed to be in thermal or heat confinement. The time needed for the heat to diffuse to the surrounding tissue is much larger than the laser pulse itself and heat conduction during the pulse can be neglected ($\tau \ll \tau_{th}$). Similarly, stress confinement can be assumed, if the stress relaxation times is smaller than the used laser pulse. If the time scale of the volume expansion of the absorbing structure and the propagation of the sound wave is much shorter than laser pulse, the illumination can be assumed to be instantaneous ($\tau < \tau_s$).

The local change in volume due to the incident laser pulse (i.e the fractional volume expansion $\mathrm{d}V/V$) is given by:

$$\frac{\mathrm{d}V}{V} = \kappa p + \beta T, \tag{4.3}$$

where κ is the isothermal compressibility, β denotes the thermal coefficient of volume expansion, and p and T denote the change in pressure and temperature, respectively. As already mentioned, for the used laser pulse thermal and stress confinement can be assumed. Therefore, the fractional volume expansion is negligible ($\mathrm{d}V/V = 0$) [87]. Using equation 4.3 the (instantaneous) pressure rise p_0 after the laser pulse can be calculated as:

$$p_0(\vec{r}) = \frac{\beta T(\vec{r})}{\kappa}. \tag{4.4}$$

The temperature rise can be rewritten as a function of the local optical absorption coefficient $\mu_a(\vec{r})$ and the local optical fluence $F(\vec{r})$ (J/cm^2):

$$T = \frac{\mu_a(\vec{r})F(\vec{r})}{\rho C_V}. \tag{4.5}$$

Here ρ is the mass density and C_V is the specific heat capacity at constant volume. The ration of the thermal coefficient of volume expansion with the product of the isothermal compressibility, the density, and specific heat capacity at constant volume is called the (dimensionless) Grüneisen parameter Γ:

$$\Gamma = \frac{\beta}{\kappa \rho C_V}. \tag{4.6}$$

The Grüneisen parameter increases as the temperature rises. With this definition of the Grüneisen parameter equation 4.4 can be rewritten as:

$$p_0 = \Gamma \mu_a(\vec{r})F(\vec{r}) = \Gamma H_s(\vec{r}), \tag{4.7}$$

where H_s is the initial heating function. The generated signal not only depends on the optical properties of the sample (μ_a) but also on optical fluence $F(\vec{r})$ in the sample and therefore on the illumination used. When light enters a sample, it will get absorbed and scattered leading to an inhomogenious light distribution within the sample. The optical fluence is therefore spatially dependent.

For longer laser pulses, where the stress confinement is not valid anymore, the generated optoacoustic pulse can be calculated as a convolution of the laser pulse and the initial pressure distribution calculated above [89].
After the initial pressure distribution $p_0(\vec{r})$ is generated by the laser pulse, the pressure starts to travel through the sample as an optoacoustic wave. This propagation of pressure waves will be discussed in the next section.

4.1.2 Optoacoustic wave propagation

The general photo- or optoacoustic equation can be derived from the thermal expansion equation (generalized Hooke's law) and the linear inviscid force equation (linearized Euler equation for inviscid flow)(see [87] page 287 et seq.) and is given by:

$$\left(\nabla^2 - \frac{1}{c^2}\frac{\partial^2}{\partial t^2}\right)p(\vec{r},t) = -\frac{\beta}{\kappa c^2}\frac{\partial^2 T(\vec{r},t)}{\partial t^2}. \tag{4.8}$$

Here c is the speed of sound, $p(\vec{r},t)$ is the local pressure field at time t, and $T(\vec{r},t)$ is the local rise in temperature. The right-hand side of the equation can be seen as the source term, while the left-hand side describes the propagation. In thermal confinement and with the definition of the Grüneisen parameter in equation 4.6 the following equation emerges:

$$\left(c^2\nabla^2 - \frac{\partial^2}{\partial t^2}\right)p(\vec{r},t) = -\Gamma\frac{\partial H(\vec{r},t)}{\partial t},\tag{4.9}$$

where $H(\vec{r},t)$ is the heating function. The heating function H is defined as the thermal energy converted per unit volume and per time:

$$H(\vec{r},t) = \rho C_V\frac{\partial T(\vec{r},t)}{\partial t}.\tag{4.10}$$

Equation 4.9 shows that time invariant heating does not generate pressure waves. As already mentioned above only a variation or modulation of the heating in time - produced for example by a laser pulse - will generate acoustic waves.

Forward solution

To solve the general photoacoustic equation 4.8, a Green's function approach can be used. Therefore the response of the system to a Dirac-delta function (both in time and in space) is examined:

$$\left(\nabla^2 - \frac{1}{c^2}\frac{\partial^2}{\partial t^2}\right)G(\vec{r},t,\vec{r}',t') = -\delta(\vec{r} - \vec{r}')\delta(t - t').\tag{4.11}$$

The Green's function $G(\vec{r},t,\vec{r}',t')$ in this case corresponds to an impulse at the point r' at the time t', which will propagate outwards as a spherical wave:

$$G(\vec{r},t,\vec{r}',t') = \frac{\delta\left(t - t' - \frac{|\vec{r}-\vec{r}'|}{c}\right)}{4\pi|\vec{r} - \vec{r}'|}\tag{4.12}$$

While the Green's function for the spatial (Dirac-delta) response can simply be seen as an acoustic point source, the interpretation of the temporal delta function is not straight forward. Since the optoacoustic equation depends on the first derivative of the heating function (see equation 4.9) the delta function rather represents a step heating (Heaviside function) than an impulse heating [87, 89].
With this definition of the Green's function, the general photoacoustic equation becomes:

$$p(\vec{r},t) = \frac{\beta}{4\pi\kappa c^2} \int \, \mathrm{d}\vec{r}' \frac{1}{|\vec{r}-\vec{r}'|} \frac{\partial^2 T(\vec{r}',t')}{\partial t'^2} \bigg|_{t'=t-\frac{|\vec{r}-\vec{r}'|}{c}} \tag{4.13}$$

With equation 4.10 (still assuming thermal confinement), the equation above can be rewritten as:

$$p(\vec{r},t) = \frac{\Gamma}{4\pi c^2} \frac{\partial}{\partial t} \int \, \mathrm{d}\vec{r}' \frac{1}{|\vec{r}-\vec{r}'|} H(\vec{r}',t-\frac{|\vec{r}-\vec{r}'|}{c}) \tag{4.14}$$

In the next step the heating function is separated into a spatial and a temporal part: $H(\vec{r}',t') = H_s(\vec{r}')H_t(t')$. Assuming the temporal heating function corresponds to a delta-function ($H_t(t') = \delta(t')$) and the (inital) spatial heating function is given by equation 4.7, the function for the pressure field at point $\vec{r}$ and the time t (equation 4.14) becomes:

$$p(\vec{r},t) = \frac{1}{4\pi c^2} \frac{\partial}{\partial t} \left[\frac{1}{ct} \int \, \mathrm{d}\vec{r}' p_0(\vec{r}') \delta\left(t - \frac{|\vec{r}-\vec{r}'|}{c}\right) \right] \tag{4.15}$$

After the initial pressure field $p_0(\vec{r})$ is generated, two pressure waves of equal magnitude to opposite direction are created - one outwardly traveling wave and one inwardly traveling wave with inverted amplitude. Thus, the optoacoustic wave generally has a bipolar shape. The temporal distance between the two amplitudes is proportional to the size of the object [86, 89].

The smaller the object, the closer both peaks will be together. Therefore, the frequency spectrum of the generated optoacoustic wave will mainly depend on the size of the absorbing structure. However, this is only true for sufficiently short laser pulses. As stated in section 4.1.1, the assumptions and approximations are only valid if the laser pulse is much shorter than the stress relaxation time of the absorber. For laser pulses longer than this relaxation time, the frequency content and therefore also the spatial resolution of the recorded pressure field will be limited by the laser pulse width.

Since the used laser pulse is much shorter than the stress relaxation time of structures at the resolution limit of the used ultrasound transducer, the frequency spectrum measured by the transducer is not limited by the laser, but depends on the absorber size (and, of course, the bandwidth of the transducer). A deeper connection between absorber size, emitted frequency spectrum, and amplitude will be discussed in the following, where the solution of the equation 4.15 for a spherical absorber is derived.

4.1.3 Analytic solution for a spherical absorber

Equation 4.15 can be solved exactly under a couple of assumptions for a few simple geometries. These assumptions include uniform illumination and a constant light fluence in the sample. The geometries presented in [87] include delta excitation as well as finite excitation for cylinders and spheres. As mentioned earlier, the laser pulse can be assumed to be much shorter than the stress relaxation time of the absorber which is why the case of a delta excitation will be covered here. Furthermore, a spherical absorber will be chosen, since it is a simple and highly symmetric case and a lot of the characterization measurements were actually done on spheres. The calculated solution for this geometry has been shown to match the experimental results as shown by Diebold at al. [89].

When the (delta) laser pulse hits a sphere with radius R_s and with the absorption coefficient μ_a, the sphere heats up and an initial pressure p_0 is generated. This initial pressure field will propagate outwards (i.e., away from the sphere) and can be calculated by equation 4.15. Since the problem is symmetric, the pressure field only depends on the absolute distance r to the center of the sphere and the time t. The integral over the volume is substituted by an integral over a sphere with a solid angle θ and a radius $R = ct$. For points outside of the sphere ($r > R_s$) the integral will only be different from zero if the spherical shell with the radius ct intersects with the heated spherical absorber ($r - R_s \leq ct \leq r + R_s$). In this case the solution to the pressure field yields:

$$p(r,t) = \frac{p_0}{2} \frac{\partial}{\partial t} [t(1 - \cos\theta)] = \frac{p_0}{2} \frac{\partial}{\partial t} \left[t \left(1 - \frac{(ct)^2 + r^2 - R_s^2}{2rct} \right) \right] \tag{4.16}$$

$$= \frac{p_0}{2r}(r - ct) \tag{4.17}$$

Assuming initial pressure can be expressed with a Heaviside function U: $p_0(r) = p_0 U(r)U(-r + R_s)$ for $0 \leq r < R_s$, the solution for the pressure field becomes:

$$p(r,t) = \frac{r + ct}{2r}p_0(r + ct) + \frac{r - ct}{2r}p_0(-r + ct) + \frac{r - ct}{2r}p_0(r - ct) \tag{4.18}$$

Upon the heating due to the laser pulse, the initial pressure p_0 is generated within the sphere. The generated pressure splits into two equal parts with their amplitudes facing in opposite direction (first and third term on the right-hand side of the equation). While in this form, the bipolar nature of the emerging wave can be observed, the equation can be rewritten to emphasize the relationship between the amplitude and size of the emerging wave [89]:

$$p(r,t) = \frac{R_s p_0}{2r}(1 - \hat{\tau})[\tilde{\Theta}_{0,1}(\hat{\tau}) + \tilde{\Theta}_{1,2}(\hat{\tau})], \tag{4.19}$$

where $\hat{\tau}$ is the dimensionless time, measured from the edge of the sphere ($\hat{\tau} = \frac{c}{R_s}\left(t - \frac{r-R_s}{c}\right)$) and $\tilde{\Theta}_{a,b}(\hat{\tau})$ is a window function defined as 1 on the interval $a \leq \hat{\tau} \leq b$ and as zero everywhere else. As expected, the amplitude of the spherical wave will decrease with $1/r$. Furthermore, equation 4.19 reveals that the amplitude of the emitted wave is directly proportional to the size R_s of the absorber.

This effect can also be seen in Figure 4.2a, which plots the signal over time at a distance of $200\,\mu m$ from the center of the sphere for spheres of different sizes. For the calculation p_0 was set to 1 and the speed of sound c to $1500\,\text{m/s}$. Similar to the amplitude, the length of the signal is also proportional to the size of the absorbing sphere.
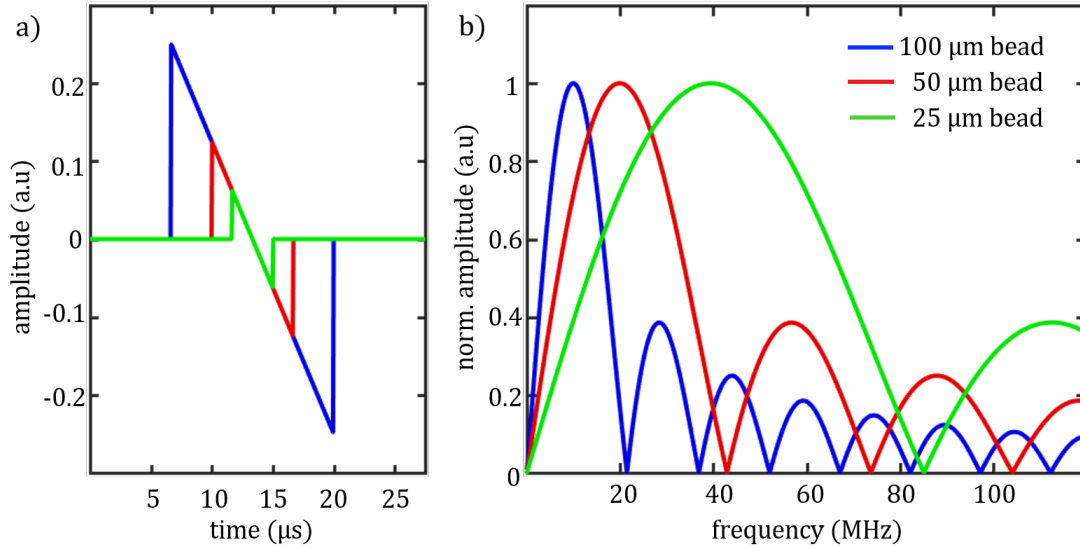
Figure 4.2: Analytic solution for a spherical absorber a) pressure distribution at the distance of $200\,\mu m$ from the sphere. b) normalized frequency spectrum of the emitted signal for the different bead sizes.

A shorter signal will translate into a higher frequency content of the signal. In Figure 4.2b the frequency spectrum of the signal for the different spheres is plotted. All plots are normalized to their peak frequency to better visualize the frequency spectrum. Without normalization the amplitude of the peak frequency decreases with $1/R_s$. In the plot it can be observed that the peak frequency shifts towards higher frequency for smaller spheres. Furthermore, the frequency spectrum gets wider. The frequency content of a signal can be characterized by its bandwidth.

One way of defining the bandwidth of a signal is using the FWHM of the peak in the frequency spectrum. More generally, the bandwidth can be defined by a threshold in frequency space. A threshold of -3 dB or -6 dB relative to the maximum frequency peak is set and the covered width in frequency space is defined as the bandwidth. The -3 dB and the -6 dB threshold correspond to the point where the power and the amplitude have dropped by about 50%. In the following, the spectral width at -6 dB will be used as the bandwidth.

The bandwidth of the signal gets larger for smaller spheres. Similar to the peak power in the frequency spectrum, the bandwidth is inversely proportional to the

Radius R_s of the sphere. In theory an infinitely small delta sphere would have an infinitely broad spectrum, but the amplitude of the signal and the peak power in frequency space would approach zero.

Since several different absorber sizes can normally be found in a biological sample, the recorded optoacoustic signal is typically wideband.

4.2 Optoacoustic image reconstruction

So far we discussed the generation and the propagation of the optoacoustic waves. However, at the end of the optoacoustic imaging process, a visualization of the absorber distribution should be attained. This section will look at how to use the optoacoustic signal to reconstruct the distribution of absorbers in the sample. As discussed in chapter 2.1.2 different scanning geometries can be implemented. While some geometries reduce the reconstruction to a two dimensional problem, the underlying wave propagation remains three dimensional.

To solve this problem, different analytical and algebraic approaches can be chosen.

Analytic methods include time-reversal [90] and backprojection algorithms [91]. In time-reversal, the optoacoustic waves are retransmitted in a reversed temporal order ($t \rightarrow -t$) and the photoacoustic wave equation 4.8 is solved 'backwards', going back from time point t' when the signal arrived at the detector to time point $t = 0$.

Backprojection algorithms are the most commonly used reconstruction algorithm for optoacoustic tomography. In analogy to X-ray computed tomography where the signal is backprojected along a line, the signal in optoacoustic tomography is back projected on a spherical shell. Backprojection algorithms can be applied in time and frequency domain. They are easy to implement and have the advantage that generally much less computational time is needed compared to most other reconstruction algorithms. In the following, the backprojection formula will be derived, and the algorithm will be used to reconstruct the measured experimental data.

In contrast to backprojection algorithms, algebraic or model-based algorithms are not based on the analytic solution of the wave equation [92]. The reconstruction is treated as an inverse problem and the progagation of the optoacoustic wave (i.e. the forward solution) is modeled as a linear operator. The measured signal is expressed as a matrix multiplication between the (unknown) initial pressure distribution and a model matrix, leading to a set of equations, which can then be solved iteratively or directly. The model matrix includes the geometry of the setup and a model of the propagation of the acoustic wave. The biggest advantage of the model-based approach is that further assumptions can be added to the model, such as a non-negative constraint for the reconstructed absorption distribution, the physical properties of the used ultrasound transducer, or even the tissue properties of the used sample.

The main disadvantage of model based approaches is that the reconstruction is computational much more demanding than backprojection algorithms. For recon-

structions with hundreds of different sensor positions the model matrix reaches sizes which can not be processed on normal PCs anymore. This becomes even more critical when the scanning geometry can not be reduced to a 2D case (although systems with implemented 3D-model based reconstruction have been demonstrated [93]).

4.2.1 Backprojection algorithm

The backprojection algorithm is an analytic approach to reconstruct the initial pressure distribution p_0 based on a set of pressure measurements $p(\vec{r_0},t)$ at the sensor positions $\vec{r_0}$.

Similar to the previous section an excitation with a delta pulse will be assumed, leading to an initial pressure distribution p_0. The wave propagation will follow equation 4.9 and the pressure wave will be detected by a point-like, ideal detector. A circular detection geometry which is shown in Figure 4.3 will be used for the derivation. The pressure will be measured along a cylinderical surface S_0 which encloses the absorber. Both the Figures and derivation of the backprojection in this section are based on [91] and [87]. In Figure 4.3 the detector on the surface S_0 at the position $\vec{r_0}$ is receiving an optoacoustic signal from the position $p_0(\vec{r})$.
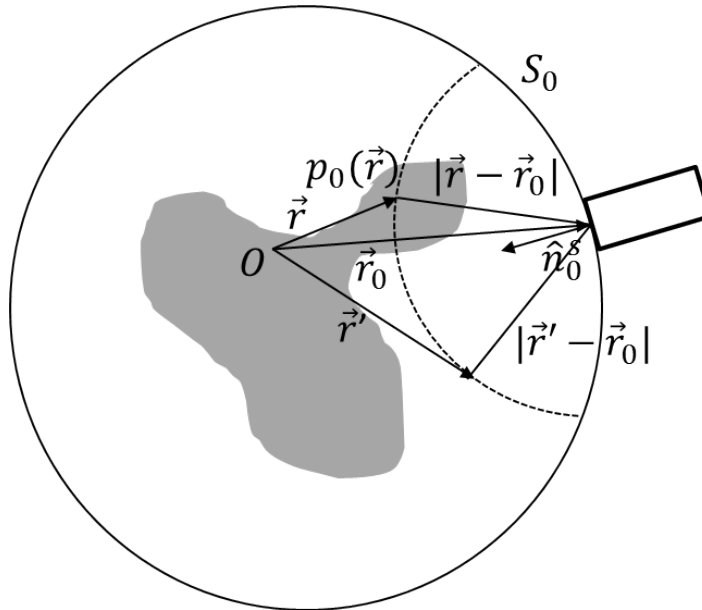
Figure 4.3: Tomographic reconstruction scheme The ultrasound transducer measures the pressure field at point $\vec{r_0}$ along the detection surface S_0. The optoacoustic signal is emitted from the source $p_0(\vec{r})$. For the reconstruction the signal measured at point $\vec{r_0}$ is modified and backprojected onto a circle with the radius $|\vec{r} - \vec{r_0}|$ with the center at $\vec{r_0}$ (adapted from [91]).

For the following derivation the Fourier transformation is defined as: $F(\bar{t}) = (1/2\pi) \int_{-\infty}^{+\infty} \tilde{F}(k) \exp(ik\bar{t}) \, \mathrm{d}k$ and $\tilde{F}(k) = \int_{-\infty}^{+\infty} F(\bar{t}) \exp(ik\bar{t}) \, \mathrm{d}\bar{t}$ for the variables $\bar{t} = ct$ and $k = \omega/c$. In Fourier space the frequency spectrum $\tilde{p}(\vec{r_0},k)$ of the pressure $p_0(\vec{r_0},\bar{t})$ can be written as [94]:

$$\tilde{p}(\vec{r}_0,k) = -ik \int_v \mathrm{d}\vec{r}\, \tilde{G}_k^{(out)}(\vec{r},\vec{r}_0)p_0(\vec{r}), \tag{4.20}$$

where V is a volume enclosing the source and $\tilde{G}_k^{(out)}(\vec{r},\vec{r}_0)$ is a Green function. This Green function corresponds to a diverging, outward going wave:

$$\tilde{G}_k^{(out)}(\vec{r},\vec{r}_0) = \frac{\exp(ik|\vec{r} - \vec{r}_0|)}{4\pi|\vec{r} - \vec{r}_0|}. \tag{4.21}$$

According the Green's theorem the Fourier spectrum $\tilde{p}(\vec{r},k)$ inside the surface S is given by

$$\tilde{p}(\vec{r},k) = \int_S \mathrm{d}S\tilde{p}^*(\vec{r}_0,k)[2\hat{n}_0^s \cdot \nabla_0 \tilde{G}_k^{(out)}(\vec{r},\vec{r}_0)]. \tag{4.22}$$

Here $\tilde{p}^*(\vec{r}_0,k)$ is the complex conjugation of $\tilde{p}$, ∇_0 is a gradient acting on r_0, and $\hat{n}_0^s$ is the normal vector on S (See Figure 4.3). Analog to $G_k^{(out)}$ the Green function $G_k^{(in)}$ of a converging, inward going spherical wave can be defined. With this function the initial pressure at the position $\vec{r}$ can be calculated

$$p_0(\vec{r}) = \frac{1}{\pi} \int_S \mathrm{d}S \int_{-\infty}^{+\infty} \mathrm{d}k\tilde{p}(\vec{r}_0,k)[2\hat{n}_0^s \cdot \nabla_0 \tilde{G}_k^{(in)}(\vec{r},\vec{r}_0)]. \tag{4.23}$$

The Green function $G_k^{(in)}$ is given by $\tilde{G}_k^{(in)}(\vec{r},\vec{r}_0) = \exp(-ik|\vec{r} - \vec{r}_0|)/4\pi|\vec{r} - \vec{r}_0|$. The derivation and the proof equation 4.23 can be found in [91]. When applying the inverse Fourier transform on $\tilde{p}$ in equation 4.23, the pressure p_0 can be written as:

$$p_0(\vec{r}) = -\frac{2}{\Omega_0}\nabla \cdot \int_{S_0} \hat{n}_0^s \,\mathrm{d}S_0 \left[\frac{p(\vec{r}_0,\bar{t})}{\bar{t}} \right]_{\bar{t}=|\vec{r}-\vec{r}_0|}. \tag{4.24}$$

Here Ω_0 is a solid angle of the entire surface S_0, which is 4π for the chosen cylindrical geometry. This analytic solution of the initial pressure distribution can also be seen as a backprojection of a term, which is related to the measured signal. The signal term which is measured at the time t is backprojected on a sphere with the radius $|\vec{r} - \vec{r}_0| = ct$ (Indicated by a dashed circle in Figure 4.3). To more clearly point out the backprojection character, equation 4.24 can be rewritten as:

$$p_0(\vec{r}) = \int_{\Omega_0} b(\vec{r}_0, \bar{t} = |\vec{r} - \vec{r}_0|) \frac{\mathrm{d}\Omega_0}{\Omega_0}, \tag{4.25}$$

where $\mathrm{d}\Omega_0$ is a fractional element of the solid angle Ω_0. This element together with the other variables in the backprojection equation is illustrated in Figure 4.4. This Figure shows how the solid angular element $\mathrm{d}\Omega$ is related to the detection element $\mathrm{d}S_0$ for a fixed point P (again this Figure is based on the illustrations in [87]).
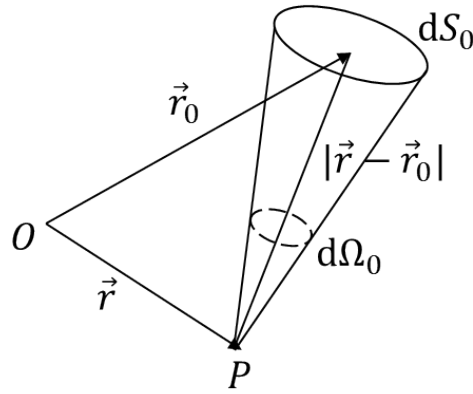
Figure 4.4: Solid angle $\mathrm{d}\Omega$ Scheme of the solid angle $\mathrm{d}\Omega$ for a detection element $\mathrm{d}S_0$ at $\vec{r}$ (adapted from [91]).

The second new function introduced in equation 4.25 is the backprojection function $b(\vec{r}_0, \bar{t} = |\vec{r} - \vec{r}_0|)$, which will backproject a signal on the sphere with the radius $\bar{t} = |\vec{r} - \vec{r}_0|)$ around the point $\vec{r}_0$. The element $\mathrm{d}\Omega$ and the function $b(\vec{r}_0, \bar{t})$ are given by:

$$b(\vec{r}_0, \bar{t}) = 2p(\vec{r}_0, \bar{t}) - 2\bar{t}\frac{\partial p(\vec{r}_0, \bar{t})}{\partial \bar{t}} \tag{4.26}$$

$$\mathrm{d}\Omega_0 = \frac{S_0}{|\vec{r} - \vec{r}_0|^2} \frac{\hat{n}_0^s \cdot (\vec{r} - \vec{r}_0)}{|\vec{r} - \vec{r}_0|} \tag{4.27}$$

The backprojection function consists of two terms. The first term directly backprojects the recorded pressure signal and the second term backprojects the time derivative of the pressure field. For most optoacoustic setups and detections the following condition is met: $k|\vec{r} - \vec{r}_0| \gg 1$. Therefore $\bar{t}\partial p(\vec{r}_0, \bar{t})/\partial \bar{t} \gg p(\vec{r}_0, \bar{t})$ and equation 4.26 can be approximated with:

$$b(\vec{r}_0, \bar{t}) \approx -2\bar{t}\frac{\partial p(\vec{r}_0, \bar{t})}{\partial \bar{t}} \tag{4.28}$$

The backprojection formula 4.25 recovers the initial pressure distribution $p_0(\vec{r})$. To obtain the actual absorption μ_a within the sample equation 4.7 has to be used:

$p_0 = \mu_a(\vec{r})F(\vec{r})$. If the optical fluence throughout the whole sample is constant, the absorption can be assumed to by directly proportional to the reconstructed initial pressure p_0.

However, the assumption of a constant optical fluence is not necessarily true, espically for larger samples of several mm in with. Even if the illumination on the outside of the sample is homogeneous, absorption within the sample will change and decrease the light fluence. This change in fluence will distort the reconstructed values for the absorption if a constant illumination is assumed. The lack of knowledge about the light fluence in the sample makes quantitative imaging very challenging, since the reconstructed values are not necessarily proportional to the actual absorption. However, there are attempts to correct for the light fluence in the sample [95, 96]. In the presented setup the illumination was homogenized by the used optical components, however, no computational correction of the light fluence within the sample was performed. For small samples the approximation of a homogeneous light fluence within the sample will be sufficient, but for samples of several millimeter width, derivations of the reconstructed and the actual absorption can be expected. Furthermore, a reference is needed to calculate the real absorption coefficient or the concentration of an absorber with known absorption. Therefore, no quantitative imaging was performed in the setup.

In this section a cylinderical geometry was assumed and discussed. As shown in [91] the analytical solution derived here is also valid for other geometries such as a planar or spherical geometry (see chapter 2.1.2).

While for the ideal case discussed in the section above, the solution is the same for all geometries, the physical properties of the transducer and the finite number of detector positions will affect the quality of the reconstruction for the different detection geometries. The solution for the absorber distribution derived here assumes an ideal point detector. In an actual measurement the transducer properties will have a significant impact on the measured signal. The influence of the detector properties and the scanning geometry on the measured signal will be discussed in the next sections.

4.3 Detection of the optoacoustic wave

The reconstruction presented in the previous section is based on the measurement of the pressure field at certain positions outside the absorber. In the ideal case the detector is assumed to be point like and perfectly reproduce the pressure field at this point. In reality the physical properties of the transducer will alter the measured signal.

Instead of measuring the exact pressure field at one point, the recorded signal will depend on several factors including the shape and orientation of the transducer as well as its material and electronic characteristics. By incorporating the effects

of the transducer on the measurement into the reconstruction, the reconstruction quality can be significantly improved [80, 97].

In the following, the characteristics of the transducer, their influence on the image, and possibilities to correct for there influence in order to improve the image quality will e discussed. The idea to correct for the electrial and spatial properties of a transducer has been introduced by Rosenthal et al. [97] and already been implemented into different systems [80].

4.3.1 Transducer material and the piezoelectric effect

There are several types of different detector types with different properties. In the following a short overview of the different detector types will be given.

The most commonly used detectors are piezo detectors. The detection of ultrasound by theses transducers is based on the piezoelectric effect. Most common ultrasound transducers are commercially available in several different shapes for a broad range of different applications, such as medical ultrasound imaging and non-destructive testing.

The piezoelectric effect can be described as the generation of an electrical field (i.e. a voltage) under the deformation of certain solids. The voltage is proportional to the deformation of the material. An incoming ultrasound wave will compress and expand the solid when traveling through the material [98]. This deformation can be measured through the generated voltage.

The piezoelectric effect is also reversible - applying a voltage to the piezo material will create a deformation. Therefore, the piezo material is not only able to measure ultrasound but also to create an ultrasound wave when applying a fast oscillating voltage. The inverse piezoelectric effect is used in conventional ultrasound imaging where an ultrasound pulse is created by the transducer. The pulse propagates through the sample and is reflected by internal structures with an impedance mismatch to the surrounding tissue. Finally, the reflected ultrasound is measured by the transducer. In contrast to the transmit and receive scheme of conventional ultrasound imaging, in optoacoustic imaging the transducer is only in passive mode receiving incoming acoustic waves. Several different materials show the piezoelectric effect. The three main types of materials for ultrasound detectors are ceramics, polymers and piezo-composite materials.

The most commonly used piezoelectric ceramic is lead zirconate titanate (Pb(Zr, Ti)O_3 or PZT), which has a strong piezoelectric response [98].
The sensitivity of a detector is not only determined by the piezoelectric response but also by the size of the detector element and by the coupling of the ultrasound into the piezo material. The higher the impedance difference between the material and the surrounding medium, the smaller the percentage of the ultrasound which is coupled into the medium. Piezoelectric ceramics are stiff solids with high densities,

compared to the surrounding water. Therefore, a high impedance mismatch between the detector and water is present [98].

To couple more ultrasound into the ceramic detector, typically one or multiple matching layers are used. These matching layers gradually adapt the impedance of the piezo material to the impedance of the surroundings [99].

Besides sensitivity, bandwidth is one of the most important characteristics of a detector. The center frequency of a transducer is primarily defined by the thickness of the piezoelectric ceramic layer. The bandwidth of the transducer is the width of the frequency spectrum around the center frequency the transducer is able to detect with a 6 dB threshold. Often the bandwidth is specified in percentage of the center frequency. As already discussed in section 4.1.3, the emitted optoacoustic frequency spectrum of a sample is typically a broad. A large bandwidth of the transducer is required to be able to image structures of different dimensions. Piezoelectric ceramic detectors normally have a narrow bandwidth. The matching layers will reduce the bandwidth even further.

Another established manufacturing material for ultrasound transducers are piezo-electric polymers, with polyvinylidence difluoride PVDF being the most commonly used one. The polymer PVDF is much more flexible than the stiff PZT, allowing easier processing and manufacturing of larger curvature radii. The lower stiffness also results in a much lower impedance mismatch between the detector and the water, so that normally no matching layer is needed. As a consequence, the bandwidth of PVDF transducers is higher than the bandwidth of ceramic transducers.

Piezo-composite materials are a combination of piezoelectric ceramics and piezoelec-tric polymers. By embedding ceramic sensors into a piezoelectric polymer matrix the advantages of both materials are combined. These composite detectors inherit the good sensitivity of the piezoelectric ceramics but at the same time they offer a much better coupling and a larger bandwidth due to the polymer.

Besides piezo based transducers, other detection methods have been developed. All optical detector such as Fabry-Pérot sensors, polymer microring resonators, or fiber bragg sensors use the change in interference of light due to ultrasound propagation [24, 100].

A rather new technique are silicon based Capacitive Micromachined Ultrasound Transducers (cMUT). These transducers can be manufactured by standard litho-graphic processes. Small cavities are arranged on the silicon chip. Incoming ultrasound generates oscillations of the enclosing membranes and these oscillations translate into changes in voltage, which can be measured [101].

The transducer used in the presented system is a cylinderically focused piezo-ceramic detector array with 128 elements. Each element has a size of $55 \times 1500\,\mu$m and the pitch between the elements is $70\,\mu$m. The transducer has a center frequency

of 24 MHz and a bandwidth of 51%. The choice of material was dictated by the specifications of the element size and the element focusing.

4.4 Electrical impulse response (EIR)

The electrical output signal is altered by the electrical properties of the transducer. The electrical impulse response (EIR) is defined as the response of the transducer to an impulse (delta) excitation and spatially independent on the location of the optoacoustic source. In the frequency domain the excitation with a delta pulse corresponds to an excitation with a constant, infinitely wide frequency spectrum. In frequency space the EIR corresponds to the frequency response of the transducer. Depending on the electrical properties, the transducer will only be sensitive to a limited range of the frequencies. This range of frequencies is also referred to as the bandwidth of the transducer.

One factor which will contribute to the EIR are the detector materials. The piezoelectric material but also the backing of the active material and the matching layers will influence the EIR. The bandwidth and therefore also the EIR will depend on whether a polymer, a ceramic or a composite detector is used (see section 4.3.1). Furthermore, the thickness of the detecting layer will influence the center frequency of the transducer as well as its bandwidth. In general the sensitivity of a transducer drops for higher center frequencies and larger bandwidths.

The voltage signal produced by the piezo material will be altered by the electronic transmission and the connected electronics such as amplification. Finally the data acquisition will convert the voltage signal into a digital signal. All these factors will contribute to the overall EIR.

The EIR can be modeled as a linear process and the effect on the signal can be described as a convolution of the EIR and the signal. Assuming a pressure field $p(\vec{r}_0)$ at the detector position $\vec{r}_0$ the measured pressure signal $p'(\vec{r}_0)$ can be written as

$$p'(\vec{r}_0) = H_i * p(\vec{r}_0) + N. \tag{4.29}$$

Here H_i is the EIR and N is a noise term. This equation is similar to equation 3.4 and the EIR can be seen analog to a PSF of an imaging system (this will be discussed further in section 4.6.1).

In conventional pulse-echo ultrasound imaging the emitted and the received signals are both affected by the EIR. Therefore, the effictive bandwidth which is used for imaging is approximately two times wider in optoacoustic imaging than in conventional pulse echo ultrasound imaging [28].

4.4.1 Measuring the EIR

Since the detection process can be seen as a linear system given by equation 4.29, the EIR H_i can be measured as the response of the system to a Dirac-delta pulse, or equivalently to an infinite broadband signal (This assumption neglects the noise N introduced to the imaging acquisition system).

Experimentally there are multiple methods to determine the EIR [97]. The detector can either be excited with a short broadband acoustic pulse, or the detector is excited with a pulse of known a spectrum and the EIR is calculated from the derivation of the measured signal form the input signal.

Here the excitation with a short broadband pulse is chosen[1]. A small polystyrene microbead with a diameter of 10 µm is used as a broadband (point) source. If the initial pressure field in the forward solution (equation 4.15) is replaced with a delta function $p_0(\vec{r}) = \delta(\vec{r})$ the measured acoustic signal $s(t)$ can be approximated by [97]

$$s(t) \approx \frac{\partial H_i(t)}{\partial t}, \tag{4.30}$$

where $H_i(t)$ is the EIR of the transducer. However, the approximation is only valid when the incoming signal is not altered by the transducer shape, i.e. arrives at the whole detector surface at the same time. This is the case when the pressure source is placed in the focus of the detector. Following equation 4.30, the EIR can be obtained by integrating the measured signal:

$$H_i(t) = \int\limits_0^t s(t')\,\mathrm{d}t' \tag{4.31}$$

As discussed in section 4.1.3, the frequency spectrum of the signal emitted from a small sphere has an almost linear slope until the center frequency is reached (see Figure 4.2). Integrating over the signal will create a flat frequency spectrum. Therefore, all spheres with a center frequency sufficiently larger than the bandwidth of the transducer can be used to calculate the EIR. The temporal sampling of the data acquisition system (DAQ) is expected to have little influence on the measurement since the frequency range the transducer is able to detect is significantly lower than the frequency spectrum which is covered by the DAQ (and the incorporated anti-aliasing filter).

The experimentally measured signal of the 10 µm bead can be seen in Figure 4.5a. It should be noted that the sign of the incoming signal is switched by the electronics

---

1 The results shown in this section were measured with the collaboration of Paul Vetschera, who also contributed to the later reconstruction/deconvolution in section 4.8.3
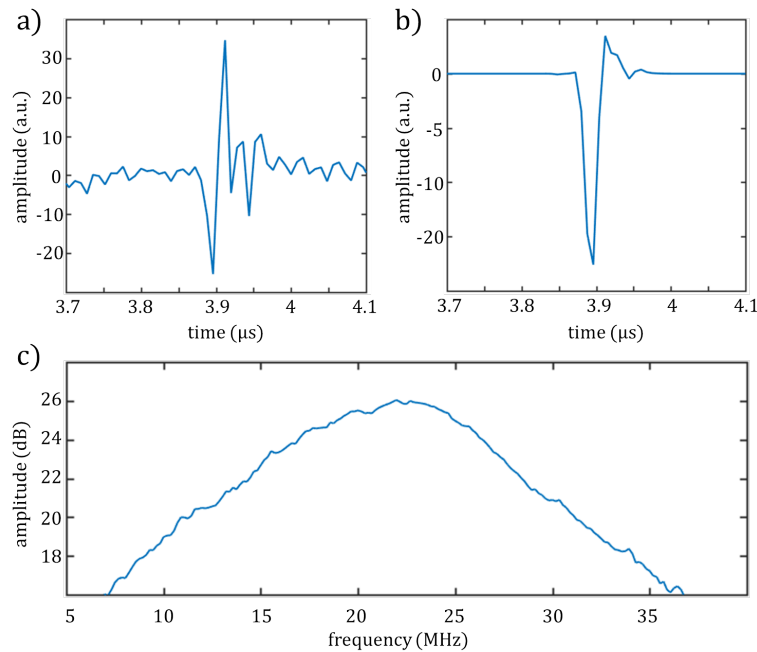
Figure 4.5: Measured EIR a) raw signal of a $10\,\mu$m bead placed in the focus of the transducer at a distance of $5.9\,$mm. b) EIR calculated from the the raw signal. The raw signal is filtered by a Gaussian window in time domain and integrated. c) measured bandwidth of the transducer

which are connected to the transducer. The physical pressure wave has a positive amplitude, followed by a negative pressure (see section 4.1).

Since the amplitude of the pressure signal is proportional to the size of the bead (see section 4.1.3), the signal from a small bead will be weak. To push the signal to noise ratio (SNR) to a level of around $16\,$dB, 50 averages were taken. Furthermore, the measurement was performed in a system with a significantly higher laser energy of $80\,$mJ at a wavelength of $800\,$nm and a pulse width of $8\,$ns. The bead was embedded in an agarose cylinder and both the transducer and the bead were submerged in water. To find the optimal focal position with the highest amplitude, the bead was scanned through the focal region. The signal shown in Figure 4.5a is filtered by a $0.1\,$MHz high-pass filter to remove low frequency noise and the DC offset of the signal which is introduced by the DAQ. Before the integration, the signal was further filtered with a Gaussian window to cut out the signal and remove the surrounding noise. The resulting EIR can be seen in Figure 4.5.

By using a standard deconvolution algorithm (see chapter 3.2), a better estimation of the original pressure distribution can be found. The results of the EIR correction can be found in section 4.8.

Besides the EIR, the frequency response or bandwidth of the transducer was determined. The plot in Figure 4.5c shows the frequency spectrum of a $20\,\mu$m bead

in front of the central elements of the transducer with 2000 averages. The plotted spectrum is averaged over the spectra of the 6 central elements. Furthermore, a moving average filter with a step size of 10 was applied to the spectrum. The measured center frequency 22.5 MHz of the array is lower than 24 MHz , which was the specification of the manufacturer. In the plot a -6 dB bandwidth of 89% of the center frequency can be read out. As mentioned earlier the bandwidth measured in pulse-echo mode is smaller than the bandwidth in optoacoustic since the signal is affected by the EIR twice. The common ultrasound bandwidth can be approximated with the the -3 dB bandwidth of the transducer. The resulting bandwidth of 59% is slightly larger than the bandwidth of 51% which is specified and measured by the manufacturer. However, the bandwidth specified by the manufacturer is an average over all elements, while the bandwidth in Figure 4.5c is only an average over the 6 central elements.

4.4.2 Noise characteristics and sensitivity of the detector elements

The EIR in the section above was calculated with the signal from the center element. However, not all 128 detector elements will have the same EIR and the same sensitivity. In fact transducer arrays often suffer from 'defect' elements with significantly lower sensitivity. Furthermore, the measured signal will be influenced by the noise of the acquisition signal, as seen in equation 4.29. Besides the EIR an additional noise term N will add up to the measured signal. This noise is typically Gaussian or white noise introduced by the transducer and the data acquisition system.

However, there will also be noise influences form the environment including electronic noise from the laser, the motor stages, or other electronic devices. Furthermore, reflections within the transducer cable can induce interferences. Since this electronic noise is not a random noise but comes from specific electronic signals, the noise is normally not Gaussian or white noise but has a characteristic spectrum. Understanding and characterizing the noise (spectrum) of an acquired signal can help to identify noise sources and reduce them, either on a hardware level or by filtering. Therefore, the noise spectra of the acquisition system will be reviewed in the following.

To analyze the noise the power spectral density (PSD) of the noise spectra will be estimated. The PSD describes the distribution of the power over the frequency spectrum of the signal. It can be estimated in a periodogram, which shows the Fourier transform of the auto-correlated time signal.
The noise signal is measured under the same environment as a regular measurement. Only the laser beam is blocked by a beam stop before it enters the sample chamber to avoid the creation of optoacoustic signal which could disturb the noise measurement. 5000 averages for each of the 128 elements are acquired. Figure 4.6 shows the average PSD for all 128 elements. Each element is plotted in a different color. In black the average over all elements is shown.
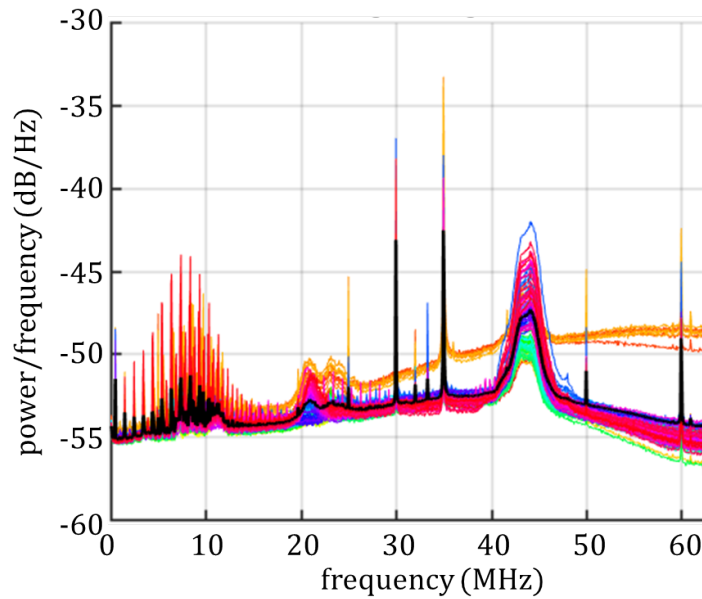
Figure 4.6: Noise power spectral density Periodogram of the noise in the acquisition system. Every transducer element is plotted in a different color. The black plot shows the average over all elements.

While most of the elements show roughly the same behavior, 16 elements show an overall increased noise level especially of the higher frequencies above 20 MHz. The anti-aliasing filter of the data acquisition cards of these 16 elements were set to a higher bandwidth of 50 MHz to eventually test higher frequency transducers. At some frequencies specific noise peaks can be detected. These peaks are located in the lower frequency band between 1 and 12 MHz, and at the frequencies of 25, 30, 35 and 42.3 MHz.

By using a bandpass filter the low and high frequency noise can be eliminated. Empirically a bandpass filter between 2 and 40 MHz has proven to filter out a large part of the noise without discarding signals from the sample.

Besides different levels of noise, the 128 elements of the transducer will show a different sensitivity. To compare all transducer elements, the SNR of each element for a selected phantom is determined. For this purpose, a long carbon rod with a diameter of 500 µm was placed in front of the elements and illuminated by the homogeneous optoacoustic illumination implemented in the setup. The SNR for all elements is plotted in Figure 4.7.

The plot shows 11 elements with a significant lower SNR. While the noise level of all transducer elements is similar (except the noise level of the first 16 elements with the change anti-aliasing filter), the sensitivity of these 11 elements is much lower than the sensitivity of the other elements. The second effect visible in the plot is a lower SNR of the first 22 elements. The main reason these elements show a lower SNR
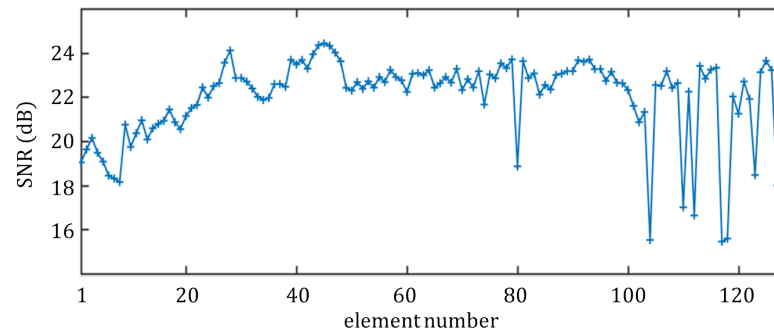
Figure 4.7: SNR comparsion of all detector elements The homogeneous illumination does not cover the region in front of the first 22 elements. 11 elements with a significant lower SNR can be determined.

compared to the rest of the transducer, is the alignment of the illumination. The field of illumination in the sample chamber is slightly shifted relative to the center of the transducer. Therefore, the illumination does not cover the region in front of the first 22 elements. The signal measured from these elements was not emitted in front of the elements but at an angle, resulting in a larger distance between the emitter and the detector, and a lower signal strength. A second effect on the SNR of the first 16 elements is given by the increased noise level as seen in Figure 4.6.

The knowledge about the sensitivity of the different elements can be used to correct the measured signal or reject signal from defect transducer elements. However, since the sensitivity of most elements is quite homogeneous and only a few elements show a significantly lower sensitivity, the effect on the final reconstruction turned out to be negligible.

4.5 Spatial impluse response and the sensitivity field

4.5.1 Transducer shape and focusing

Transducers can be found in various shapes and sizes. Often single transducer elements are combined to an array of elements, like the array used in this thesis. The different shapes serve different purposes and are chosen according to their field of application. Focusing of a detector can be achieved either through an (acoustic) lens or through the shape of the transducer itself.
In the following, basic transducer shapes and their focusing will be discussed. This will help to understand the choice of the transducer and the scanning geometry for the presented optoacoustic setup as well as the impact of the transducer shape on the measured signal which will be discussed later in this section.

Unlike ideal point detectors, real detectors typically do not detect all ultrasound wave regardless of there origin and the related incident angle. Similar to optical detection systems such as microscope objectives, ultrasound detectors only have a certain acceptance angle θ or numerical aperture (NA). The detector is only

sensitive to signals coming from the area within the aperture angle θ. More precisely, the sensitivity field of a transducer describes the relation between the amplitude of the incoming signal depending on the spatial origin of the signal. The focus of a detector is the region where it is most sensitive for emerging ultrasound waves (in the reverse case of normal ultrasound imaging, when the transducer is not receiving but emitting ultrasound, the focus is the region where generated waves overlap and the highest acoustic pressure can be found).

The simplest detector shape is an unfocused, round, and flat transducer. The field directly in front of the transducer is the near field. At the transition between the near field and the far field, a weak "natural focus" is generated. Behind the focus the sensitivity of the transducer diverges with a distinct aperture angle θ. Both the focal position and the aperture angle of an unfocused transducer only depend on the radius of the detector and the wavelength of the acoustic signal. The position of the focus is given by [98]: $z_0 = r^2/\lambda$, with r being the radius of the round detector surface and λ being the wavelength of the acoustic wave. The aperture angle θ of the diverging sensitivity field behind the focus can be approximated by:

$$\sin(\theta/2) = 0.61\lambda/r. \tag{4.32}$$

The larger the area of the detector the more "forward looking" the detector will be. The focus will shift further away from the detector and the focal depth will increase. Furthermore, the NA will get smaller making the transducer only sensitive for objects which are directly facing the transducer. In contrast, smaller detectors will have a larger acceptance angle giving them a wide field of view.

Focused transducers enhance the signal coming from the focal region and at the same time reduce the focal width. Spherically focused transducers confine the focus symmetrically in all direction. A schematic of a spherical focused detector can be found in Figure 4.8.
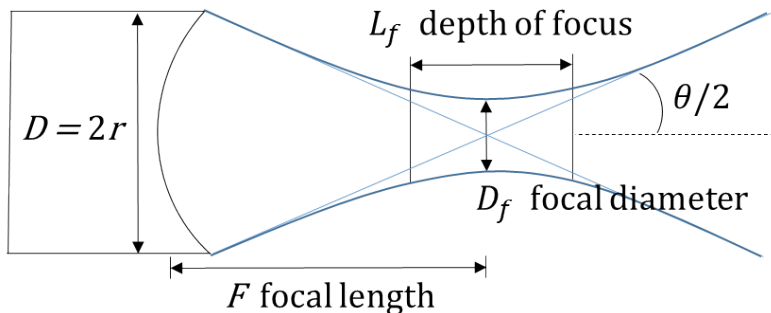
Figure 4.8: Spherical focused transducer Pressure profile of a spherical focused transducer. This approximation is valid for $F < D^2/(2\lambda)$.

Similar to the unfocused case, the focal depth L_f and the focal width D_f depend on both, the size of the detector and the wavelength of the incident acoustic wave.

The focal position is primarily defined by the focal length F of the transducer. Similarly, the aperture angle will depend on the focal length and the diameter of the transducer as seen in Figure 4.8.

$$\sin(\theta/2) = \frac{r}{F} \tag{4.33}$$

However, this approximation is only vaild for $\lambda F/r^2 \ll 1$. For low frequencies the focus will loose its shape and the aperture angle will increase. Analog to a focused optical lens, the focal width will decrease for a larger aperture or equivalently for a larger detector radius:

$$D_{f(6\,dB)} \approx 1.4\frac{\lambda F}{2r}. \tag{4.34}$$

In the same way the depth of the focus L_f will decrease for larger detector sizes

$$L_{f(3\,dB)} \approx \frac{1.8\lambda}{\sin^2(\theta/2)} = 1.8\lambda\frac{F^2}{r^2} \tag{4.35}$$

Cylindrically focused transducer, including the cylindrically focused array used in the presented system, are only focused in one direction, while the second direction remains unfocused.

The focusing of a transducer is either achieved by a lens in front of the transducer or by bending the surface in a convex shape. The later technique is mostly used by PVDF and piezo-composite transducers. The more flexible polymers allows much higher bending radii, which can not be achieved with ceramic detectors. Ceramic (PZT) detectors are often focused through a lens, especially when strong focusing is required. This applies also for the array which is used in this thesis.

4.5.2 Spatial impulse response (SIR)

The shape and the focusing of a transducer has a critical influence on the amplitude of the measured signal, depending on the origin of the signal. However, the amplitude is not the only characteristic of the signal which changes. The shape and width of the acquired signal is spatially dependent on the origin of the signal. The deformation of the signal due to is spatial dependence is called spatial impulse response (SIR).

When an optoacoustic signal arrives at the transducer, it does not necessarily arrive at each point r_a on the detector at the same time. The measured signal p_m in fact is a spatial average of the pressure field over the detector surface S [80]:

$$p_m(t) = \int_S p(\vec{r}_0, t) \, \mathrm{d}S \tag{4.36}$$

To understand the effect of the sensor shape on an actual signal, a point-like source at the position $\vec{r}$ is assumed and the pressure is propagated according to equation 4.15. Inserting this solution into equation 4.36 above yields:

$$p_m(\vec{r}, t) = h(\vec{r}, t) = \int_S \frac{\delta\left(t - \frac{|\vec{r}_d s - \vec{r}|}{c}\right)}{|\vec{r}_d s - \vec{r}|} \, \mathrm{d}\vec{r}_d s, \tag{4.37}$$

where $\vec{r}_d s$ are positions on the detector surface S. The function $h(\vec{r}, t)$ is referred to as the spatial impulse response of the detector (except a missing scaling/normalization factor) [28]. The deformation of the signal through the SIR can be modeled as a linear process [102]. Therefore, the altered signal can be expressed as a temporal convolution of the original signal and the SIR, similar to the deformation of the signal due to the EIR (see section 4.4).

If the transducer is curved with a certain radius r_f, signals from the center of the curving sphere (or cylinder for cylindrical focused transducer) will arrive at the detector surface at the same point in time and the signal will remain unchanged. This way the focusing of the transducer can be understood. Signals from outside the focus (i.e. the center of the transducer surface shaping sphere) will not be "smeared out" by the spatial impulse response. The larger the detector the more of the spherical acoustic wave at the focus will be collected by the surface of the detector resulting in a higher measured signal amplitude and therefore a higher sensitivity of the transducer. A lens in front of the transducer practically achieves the same effect. Through the higher speed of sound inside the lens, the arrival time of the signal at the surface of the transducer will be altered. Similar to the physically shaped transducer, signals from the focus will arrive simultaneously at the detector surface.

The spatial impulse response can also be used to calculated the sensitivity field of a transducer. More precisely, the sensitivity field of a transducer can be referred to as the amplitude of the SIR. The amplitude of signals from outside the focus and outside the acceptance angle of the transducer will diminish and at some point drop under the detectable threshold of the transducer, portraying the effective sensitivity field of the detector.

The sensitivity field of a transducer will define the signal strength of an incoming acoustic pressure wave, based on the position of its origin relative to the position of the transducer. Understanding the sensitivity field of a transducer and the related focal position and size is important for adapting the scanning geometry and step size. Furthermore, the knowledge about the sensitivity field can be used to improve

the reconstruction which will be shown in section 4.8.

There are two methods which can be used to determine the sensitivity field of a transducer. The field can either be computationally simulated or measured. In the following both methods will be used to determine the sensitivity field of the used transducer.

4.5.3 Computationally modeled sensitivity field

To simulate the SIR and the resulting sensitivity field the Matlab toolbox Field II [103] is used. The program can be used to simulate all common piezo-transducer shapes, from single element transducers to transducer arrays.

The SIR can be calculated with equation 4.37, which is derived in the previous sections. However, this equation can only be analytically solved for a few special cases such as a spherically focused single element transducer. Instead of solving the equation for a complex surface S, the Field II program divides the surface into several smaller, flat (square) patches and solves the equation for each of them. All results for the sub-surfaces are summed up coherently to obtain the overall SIR of the transducer.

The sensitivity field of a transducer is highly frequency dependent. Since the optoacoustic signal from most sample is inherently a broadband signal (see section 4.1.3), the frequency dependency of the sensitivity field has to be considered for transducers which cover a large bandwidth.

The Field II program allows to freely choose the signal which is propagated to the transducer and can therefore simulate the sensitivity field for different frequencies.
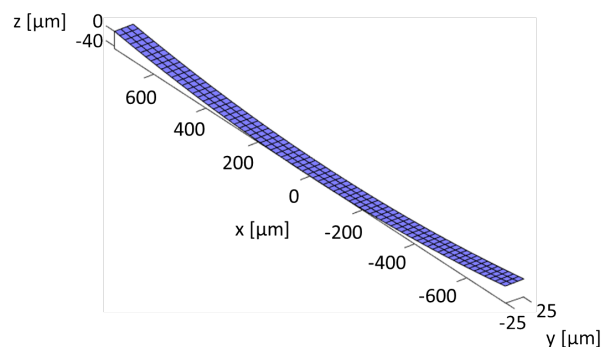
Figure 4.9: Simulated transducer element surface Cylindrically focused element of the transducer array. For the simulation the element is divided into small, flat, rectangular sub surfaces (calculated with the Field II toolbox [103]).

The transducer array which is integrated into the system consists of 128 identical cylinderically focused rectangular shaped elements. A single element is 55 μm in height (along the y-axis) and 1.5 mm in width. The pitch of the transducer elements

(the distance between the center of two elements) is $70\,\mu m$. The surface shape of one element which is used for the calculation as well as the division into smaller patches, can be seen in Figure 4.9. However, the shape in the image does not correspond to the actual or physical shape of the elements. The piezo elements are flat and the focusing is done by a cylindrical lens on top of the array. By the different speed of sound inside the lens, the time of arrival of the signal on the detector surface is adjusted. For the calculation of the sensitivity field, the focusing of the lens of $5.9\,mm$ is translated into a curved element shape with the corresponding curvature radius.

The element shape shown in Figure 4.9 is used to calculate the sensitivity field at different frequencies. As an input signal a sinusoidal wave with a distinct frequency f_0 is used. The results for the frequencies $f_0 = 10, 20, 25, 30\,MHz$ can be seen in Figure 4.10. The Figure shows two different planes the sensitivity field. In all panels the detector element is positioned in the origin, which is located at the center of the upper frame of the FOV. The transducer z-axis corresponds to the vertical direction of the shown sensitivity field. A section of $15 \times 15\,mm$ of the sensitivity field is shown. The upper row shows unfocused direction of the element, the yz-plane $(x = 0)$. In the lower row the focused direction, the xz-plane $(y = 0)$, can be seen. In the focused direction only a small stripe along the yz-plane $(x = 0)$, or the axis of the transducer is covered by the sensitivity field. All signals which are originating from outside this small region around the plane will not be visible by the transducer. At the center frequency of $25\,MHz$ the focal spot, i.e., the region with the highest intensity, is at $5.9\,mm$ distance. As expected, the width and the length of the focal area will vary for different frequencies as seen in equation 4.34 and 4.35. For lower frequencies the approximation $\lambda F/r^2 \ll 1$ which is used to calculate the focal width and length is not valid any more (see section 4.5.1. As seen in Figure 4.10, the focusing is not efficient for low frequencies.

In the other, unfocused direction the sensitivity field of the element has a large acceptance angle due to the small size of the element. Equation 4.33 describes the relation between the opening angle θ, the element size r, and the frequency f (or wavelength λ) of the signal. As seen in Figure 4.10 the acceptance angle θ increases for lower frequencies f.
Furthermore, an interference pattern can be observed in all sensitivity fields. These patterns have two origins. The more dominant oscillations are inherent to the used excitation frequency. In the unfocused direction (upper row/yz-plane) these oscillations appear as circles around the transducer element. In the focused direction (lower row/xz-plane) the excitation frequency will cause sidelobes (as seen in the sensitivity field for $10\,MHz$) and distinct pattern in the near field, the area between the transducer element and the focus.

The second type of interference patterns is caused by the sampling frequency which is used in the simulation. These pattern can mostly be seen in the unfocused direction (upper row) and are located along lines originating at the transducer element. The angle of these lines is independent of the excitation frequency.
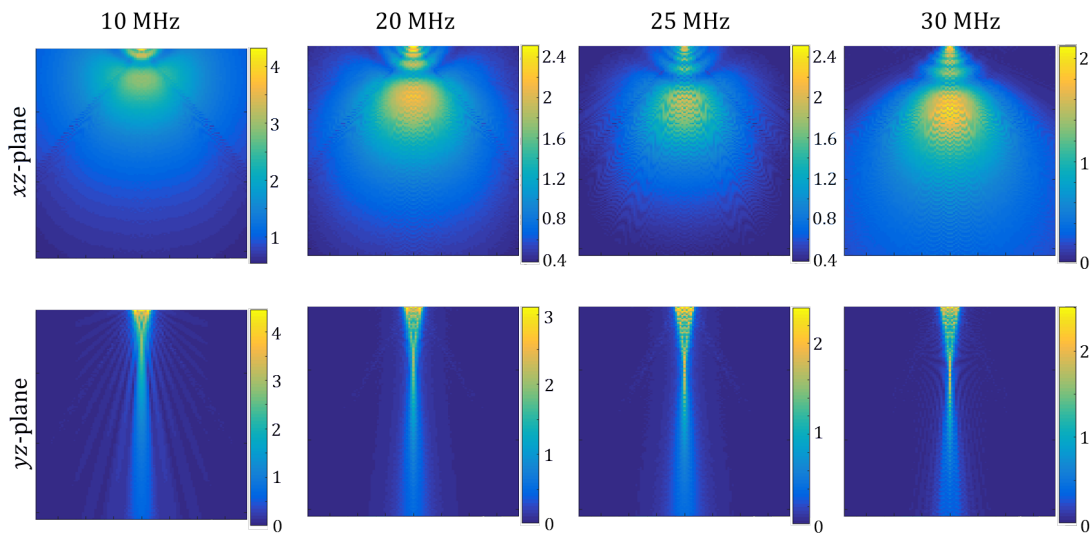
Figure 4.10: Simulated sensitivity field Sensitivity field of one cylindrical focused detector element from the transducer array. In the top row the unfocused direction of the transducer, the yz-plane is shown. In the bottom row the focused direction of the transducer, the xz-plane is depicted. In the unfocused direction the aperture angle decreases with frequency. The colorbar shows the intensity in arbitrary units

The interference pattern in the calculated sensitivity field can be avoided when broadband signal is used for the simulation instead of a narrowband signal. In Figure 4.11 a sensitivity field for a broadband excitation pulse is shown. The bandwidth of the used pulse corresponds to the bandwidth of the transducer. While the low frequency oscillations mostly disappeared, the high frequency oscillations due to the chosen sampling frequency remain in the simulated sensitivity field.
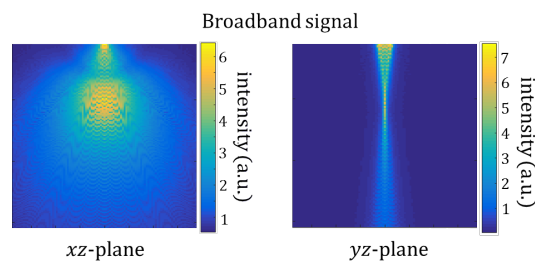
Figure 4.11: Simulated broadband sensitivity field The sensitivity field is simulated using a broadband pulse with the bandwidth of the real ultrasound transducer. On the left the yz-plane and on the right the xz-plane is shown.

Before the simulated sensitivity field will be used to improve the reconstruction quality, the results from the simulation will be validated with experimental measurements.

4.5.4 Experimental validation of the sensitivity field

To validate the simulated sensitivity fields, the sensitivity field of the central transducer element was measured. Similar to the measurement of the EIR, a 10 μm bead was used as a point-like broadband emitter. Again the fact is used that the image formation under the SIR is a linear process and the measured signal can be seen as a convolution between the original pressure distribution and the SIR [97]. By using a point like delta source the SIR can be measured. To calculate the sensitivity field only the absolute signal amplitude of the signal is extracted.

The measurement was performed in the same scanning system as the measurement of the EIR. To generate a sufficiently strong signal an 80 mJ NIR laser was used. The pulse width of the used laser is 8 ns and the wavelength was tuned to 800 nm. The bead was embedded in an agarose cylinder and both the sample and the transducer were submerged in water. Scanning and positioning of the transducer were performed by three motorized stages. Even with the high energy of 80 mJ averaging was necessary to get a sufficient SNR of around 16 dB at the center of the focus with 50 averages per position. Only the xz-plane in front of the central element was sampled. The result can be seen in Figure 4.12
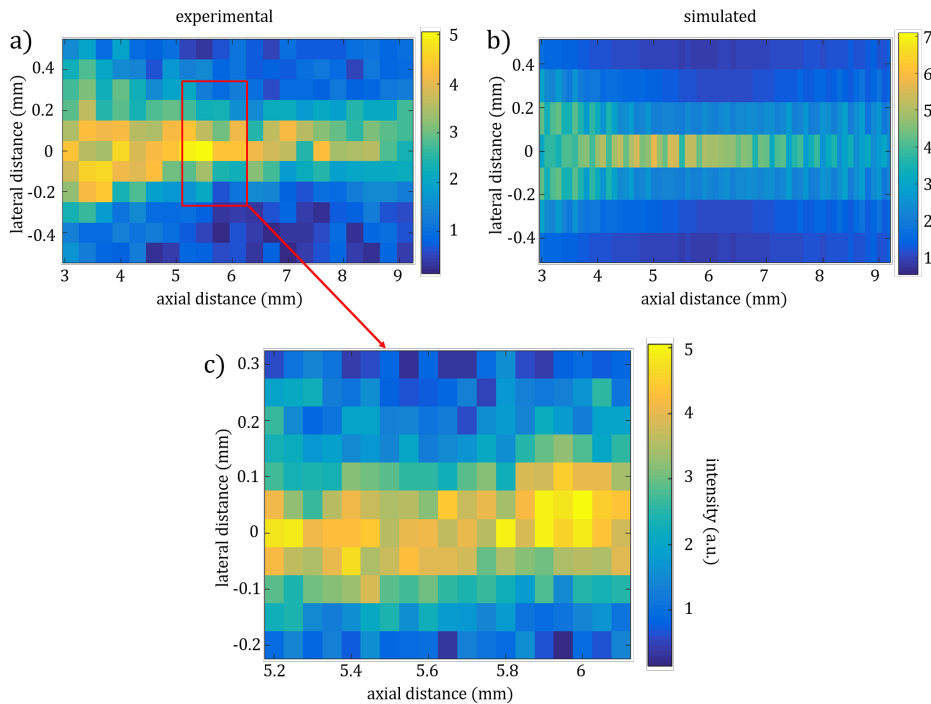
Figure 4.12: Measured sensitivity field a) measured sensitivity field in the yz-plane b) comparison to the simulated sensitivity field with the same FOV. c) smaller step size measurement of the focal region of the transducer (also yz-plane).

Two scans of the sensitivity field were performed: A large scan with a step size of 0.1 mm in the lateral direction and 0.3 mm in the axial direction was performed to cover the overall shape of the sensitivity field and determine the position of the focal

region (Figure 4.12a). Then the focal region was scanned with a smaller step size to acquire a more detailed sensitivity map and the exact focal position (Figure 4.12a) The signal from the focal spot was used to determine the EIR in the previous section.

Next to the measured sensitivity field with the large FOV, the simulated sensitivity field is shown in Figure 4.12. The same simulated sensitivity field can also be found in Figure 4.11. As shown in section 4.1.3, the frequency spectrum of a sphere of $25\,\mu m$ or smaller (as it is the case for the used $10\,\mu m$ sphere) is expected to have a center frequency significantly above the bandwidth of the transducer. The measured frequency spectrum can be assumed to be mainly dependent on the bandwidth of the transducer and not on the spectrum of the used bead. Therefore, the sensitivity field was simulated using a broad band pulse with the bandwidth of the transducer.

As seen in Figure 4.12 the measurement and the simulation of the sensitivity field are in good agreement. Both sensitivity fields show a similar shape and focal position. The derivations which can be seen between Figure 4.12a) and b) are mainly due to the poor SNR of the measured sensitivity field. The small oscillations due to the sampling frequency, which are visible in the simulated sensitivity field in Figure 4.12b, can not be expected to be seen at the chosen the sampling step size of the experimental measurement. Even for measurements with better spatial sampling, the SNR is too poor to image small oscillations of the sensitivity field in the focal region, as seen in Figure 4.12c.

Because of the confirmed shape of the simulated sensitivity field, the results from the simulation will be used to correct for the sensitivity field in section 4.8.

4.6 Spatial resolution of the two scanning geometries

Similar to most other imaging modalities, the spatial resolution is an important parameter in optoacoustic imaging. The resolution of the imaging system will determine which structures and details can be imaged.

4.6.1 Theoretical resolution

There are three main factors which define the resolution of an optoacoustic system: the pulse width of the laser, the bandwidth of the detector, and the aperture (or size) of the detector. Here a sufficiently short laser pulse will be assumed (see section 4.1.1). In this case the resolution only depends on the transducer properties. The following estimations for the PSF are taken from [85], where also a more detailed derivation can be found.

Bandwidth or EIR limited resolution

First, the impact of the bandwidth and therefore the EIR on the resolution will be considered. The calculation of the PSF follows a similar principle like the calculation

of the EIR H_i in section 4.4. A circular detection geometry (depicted in Figure 4.3) and a point source $p_0(\vec{r}) = \delta(\vec{r} - \vec{r_a})$ at the position r_a will be assumed. The (Fourier transformed) pressure $\tilde{p}(\vec{r_0}, k)$ at the position r_0 at the detection surface S is given by equation 4.20. However, the signal which is acquired by the detector will differ from the actual pressure field due to the finite bandwidth of the detector. The frequency characteristics of a detector are characterized by the EIR (in the time domain) or the frequency response. The frequency response can be assumed to be a band-pass function $\tilde{H}_i(k)$. Thus, the measured signal at position $\vec{r_0}$ can be written as $\tilde{p}'(\vec{r_0}, k) = \tilde{H}_i(k)\tilde{p}(\vec{r_0}, k)$. By replacing the $\tilde{p}(\vec{r_0}, k)$ with $\tilde{p}'(\vec{r_0}, k)$ in the reconstruction formulas in section 4.2, a theoretical bandwidth limited PSF$^{(b)}$ and therefore the frequency dependent resolution of the system can be determined:

$$\text{PSF}^{(b)}(R) = \frac{1}{2\pi^2} \int\limits_0^\infty \tilde{H}_i(k) j_0(kR) k^2 \, \mathrm{d}k, \tag{4.38}$$

where $R = |\vec{r_a} - \vec{r}|$ is the distance between the point $\vec{r_a}$ of the source and an arbitrary point $\vec{r}$, and j_0 is the Bessel function of the first kind.
If $\tilde{H}_i(k)$ is even (axisymmetric in the Fourier space) and real, and a cut-off frequency k_c of the function $\tilde{H}_i(k)$ with $\tilde{H}_i(k) = 1$ for $k < k_c$ and 0 else is assumed, the integral in equation 4.38 can be solved. After normalization the following formula is found for the PSF$^{(b)}$:

$$\text{PSF}^{(b)}(R) = \frac{3j_1(k_c R)}{k_c R}. \tag{4.39}$$

A common definition for the spatial resolution of a system is the FWHM of the PSF. Solving $3j_1(x)/x = 0.5$ for x and inserting it into 4.39 gives

$$R_H = 2 \cdot \frac{2.4983}{k_c} \approx 0.8 \cdot \frac{c}{f_c}. \tag{4.40}$$

Here f_c is the cut-off frequency and c the speed of sound ($k_c = f_c/c$). For the used detector array with a (-6dB) bandwidth going up to approximately 30 MHz a theoretical resolution of 40 µm can be calculated. However, as seen in Figure 4.5, frequencies beyond 30 MHz can be detected (with a lower signal strength). Therefore, the detector will be able to record signals higher than the (-6dB) bandwidth limit, which will result in a slightly higher resolution.

Aperture or SIR limited resolution

Besides the EIR, the SIR will alter the detected signal. Similar to the calculation of the bandwidth-limited PSF$^{(b)}$, the signal $p_0'(\vec{r_a})$ measured by the transducer does not necessarily correspond to the pressure signal $p_0(\vec{r_a})$, depending on the shape

of the detector and the origin of the acoustic signal. The signal acquired by the detector can be seen as an integral over the surface of the detector (see equation 4.36 and 4.37). The aperture limited $\mathrm{PSF}^{(a)}$ can be calculated, by inserting the new $p'_0(\vec{r_a})$ into the analytic reconstruction formula. To demonstrate the effect of the aperture and detector size, a flat and round detector with the radius P will be assumed and the detector will be translated along a line. In this case the calculation of the $\mathrm{PSF}^{(a)}$ yields

$$\mathrm{PSF}^{(a)}(\vec{r_a},\vec{r}) = U(P - D)\delta(\Delta z). \tag{4.41}$$

Here $\vec{r}(x,y,z)$ is an arbitrary point and $D = \sqrt{(\Delta x)^2 + (\Delta y)^2}$ is the lateral distance to the source (with $\Delta x = x - x_a$). As seen in equation 4.41, the PSF does not extend in the axial direction in case the EIR is neglected. The resolution R_L is simply given by the diameter D_d of the detector:

$$R_L \approx D_d. \tag{4.42}$$

The geometry discussed here corresponds to the vertical axis of the transducer array. In this direction the elements are unfocused and aligned along a line.

Combined resolution

In the system a combined bandwidth and SIR limited resolution will be found. The setup in this thesis uses a cylinderically focused transducer array (see chapter 2.1.3). The effect of the SIR on the signal will be negligible in the focal region of the transducer. Therefore, the combined rotation and translation of the transducer array will provide a homogeneous resolution R_H in the axial/horizontal plane, which is mainly limited by the bandwidth of the transducer. In the presented system the horizontal plane is the xz-plane and the resolution at the center of the plane can be approximated with $40\,\mu\mathrm{m}$. In the vertical direction (along the y-axis) the resolution can be approximated as: $R^L = \sqrt{R_H^2 + R_L^2}$. With an element size of $55\,\mu\mathrm{m}$ the expected resolution along this axis should be in the range of $70\,\mu\mathrm{m}$.

4.6.2 Overview of the scanning geometries

Two different scanning geometries were implemented in the system (see chapter 2.1.3). Both geometries are schematically depicted in Figure 4.13. In both geometries the samples are illuminated with a broad, homogeneous beam from opposite sides. In the first scanning geometry the transducer is rotated by an angle α, as well as translated by a distance l for each angular position. Because of the narrow cylindrical focus of the transducer, a lateral scan is necessary to image the entire sample for a fixed angular position. The lateral scanning distance therefore has to be at least equal to the sample width. Since most samples will not be exactly
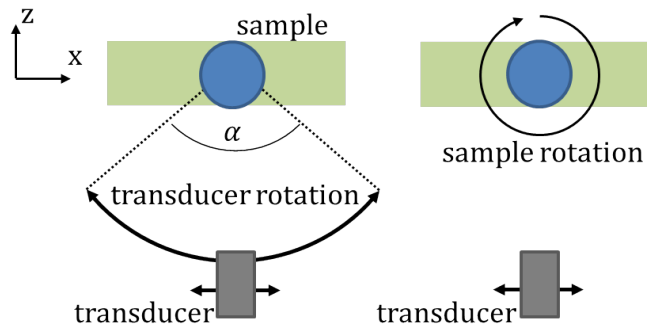
Figure 4.13: Scheme of the two scanning geometries Two different scanning geometries were implemented: In a) the transducer is both translated on rotated. In b) the transducer is only translated and the sample is rotated. The sample is illuminated from opposite sides.

positioned in the center of rotation, l is normally chosen to be larger than the sample width. The sample (and therefore also the light flux in the sample) are stationary in this geometry. Although the scanning geometry is referred to as a '90°-scan', the maximum angle α is typically below 90° since the transducer is also translated. For most samples the maximum angle is between $80° - 85°$ depending on the lateral translation l for each angular position.

In the second geometry the sample is rotated 360° and the transducer is only translated. Keeping the amount of angular positions fixed in both scans results in a similar scan time.

The theoretical resolution given in the previous section was calculated under the assumption of a circular scanning geometry. The missing angular cone in the 90°-scanning geometry is expected to cause an anisotropic resolution (or PSF) in the horizontal plane.

4.6.3 Measured resolution

To compare both scanning geometries and characterize the resolution, two phantoms were used. A single $20\,\mu$m bead is placed in the focus and measured in both geometries. 21 lateral scanning positions with a step size of $100\,\mu$m and 60 angular scanning positions were chosen. The angular scanning positions were distributed equally over the whole scanning range. For the 360° scan this results in an angular step size of 6° and for the 85° scan in an angular step size of approximately 1.5°. In Figure 4.14 the results of both scans are shown.
Panel 4.14a-c) depict the reconstruction for the 360°-scan. The horizontal plane (xz-plane) with the high, frequency dependent resolution is shown next to a vertical slice (yx-plane). In the vertical direction the resolution is additionally influenced by the NA or the size of the transducer in the vertical (unfocused) direction. The measured profile of the $20\,\mu$m is shown in panel 4.14c). While the resolution in the
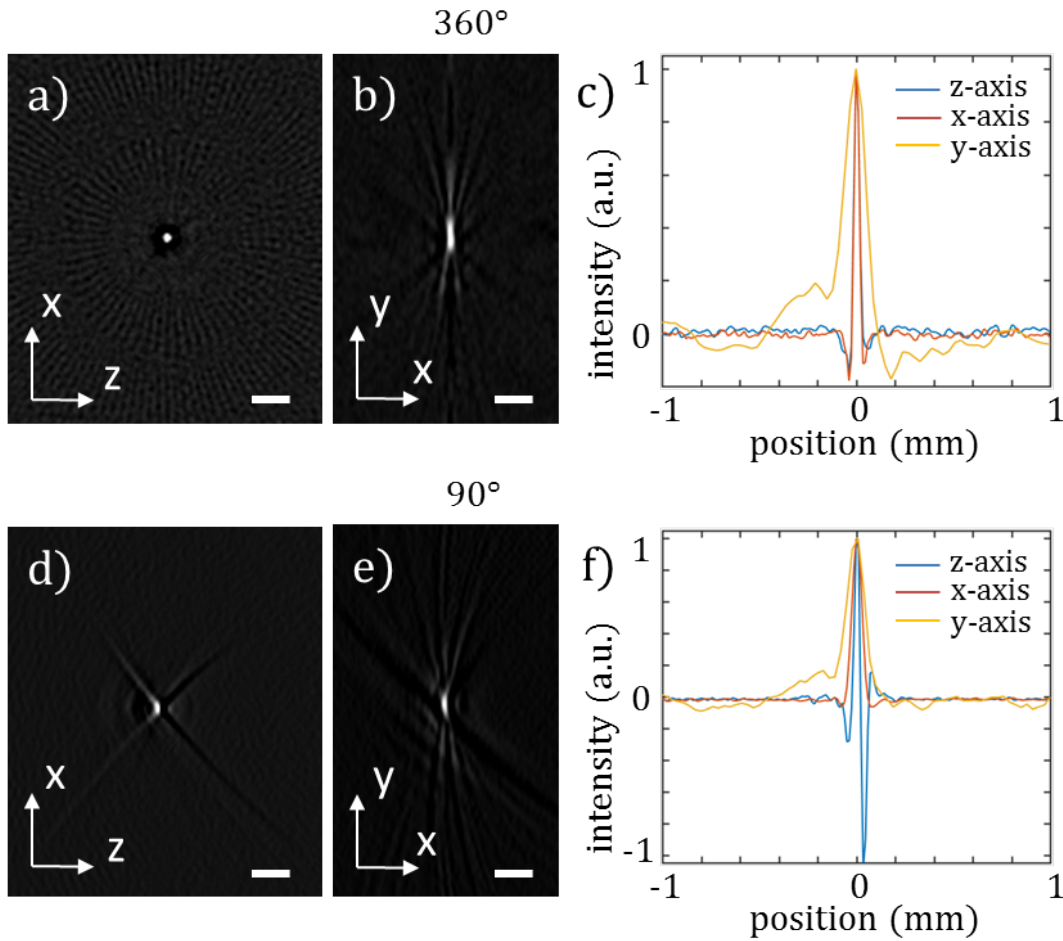
Figure 4.14: Optoacoustic resolution a)-c) results of the 360°-scan. a) isotropic shape of the single 20 μm in the xz-plane. b) ellipsoidal shape of the bead in the yx-plane. c) profile of the bead in all three directions. d)-f) results of the 90°-scan. d) anisotropic shape and artifacts in the xz-plane due to the missing angular cone. e) ellipsoidal shape of the bead in the yx-plane. f) profile of the bead in all three directions. scale bar indicates 200 μm

x and z-direction is isotropic and a FWHM of 35 μm is measured, the resolution in the y-direction shows a FWHM of 120 μm and is lower than the expected theoretical resolution. Furthermore, the measured profile is not completely symmetric. This is due to the fact, that the bead was not aligned at the middle of the FOV in front of the central element 64, but slightly shifted down in front of element 80.

Small negative values in the reconstructed image can be seen around the reconstructed sphere. These negative values are artifacts from the backprojection algorithm due to the finite number of projections and the cut-off of lower frequencies by the limited bandwidth of the transducer.

The reconstruction for the 90°-(or rather 85°) scan are shown in panels 4.14d-f). In contrast to the 360°-scan,0 the reconstruction of the bead in the horizontal xz-plane does not show an isotropic shape. Instead, the shape of the beads is elongated

and a cross-shaped artifact can be seen originating from the bead. In the vertical direction the effect on the shape is negligible. This can also be seen in panel 4.14f), where again the profile of the bead along the different axes is plotted. While the profile in the y-direction shows the same shape and the same FWHM of $120\,\mu$m as in the 360°-scan, the profile in the x and z direction deviate significantly. In the z-direction, strong negative artifacts can be observed. Taking only the positive peak into account a FWHM of $30\,\mu$m can be measured which is similar to the measure width of the 360°-scan. The negative artifact propagates along two lines, forming one half of the cross-shaped artifact. The other half of the cross artifact is formed by two positive line artifacts facing in the opposite directions. In the y-direction, the bead is smeared out and shows a FWHM of $70\,\mu$m, which is twice the size of the resolution achieved in the 360°-scan.

As expected the missing angular cone in the 90°-scanning geometry causes strong artifacts and an anisotropic resolution. This can also be observed in Figure 4.15. Here a suture cross of $20\,\mu$m sutures was measured in both scanning geometries.
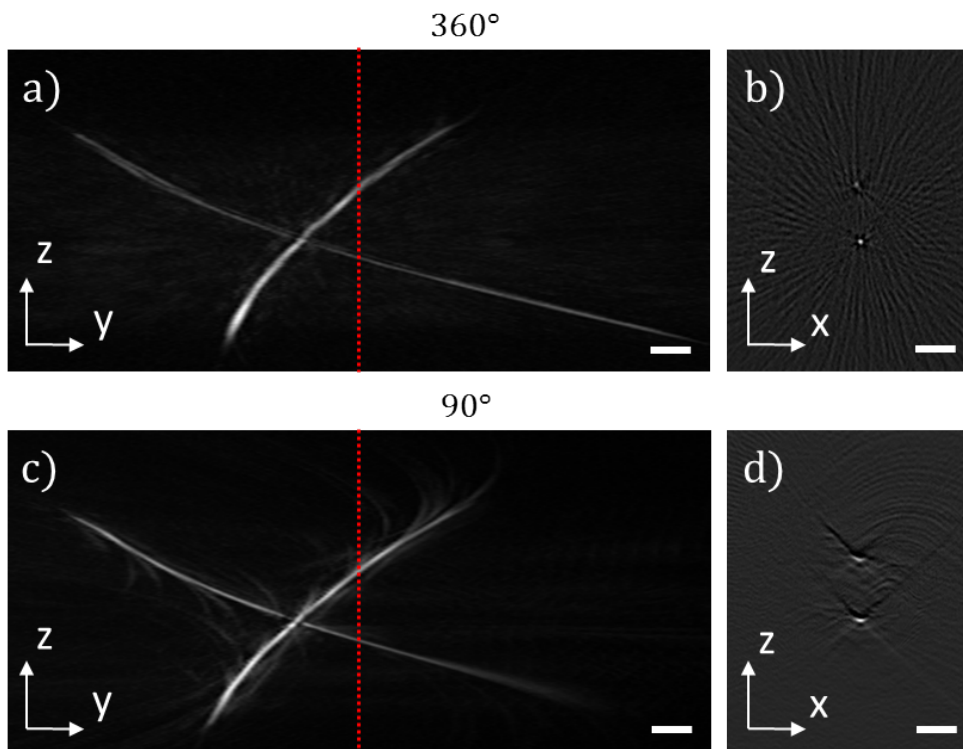
Figure 4.15: Missing angle artifacts Suture cross imaged with the 360° (a and b) and 90° (c and d)-scan geometry. a) and c) show a MIP along the x-direction. b) and d) show a zx-slice form the suture cross. The position of the slice is indicated by the dashed line in the MIPs. scale bar indicates $500\,\mu$m

In Figure 4.15a) and c) a MIP of the suture cross is shown. In the plane shown (zy) the width of the suture is similar. However, more artifacts can be see around the suture in the 90°-scan. Furthermore, the suture cross is better visible in the lower right part of the MIP. One possible reason for the decreased signal from the

suture can be its orientation. Since the optoacoustics signal is mainly emitted perpendicular to the suture and the suture is tilted, the signal from the suture will vary depending on the relative position to the transducer. The missing angle implicates a missing cone in frequency space. If a structure (or suture) is oriented in a way that the emitted frequencies lie completely within the missing cone in the frequency space, the structure can not be detected at all.

The anisotropic resolution for the 90°-scan can be observed in the image plane in Figure 4.15b) and d). The position of the image plane is indicated in the MIPs with a dotted line. Similar to the artifacts visible for the single bead in Figure 4.14, a cross artifact can be seen around both sutures. Furthermore, the cross section of the suture shows an ellipsoidal shape. The width of the suture for both scans is similar to the FWHM of the single bead. The 360°-scan shows an isotropic FWHM of around 35 μm, while the 90°-scan shows a width of 35 μm in the z-direction and 70 μm in the x-direction.

4.7 Comparison of both scanning geometries

To test impact of the two different scanning geometries on the image and reconstruction quality of a real biological sample, a 2.5 month old zebrafish was scanned in both geometries. In contrast to a suture sample where the orientation of the structures is predetermined, a great variety of structures with different orientations can be found in a biological sample. Therefore, it is expected that the amount of missing information in the 90°-scan is even larger than in the suture phantom in the previous section (see Figure 4.15).

Figure 4.16 shows the reconstruction of the 2.5 month old zebrafish, imaged with both scanning geometries. The number of angular and translational scanning position was kept constant for both scans. As already seen in the MIPs in Figure 4.16a) and d), not all structures are visible in the reconstruction of the 90°-scan. The disadvantage of the 90°-scan becomes even more evident, when the slices from the two regions of the 90°- and the 360°-scan are compared. Figure 4.16b) and c) show the reconstruction of two slices imaged in the 360°-geometry. Structures of all orientations are visible in the reconstruction. Most dominantly the pigmentation on the top and on the sides of the zebrafish can be seen. The pigmentation or melanin cells on the surface of the fish form a strongly absorbing structure and therefore generate strong optoacoustic contrast. In the 360°-scan the reconstructed structures show a symmetric pattern of both sides of the zebrafish as expected by the anatomy.
In contrast to this, the 90°-scan reconstruction shows a high dependency between the orientation of the structure and its visibility, as seen in Figure 4.16e) and f). The center of the 90°-scan was located at the upper left of the shown plane. Only structures which are (partly) perpendicular to the direction of the scanning center show a strong signal and are visible in the reconstruction. This effect can be observed at the pigmentation which covers the sides and the top of the zebrafish.
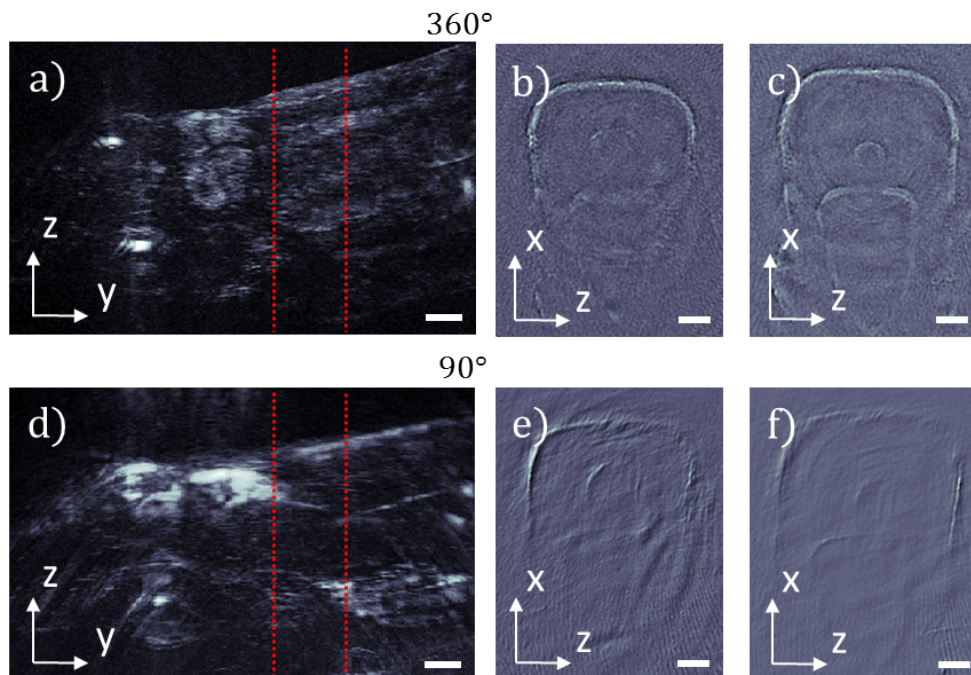
Figure 4.16: Comparison of both scanning geometries A 2.5 month old zebrafish was imaged. The upper roe shows the results of the 360° scan. In a) a MIP of the zebrafish is shown and two slices are marked for a more detailed comparison. b) shows the first slice located directly behind the head of the zebrafish. c) shows the second slice from the belly. In the lower row the results of the 90°-scan are depicted. Again a MIP is shown in d). e) and f) show the corresponding slices from the region behind the head and the belly. scale bar indicates $500\,\mu m$

While in the 360°-scan geometry the entire pigmentation can be seen, the 90°-scan shows only part of the pigmentation. The same holds for internal structures especially in the belly (Figure 4.16c and f).

The main reason for the limited visibility of structures is the directionality of the emitted signals. Structures which emit the optoacoustic signal perpendicular to the transducer axis cannot be detected by the transducer. Furthermore, the signal from the back of the zebrafish will be damped by absorbtion of optoacoustic wave within the sample. Therefore the side of the zebrafish closer to the detector will show a stronger signal.

The results form this section clearly show that the disadvantages of the 90°-scan outweigh the advantages of a constant illumination in the scanning geometry. In the 360°-scan the sample is rotated relative to the illumination, which might result in a change of light fluence for different detector positions. However, the reconstruction quality is significantly better and structures of all orientations can be detected. Because of the results from this section, the 360°-scan will be used for all further sample scans.

4.8 Advanced reconstruction

The knowledge about the characteristics of the transducer such as the EIR and the sensitivity field can be used to improve the reconstruction. In the following section the incorporation of the sensitivity field into the backprojection algorithm as well as the correction of the signal through the EIR will be discussed and evaluated on the basis of acquired biological data sets.

4.8.1 Weighted backprojection

For the standard backprojection algorithm, a point-like detector with a homogeneous sensitivity in all directions is assumed. In the reconstruction the signal from all directions will overlap at one point. The basic principle of the standard backprojection algorithm was derived in section 4.2.
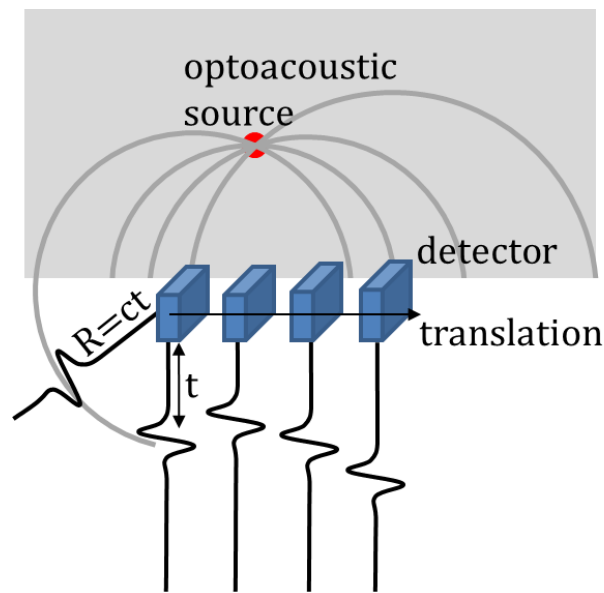
Figure 4.17: Backprojection scheme In standard backprojection, the derivative of the recorded signal is backprojected onto a sphere with the radius $R = ct$, where c is the speed of sound and t the point in time of the signal. Signals form the same source recorded at different detector positions overlap at the location of the source. (see [84])

In Figure 4.17 the basic scheme for a planar geometry is depicted. This geometry corresponds to the lateral scanning of the transducer array. The signal, or rather the derivative of the signal, recorded at point t in time is backprojected onto a sphere with radius $R = ct$, where c is the speed of sound.

However, in an actual optoacoustic setup, the measured signal will highly depend on the sensitivity field and the orientation of the transducer. While the transducer will be able to record a strong signal if the absorber is in the focus, the signal will decrease the farther the absorber is located away form the focus until the

signal from the absorber will not be recognized by the transducer at all. The signal acquisition for a focused transducer is illustrated in Figure 4.18a.
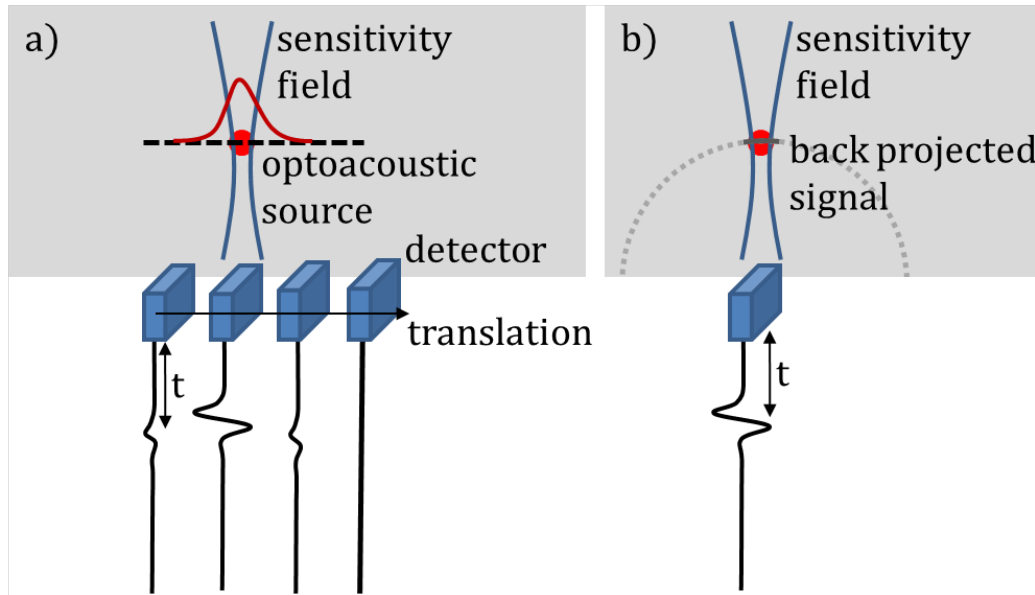
Figure 4.18: Weighted backprojection scheme a) The optoacoustic signal will only be detected the focused transducer is facing the optoacoustic source. When translated further away, no signal will be detected. b) The acquired signal is not backprojected on to a sphere, but only the region covered by the sensitivity field of the transducer.

The sensitivity of the detector is limited to a narrow focal zone with the highest sensitivity at the center. If the detector is laterally translated, the recorded signal from the optoacoustic source will get weaker and, at some point, not be detected by the transducer anymore.

There are two approaches to incorporate the sensitivity field into the reconstruction and to increase the image quality. One possibility is to correct for the drop in sensitivity by enhancing the weak signal coming outside of the focal region. However, since noise is present in the acquired signal, enhancing weak signal will also amplify noise.

A second approach is to restrict the region to which the signal is backprojected. Instead of backprojecting the signal on a sphere (or a circle in 2D) the signal is multipled by the sensitivity field. In this way the signal will get backprojected only to such regions the signal most likely originated from. Especially if the number of projections is low, or the optoacoustic source can only be detected in a small proportion of the detector positions, this approach should be beneficial.

The ideal backprojection assumes an infinite amount of detector positions. The signal from a single source will overlap in one point and cancel out everywhere

else. In case of only a few scanning position, as it is depicted in Figure 4.17, the backprojected signal forms spheres around the detector positions which will be be clearly visible in the reconstruction. By restricting the backprojected signal to the focal region of the transducer these ring artifacts can be avoided.

Even when several detector positions are acquired, this approach can be useful. Elongated optoacoustic sources will create a directional signal depending on the orientation of the structure effectively lowering the number of transducer positions which can detect the source. Furthermore, absorption of the emitted optoacoustic waves within large samples might block signals originating from the opposite side of the sample (seen from the transducer). Therefore, an optoacoustic source within a larger sample can often be detected only from a limited number of detector positions. Again a limited number of projections will lead to ring artifacts, which can be avoided by the weighted backprojection.

The approach of weighting the backprojected signal is therefore expected to increase the image quality for large samples or in case of a limited number of views/detector positions. This assumption is tested on large biological samples in section 4.8.2.

Frequency dependent weighted backprojection

Until now, one universal sensitivity field was assumed. For transducers with a narrow bandwidth this is a valid approximation. In the case of a narrow bandwidth, the sensitivity field of the center frequency or the sensitivity field of a pulse with the transducer bandwidth can be used (see Figure 4.11). However, for detectors with a broad bandwidth, the sensitivity field will look differently depending on the frequency of the optoacoustic source. This can be seen in the simulation results in Figure 4.10 in section 4.5.3, where the sensitivity field is plotted for different frequencies.

To account for the frequency dependency, an approach similar to the (Gabor-) window reconstruction in chapter 3.2.6 is used. The recorded signal is transformed to the Fourier space and multiplied by overlapping window functions (an example for the overlapping window functions can be found in Figure 4.22a). By multiplication with the window functions, multiple frequency bands of the signal are acquired. Each frequency band is transformed back into the time domain and reconstructed independently. The sensitivity field used in the weighted backprojection corresponds to the sensitivity field of a pulse with the respective bandwidth of the window.

To gain a final reconstruction, all independent reconstructions are summed up. This reconstruction method also allows to weight the reconstructed frequency bands with adapted factors. High frequency signals are normally weaker than the lower frequency signal and can be enhanced. Furthermore, the division into the frequency band allows to differentiate between structures of different size.

4.8.2 Experimental results for the weighted backprojection

First, the simple weighted backprojection, using only one sensitivity field (of a pulse with the transducer bandwidth), will be analyzed. Afterwards, the simple weighted backprojection will be compared to the frequency dependent weighted backprojection on the basis of the reconstruction of a biological sample.

The weighted backprojection is expected to improve the reconstruction in the case the signal from an optoacoustic source is only visible in a limited number of detector positions. In a more ideal case of several projection from all sides of the sample, the dampening of signals from the outer regions of the focus will reduce the given amount of information and effectively lower the NA of the transducer. Since the resolution of a transducer element is proportional to the NA of the element, the weighted backprojection might negatively affect the reconstruction.
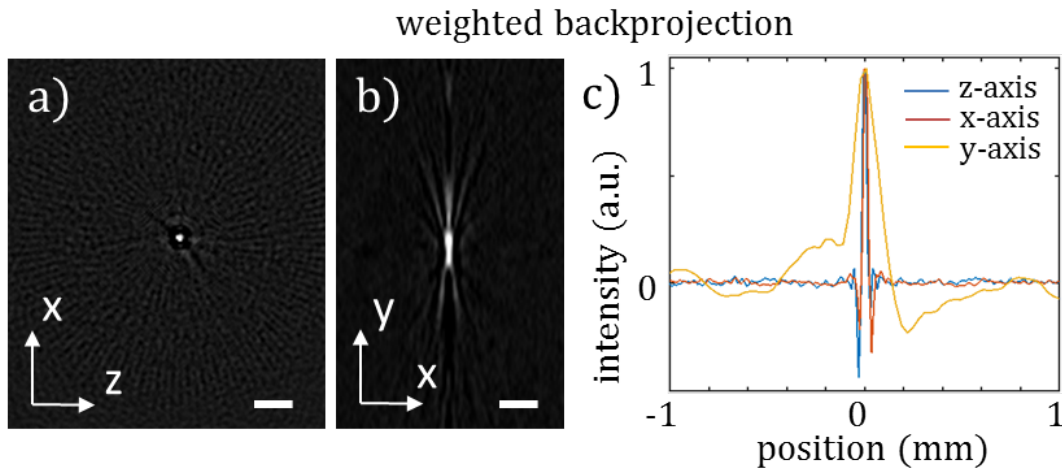
Figure 4.19: Resolution of the weighted backprojection a) isotropic shape of the single 20 μm in the xz-plane. b) ellipsoidal shape of the bead in the yx-plane. c) profile of the bead in all three directions. scale bar indicates 200 μm

This assumption is tested with a 20 μm bead. The same bead was previously used to determine the resolution of the optoacoustic setup. The reconstruction result for the weighted backprojection can be seen in Figure 4.19. The reconstruction in the horizontal xz-plane (panel a) and in the vertical xy-plane look similar to the results of the normal backprojection. Only when the profile of the bead (see Figure 4.19) is analyzed, differences to the standard backprojection can be found. Because of the decreased signal strength for signals originating from the outer regions of the focal area (where the sensitivity has already dropped but the signal is still visible), the negative values at the edge of the bead are enhanced. Furthermore, the absolute reconstructed intensity of the bead is lower than for the standard backprojection. However, the bead size and therefore the resolution in the xz-plane remains unchanged at 35 μm. Along the vertical y-axis, the same effect of increased negative values can be observed. Additionally, the FWHM of the bead increases to

145 μm. The deterioration of the resolution in the vertical direction confirms the assumption, that the weighted backprojection is effectively lowering the NA of the transducer.
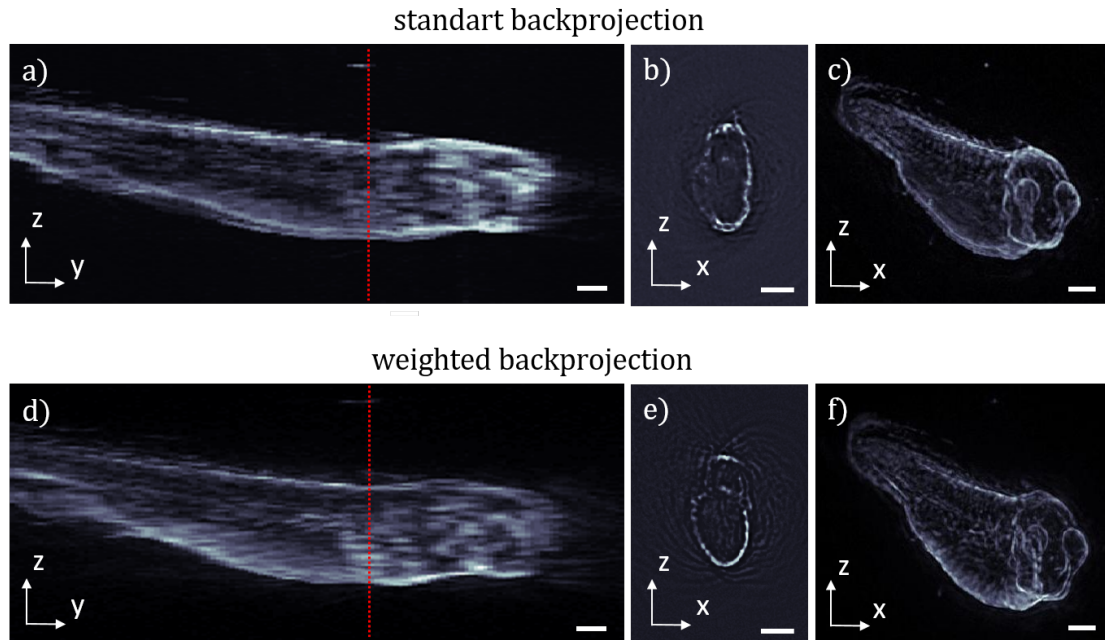
Figure 4.20: Xenopus larvae backprojection comparision a)-c) show the results for the standard backprojection. d)-f) show the results for the weighted backprojection. b) and e) show a slice from the xenopus larvae, while the other panels show MIPs. scale bar indicates 200 μm

Since the standard backprojection gives better results for the 'ideal' case of a single bead which is visible from all directions and emits an isotropic acoustic signal in all directions, the weighted backprojection was tested on a small biological sample. In this case a 2 day old *Xenopus*[1] larvae is used to create conditions similar to the case of a small absorber visible form all sides. The results are shown in Figure 4.20.

In the upper row of Figure 4.20 the reconstruction with the standard backprojection is shown, in the lower row the reconstruction results for the weighted backprojection. In the MIP in Figure 4.20a) a generally higher intensity from the head of the *Xenopus* larvae can be observed, compared to the weighted reconstruction in panel d). The same effect is visible in the MIPs in panel c) and f). In Figure 4.20b) and e) a single slice from the reconstruction volume is shown.

The shown results indicate that because of the weighted backprojection lower spatial frequencies get suppressed. As shown in section 4.5, the NA and the focal size of the transducer is larger for lower ultrasound frequencies. These lower ultrasound frequencies also translate into structures of lower spatial frequency. By decreas-

---

1 Similar to the zebrafish the *Xenopus* (larvae) is a commonly used model organism

ing the signal from regions outside the focal point, as it is done by the weighted backprojection, lower frequencies get suppressed. A second effect is the influence of the SIR on the signal. The SIR will alter the shape of signals outside the focal region, normally causing a shift in the frequency spectrum of the signal towards lower frequencies. By decreasing the signal from sources outside of the focus, the effect on the reconstruction of these signals is reduced.
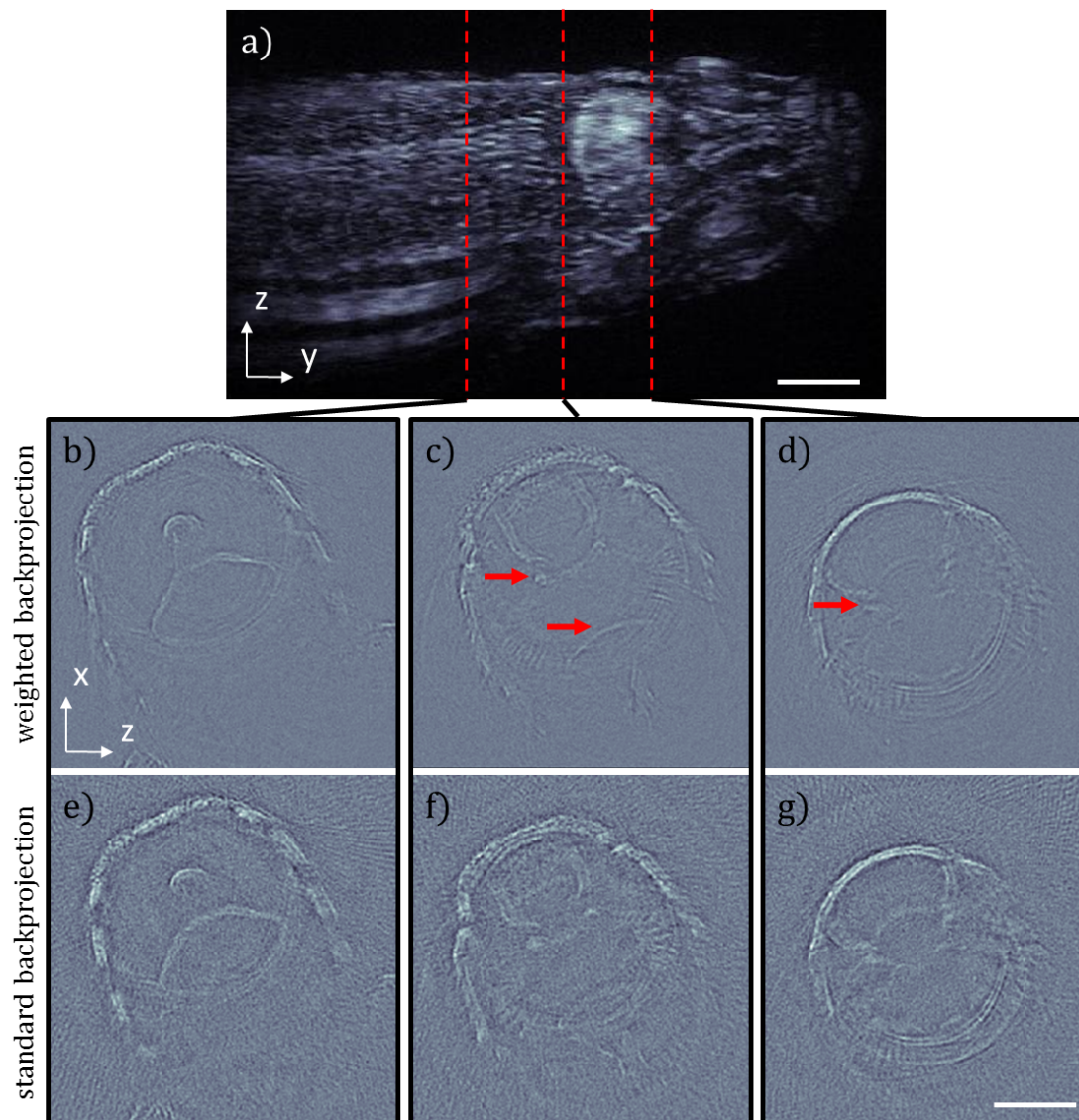
Figure 4.21: Adult zebrafish backprojection comparision A 2 month old zebrafish was reconstructed with the standard and the weighted backprojection algorithm. a) MIP of the zebrafish along the x-direction (weighted backprojection). Three slices of the zebrafish are chosen and shown below. The location of each slice is indicated with a dotted line. The first row b)-d) show the results for the weighted backprojection, the lower row e)-g) the results for the standard backprojection. The red arrows mark regions where improvements of the reconstruction is clearly visible. scale bar indicates 1 mm

To show the advantage of the weighted backprojection over the standard backprojection for larger samples, a two month old zebrafish was chosen. The results of both reconstruction algorithms can be seen in Figure 4.21. Panel a) shows a MIP of the weighted backprojection reconstruction. Three slices from the reconstruction volume are picked to demonstrate the effect of the weighted backprojection on the reconstructed results. The location of the three slices is indicated with a dashed line. In the first row, panel b)-d), the results for the weighted backprojection are shown, in the second row, panel e)-g), the results for the standard backprojection are shown. Two effects are visible in the reconstructed slices. The structures are sharper in the weighted backprojection and reconstruction artifacts are significantly reduced.

The suppression of reconstruction artifacts is linked to the finite number of detector positions. In the case of the ideal backprojection, an infinite number of projections is assumed. All signals are projected into the reconstruction space on spheres with the origin at the respective detector position. The signals will cancel out everywhere except at the position of the optoacoustic source, where all signal spheres overlap. When the number of projections is finite, ring artifacts will be visible in the outer regions of the reconstruction volume. If the signal is not visible from all direction or angles, similar artifacts will appear. By limiting the region to which the signal is backprojected, as it is done in the weighted backprojection, these reconstruction artifacts can be minimized.

The results in Figure 4.21 show that the reconstruction quality for larger samples can be significantly improved through the weighted backprojection.

Frequency dependent weighted backprojection

The previous results were acquired with a frequency independent weighted backprojection. Generally the sensitivity field is frequency dependent. Therefore, a frequency dependent weighted backprojection was implemented and tested on a 25 day old juvenile zebrafish. The sample size is between the *Xenopus* larvae and the 2 month old adult zebrafish shown in the previous section. The smaller size of the sample compared to the adult zebrafish reduces the advantage of the weighted backprojection over the standard backprojection and makes the problems mentioned for small samples more prominent. All acquired signals were divided into three frequency bands. Figure 4.22a) shows the three window function (red) and the frequency spectrum of complete measurement (blue). All signals were filtered with a 2-40 MHz bandpass filter and the spectrum was averaged over all 2100 detector positions and the 128 elements of the array. The frequency content above 35 MHzis low, and therefore not shown in the plot. However, for the reconstructions, the full spectrum was used.

Figure 4.22b)-d) show the MIPs of the three reconstructed frequency bands from 0-12 MHz, 12-18 MHz and 18-40 MHz, respectively. In panel b) only the larger melanin structures on the surface of the zebrafish and the heart, as a large internal structure, are visible. Panel c) already reveals several smaller structures. Most of
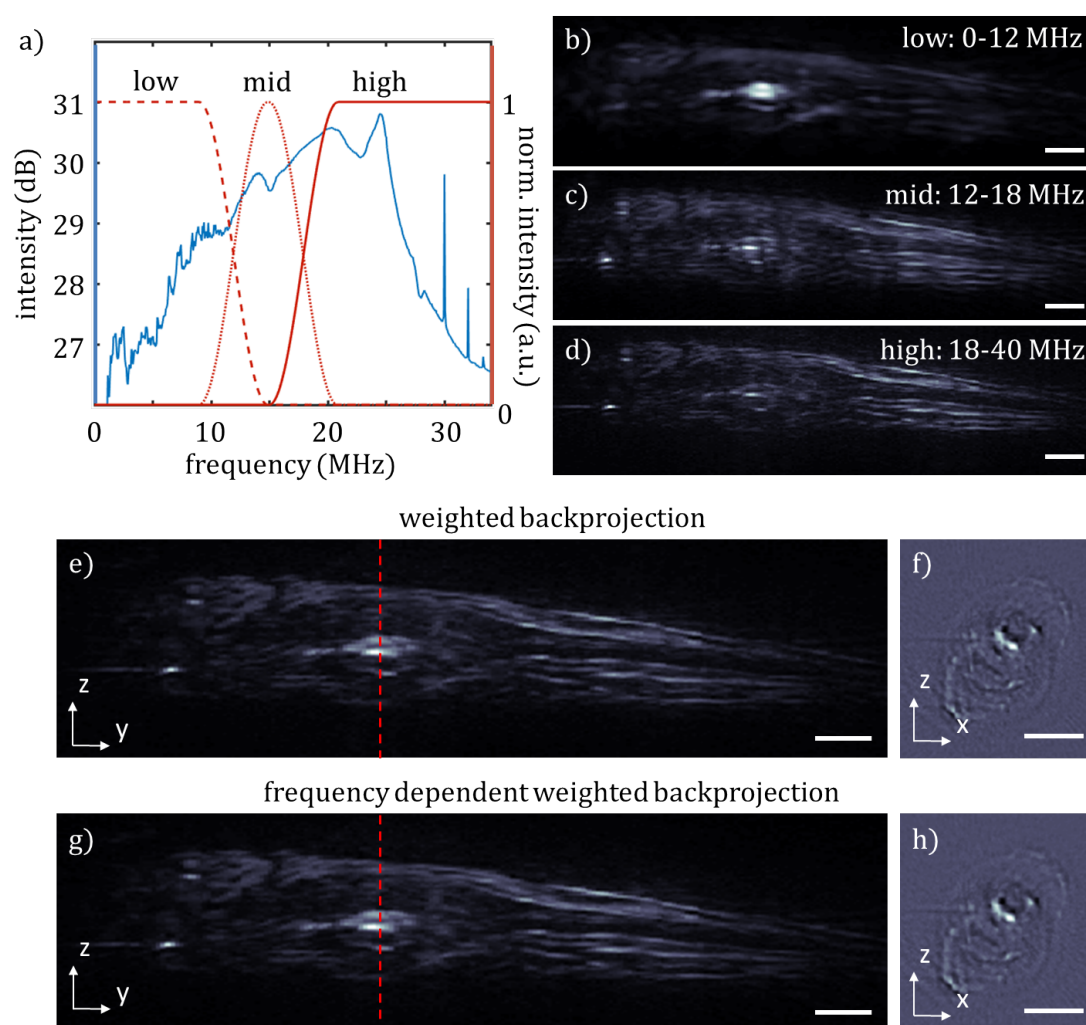
Figure 4.22: Frequency dependent weighted backprojectio 25 day old zebrafish reconstructed with the frequency dependent and the frequency independent weighted backprojection. a) averaged frequency spectrum of all acquired signal and the used window functions. b)-d) MIP of the reconstructed sample for the three frequency bands. e) MIP reconstructed with the frequency independent weighted backprojection. f) slice from the reconstruction volume shown in e). g) MIP of the summed frequency dependent weighted backprojections of all three frequency bands and f) slice from the respective reconstruction volume. scale bar indicates 500 μm

these structures are also visible in panel d), indicating that the frequency spectrum of theses small structures spans over both reconstructed frequency bands.

In Figure 4.22e)-h) the results of the frequency dependent and the frequency independent backprojection are compared. In each case a MIP and a slice of the reconstructed volume are depicted (the *y*-position of the slice is indicated with the dotted line).

The differences between both reconstructions are insignificant. This result suggests

that the sensitivity field for the used transducer can be approximated to be frequency independent. In the presented case the only advantage of the frequency dependent reconstruction is the separation of structures of different size (as seen in Figure 4.22b-d) and the possibility to adapt the intensity scaling factor between the different frequencies. However, the total reconstruction time will multiply with the number of frequency bands, slowing down the reconstruction significantly.

4.8.3 EIR deconvolution

The signal formation process due to the EIR is a linear process. The acquired signal $p'(\vec{r}_0)$ can be described as a convolution of the actual pressure field $p'(\vec{r}_0)$ at point r_0 and the EIR H (see equation 4.29). There are multiple (iterative) methods to deconvolve a signal. One of them is presented in chapter 3. In this case an existing Matlab deconvolution function `deconv` will be used. The simple deconvolution algorithms comes without further priors and is already runtime optimized. Each recorded signal is deconvolved with the EIR calculated in section 4.4. The corrected signal is then reconstructed by the back projection algorithm. The results of the EIR correction in conjunction with the weighted backprojection can be found in the next section[1].

4.8.4 Experimental results for the EIR deconvolution

Figure 4.23 shows the reconstruction of a 2 month old zebrafish. The reconstruction was performed with the weighted backprojection algorithm presented in the previous section. Two slices are picked for the zebrafish (indicated by dashed lines in the MIP in Figure 4.23a) and depicted in the panels b)-e).

The EIR corrected reconstruction in the first column (b and d) show an improved contrast to the uncorrected images. Structural details visible in panel b) are improved compared to the reconstruction in panel c) (indicated by the red arrows). However, in most cases the EIR correction showed little impact on the image quality.

To improve the EIR correction, a better and more precise measurement of the EIR is necessary. The signal which was used in section 4.4 to calculate the EIR (see Figure 4.5) shows a poor SNR due to the weak signal from the bead and the low sensitivity from the transducer array. To improve the signal, significantly higher laser energies per area and more averages are necessary. Alternatively, different methods can be used to determine the EIR [80, 97]. Through focusing of a laser pulse on a thin layer of absorbing (black) varnish a strong optoacoustic source with a large bandwidth can be created. Because of the focusing of light, much stronger optoacoustic signals can be generated compared to a broad illumination. Another possible way of improving the EIR correction could be achieved by correcting each transducer element individually. The EIR for all elements will be slightly different

---

1   The results of the EIR deconvolution were acquired together with Paul Vetschera
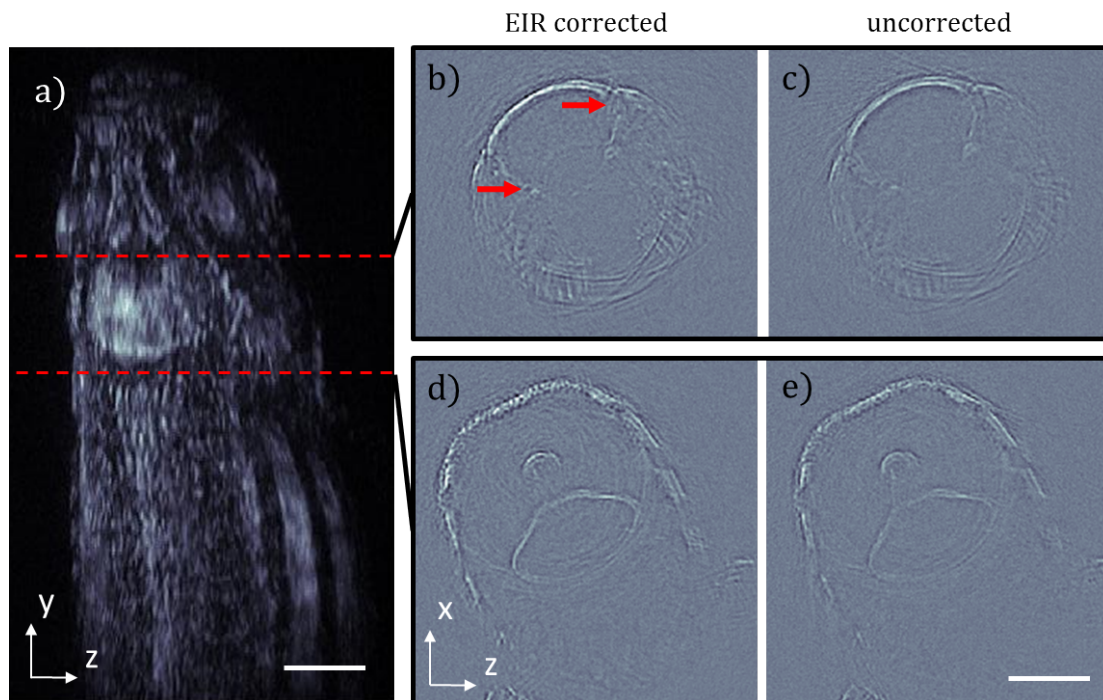
Figure 4.23: Adult zebrafish EIR correction A 2 month old zebrafish was reconstructed with and without EIR correction. a) MIP of the zebrafish along the x-direction (weighted backprojection). Two slices of the zebrafish are chosen and shown in the panels b)-e). The location of each slice is indicated with a dotted line. The first column b) and d) show the results for the EIR corrected reconstruction, the second column c) and e) the results for the uncorrected reconstruction. The red arrows mark regions where improvements of the reconstruction is clearly visible. scale bar indicates 1 mm

and therefore an independent measurement and correction of the EIR for each of the 128 elements could be beneficial.

5 Hybrid imaging results and discussion

Most studies of developing model organisms are confined to the embryonic stage of development. However, not all biological questions can be answered during this early stage, since morphogenesis continues until adulthood, and expression patterns of genes, such as those encoding hormones, change with age. The motivation for developing and implementing the hybrid SPIM and optoacoustic mesoscopy system - as well as the implementation of novel reconstruction algorithms - was to create a tool which is able to track developing model organisms over large scales, both in time and over a large range of sample sizes.

In the preceding chapters, we have introduced and characterized a scanning geometry for the hybrid system. On the algorithmic level, advanced reconstruction algorithms have been developed and implemented for both imaging modalities.

In the following the applicability of the presented system as a multi-scale hybrid imaging modality will be examined.

5.1 Hybrid imaging of zebrafish over 50 days of development

To demonstrate the abilities of the hybrid SPIM and optoacoustic mesoscopy system, a developmental study of zebrafish is performed. The genetic line Brn3c:GFP [104], which expresses GFP in hair cells, was tracked from early development to adulthood and imaged in time intervals of 7-9 days.

To avoid a loss in fluorescence of the GFP due to photo bleaching during the optoacoustic scan, the SPIM scan at 488 nm wavelength was performed first. The subsequent optoacoustic mesoscopy scan was performed at the same wavelength with the optoacoustic illumination. At 488 nm the laser light will heavily be absorbed by melanin and blood, generating a strong optoacoustic signal. Figure 5.1 shows a selection of different stages of development from the developmental study we performed, ranging from the larval stage (10 days) to adult stage (60 days)[1].

While abundant GFP signal (green) with the expected distribution is visible in larvae (Figure 5.1a and b), the signal is much weaker and poorly resolved in larger animals (Figure 5.1g and h). The loss in fluorescence and resolution has two reasons: firstly the larger sample size and secondly the more opaque tissue. Some of the

---

1   The results shown in this section are part of a paper in preparation and were measured together with Paul Vetschera
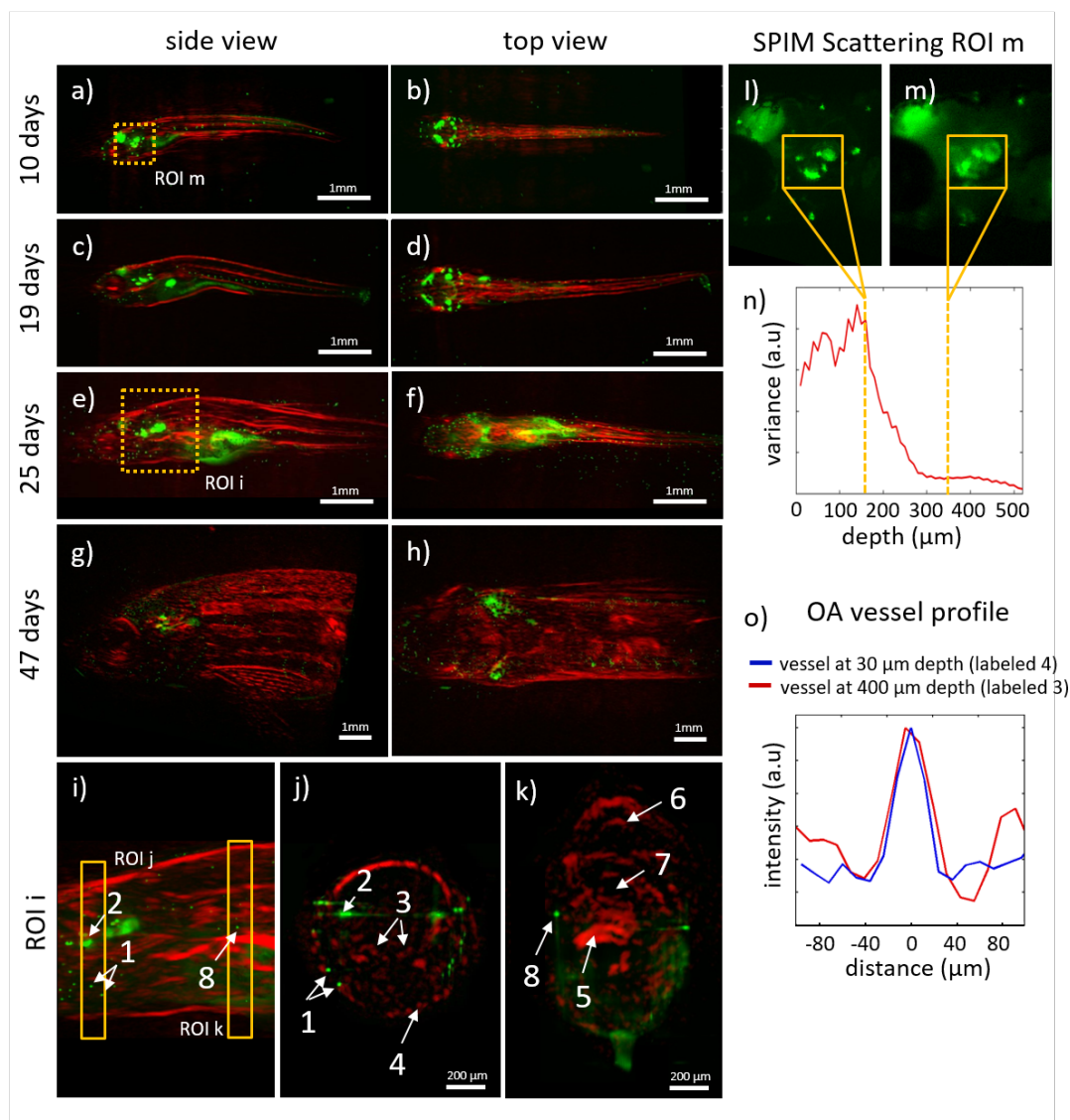
Figure 5.1: Hybrid SPIM-optoacoustic mesoscopy imaging of zebrafish development Brn3c:GFP zebrafish expressing GFP in hair cells were imaged at 10, 19, 25, and 47 days after fertilization. GFP fluorescence (green) was imaged by SPIM. The optoacoustic signal (red) was measured at the same wavelength of 488 nm . (a,c, e, g) Side views. (b, d, f, h) Top view of the reconstructed volumes. (i) Enlarged view of ROI i from panel e. (j) Cross-sectional view of the ROI j depicted in side view in panel i. (k) A cross-sectional view of the ROI k from further down the belly. Anatomical features are indicated: . 1,8: hair cells; 2: ear; 3,4: vessels; 5: intestine; 6: spine; 7: swim bladder. l) and m) show single slices from the SPIM datastack of the 10d larvae. While l) shows the ear which is close to the objective (160 µm depth), m) shows the ear faceing away from the objective (340 µm depth). The latter shows the effect of scattering, which is experienced after approximately 180 µm. This can also be quantified: In n) the variance of the fluorescent intensity as a measure for image sharpness is plotted. In contrast, p) shows the sharp intensity profile of vessels on the surface (labeled with 4 in panel j at 20-30 µm depth) and deep within the fish (labeled with 3 in panel j at approx. 400 µm depth) measured with optoacoustic mesoscopy.

structures, especially the otoliths (ears), which emit a strong signal in the larvae and juvenile developmental stage, are much weaker and more blurred in the adult zebrafish. The size and depth of this structure increases with age and the tissue around the ear becomes more scattering. Furthermore, the zebrafish develops an opaque and reflecting skin, which makes imaging even more challenging. The labeled neuromast cells, which are located at the surface of the fish, are visible throughout all developmental stages in the SPIM images. The loss in resolution of SPIM with depth is exemplarily shown in Figure 5.1l-n. In Figure 5.1n a plot of the variance of the GFP fluorescence image as a function of image depth can be seen. The (normalized) variance of an image can be used as an indicator for image sharpness and therefore as a measure for the amount of scattering in the sample [105]. The zebrafish is imaged from the side. Due to the symmetric anatomy of the zebrafish the same structures are present on both sides of the fish, with the structures from one side being close to the objective and the structures from the other being image at a significant larger depth. This can be seen in Figure 5.1l and m, where the two ears of the zebrafish are shown, one facing the objective and one facing away from the objective. The corresponding imaging depth of the two slides is indicated in the variance plot in Figure 5.1n. As seen in the plot, the variance and therefore the image sharpness rapidly decreases beyond approximately 180 μm due to scattering. The ear closer to the objective is sharper compared to the ear further away form the objective, which can be seen in the shown image slices as well as in the variance plot.

In contrast to the SPIM images, the red optoacoustic signal from melanin remains strong at all ages, and the overall morphology as well as internal structures are visible. For the shown sample size, the optoacoustic resolution of the system is not affected by the imaging depth. This is demonstrated on two vessels in Figure 5.1o, where a profile plot of the vessels is shown. One vessel (blue) is located close to the surface of the zebrafish and one vessel is located in the middle of the zebrafish at a depth of 400 μm(red). The location of both vessels within the fish is shown in panel j, where a slice from the belly of the fish is depicted (labeled with 3 and 4). The optoacoustic signal from the vessels remains strong over the whole size of the zebrafish and the edges of blood vessels show an unaffected sharp shape even at depths of 400 μm. The measured FWHM of the depicted blood vessels was 35 μm in both cases, which is at the resolution limit of the optoacoustic system.

These results highlight the complementary nature of the information obtained from SPIM and optoacoustic mesoscopy and show the capability to image samples over a large range of sizes, from the early larval stage until adulthood.

5.2 Conclusion and Outlook

In this thesis a novel hybrid SPIM and optoacoutic mesoscopy imaging system is presented that significantly improves the imaging depths compared to conventional fluorescence microscopy, allowing the study of model organism development from early stages through adulthood. The hybrid system can detect fluorescence contrast

agents through SPIM and complementary absorption contrast through optoacoustic mesoscopy, allowing to visualize anatomical structures deep within adult zebrafish. We have demonstrated that the decrease of image quality and resolution due to light scattering [2] for older samples in SPIM can be overcome through optoacoustic mesoscopy, which maintains its resolution for developing biological samples over long periods of time.

The presented imaging quality and imaging depth could only be achieved by extensive work on the underlying reconstruction algorithms. To improve the imaging depth of SPIM a new prior and an adaptive regularizer were introduced and tested. Both the simulated and the experimentally acquired results show that the novel regularizer and prior are able to correct for scattering within the sample and enhance the image quality and depth. In the presented dataset the imaging depth could be increased by $30\,\mu m$. Furthermore, the adaptive regularizer minimizes the effect of over-regularization on the reconstruction compared to static regularization approaches. The improved reconstruction due to the introduced prior and regularizer only uses image information from neighboring planes, together with a simple model for the scattering of light in the sample. This model was implemented through the Tikhonov regularization and has shown to the capability to account for an increased scattering which comes along with an increased imaging depth [21].

Two different scanning geometries for the optoacoustic acquisition were evaluated and the characteristics of the used transducer array were analyzed. With the knowledge about the detector characteristics, we were able to improve the optoacousitc reconstruction significantly. The sensitivity field of the transducer was incorporated in the form of a weighted backprojection algorithm. The results acquired with the weighted backprojection show that the algorithm heavily reduces reconstruction artifacts for larger samples. The deconvolution of the acquired signal and the electrical impulse response could improve the achieved reconstruction quality even further.

Our novel hybrid system allows multiscale imaging of fluorescence and optoacoustic signals to visualize components and processes at the cellular, tissue, and organismal levels. Our setup is compatible with other model organisms such as *Xenopus* and *Axolotls*, and it may be particularly useful for organisms that go from transparent to opaque during development and so cannot be analyzed in vivo using conventional optical microscopy.

Outlook

Optoacoustic imaging offers the great possibility of acquiring multispectral contrast from endogenous absorbers. This aspect of optoacoustic imaging was not covered in this thesis, but could easily extend the possible range of application for the system. The multispectral capability of the system allows for imaging the distribution of numerous target molecules or tissues to be imaged simultaneously, either in a label-free way or following expression or injection of exogenous contrast agents.

The range of agents compatible with optoacoustic imaging continues to grow [106], opening up exciting possibilities for in vivo imaging using our set-up.

The presented system can be improved in several ways. Improvements can be achieved on both levels, on the hardware and on the reconstruction level.
The SPIM reconstruction of the object and the PSF will get better the more information is available. The algorithm could be extended to handle additional datasets, either in the from of multiple views from the sample, or in the form of a varying illumination.
Furthermore, imaging information acquired with one of the modalities can be used to improve the reconstruction of the other imaging modality. Information about the shape, the scattering coefficient, or the distribution of a certain (fluorescent) label, could be used and incorporated into either of the reconstructions.
When the multispectral capability is exploited, spectral correction becomes important. Not only will the laser energy vary with the used wavelength, but also the absorption within the sample and therefore the light fluence will change with the wavelength and distort the acquired spectrum. For the near infra-red regime, computational methods have already proven to successfully correct for the change in light fluence and provide more accurate spectral information from the sample [107]. These methods could be extended to the visible range and applied on the hybrid imaging system.

The biggest improvements can be expected on the hardware level by further optimizing the used detectors and detection geometries. The system currently uses a linear cylindrically focused transducer array, which has relatively small ultrasound elements, limiting the detection sensitivity. Switching to more sensitive, spherically focused detectors, which have a much larger detection aperture, may increase the SNR, and improve the system's ability to detect low concentrations of contrast agents. With an increased sensitivity the system might be able to detect the same genetically expressed fluorescence labels which are visible in SPIM. This would enable a consistent tracking of the structures of interest from cellular level in the larvae stage to an age when the structures are not accessible anymore by light microscopy. All these future improvements and the data shown in this article reveal the promising potential of our system, which is able to monitor developmental processes deep within the samples over long timescales.

List of Figures

Published material and reprint permissions

Most of the results presented in this work has been previously published in different articles or are being prepared for publication in the near future.

- In chapter 3, Figure 3.9, Figure 3.10, and Figure 3.11 were adapted from [21] (© 2016 SPIE).

- In chapter 3, Figure 3.12 was adapted from [79] (© 2015 John Wiley & Sons, Inc).

- In chapter 5, Figure 5.1 was in preparation for submission during the thesis was written.

Permissions to reproduce text passages and illustrations are granted through the author rights in the copyright transfer agreements for the above mentioned publications and have been additionally obtained in written form through email contact to the editorial boards.

List of publications

J. Ripoll, B. Koberstein-Schwarz, and V. Ntziachristos, "Unleashing Optics and Optoacoustics for Developmental Biology," *Trends in Biotechnology*, vol. 33, no. 11, pp. 679–691, 2015.

H.-C. A. Lin, A. Chekkoury, M. Omar, T. Schmitt-Manderbach, B. Koberstein-Schwarz, T. Mappes, H. López-Schier, D. Razansky, and V. Ntziachristos, "Selective plane illumination optical and optoacoustic microscopy for postembryonic imaging," *Laser & Photonics Reviews*, vol. 9, no. 5, pp. L29–L34, 2015.

B. Koberstein-Schwarz, L. Omlor, T. Schmitt-Manderbach, T. Mappes, and V. Ntziachristos, "Scattering correction through a space-variant blind deconvolution algorithm," *Journal of Biomedical Optics*, vol. 21, no. 9, p. 096005, 2016.

Acknowledgments

I would like to thank everyone who supported my work during the past three years. My special thanks go to Prof. Vasilis Ntziachristos for giving me the opportunity of working on such a great project and for his advise and feedback.

Tobias Schmidt-Manderbach, Lars Omlor, and Murad Omar are to be thanked for the countless discussion on the project. Their advise can be considered an important contribution to the presented work. Furthermore, I would like to thank them for proof-reading my thesis.

Paul Vetschera, who worked together with me on the presented hybrid system, is to be thanked for the hours of collaborative work in the lab and the discussions in our office. Many of the shown measurements were acquired with his help.

Josephine Reber has to be thanked for finding and organizing suitable samples and for valuable advise on all the biological aspects of the project.

Amy Lin, Jiao Li, Christian Dietrich, Wibke Hellmich have to be thanked for help with technical and biological problems which occurred during the three years I worked on the project.

Finally, I would like to thank all of my colleagues form the IBMI with whom I shared a chat in the kitchen or during the lunch break - or at a one of the many occasions after work.